PHYSIK-DEPARTMENT

Single Molecule Sensors to Study Hydrophobic Phenomena

Dissertation

von

Michael Geisler

TECHNISCHE
UNIVERSITÄT
MÜNCHEN

TECHNISCHE UNIVERSITÄT MÜNCHEN

Physik Department
Lehrstuhl für Biophysik E22

Single Molecule Sensors to Study Hydrophobic Phenomena

Michael Geisler

Vollständiger Abdruck der von der Fakultät für Physik der Technischen Universität München zur Erlangung des akademischen Grades eines

Doktors der Naturwissenschaften (Dr. rer. nat.)

genehmigten Dissertation.

Vorsitzender: Univ.-Prof. Dr. Friedrich Simmel
Prüfer der Dissertation:
1. Univ.-Prof. Dr. Thorsten Hugel
2. Univ.-Prof. Dr. Roland Netz

Die Dissertation wurde am 02.11.2009 bei der Technischen Universität München eingereicht und durch die Fakultät für Physik am 14.12.2009 angenommen.

This work is dedicated to my wife

Jutta

and my children

Zoe and René

"…One is reminded of the story of the drunk who, one dark night, lost his keys. He is seen looking for them under a street light. When asked where he lost them, he points across the street, where all is dark. "Why, then, are you looking for them here?" He replies, "Because there is more light here". Until more searching is done in the darkness, our understanding of the hydrophobic effect must be considered quite incomplete."

Walter Kauzman, Nature, 325 (1987)

"I know a man who grabbed a cat by the tail and learned 40 per cent more about cats than the man who didn't."

Mark Twain,

cited by Carlos Bustamante, Nature, 1 (2000)

Table of Contents

Table of Figures

Summary

Although many factors influence the adhesive strength of attached interfaces, the cohesive strength of a material, or the stability of a protein's functional structure, these properties are all ultimately limited by the forces needed to break molecular bonds.

In the current study, with the aid of AFM-based dynamic force spectroscopy in combination with theoretical methods, we will develop a more and more refined understanding of hydrophobic phenomena comprising adhesion, aging, hydration and self-assembly. Therefore, we have designed a single molecule sensor which is capable of measuring equilibrium forces and free energies per length between individual polymers and different solid/liquid interfaces in a variety of solutions. The small size of the system allows a direct comparison with all-atomistic molecular dynamics simulations. Our approach similar to a "nano-peel test" demonstrates negligible friction and a high in-plane mobility of the adherent polymers. Surprisingly, most material properties like roughness, conductivity, surface potential and even composition hardly influence single molecule adhesion under equilibrium conditions. A comparison of molecular adsorption free energies, surface potential differences and the surface energies at different points in time reveal a clear relation between these quantities and the process of material aging. We will demonstrate that chemical modifications in particular those which alter the surface wettability are in fact capable of fine-tuning the surface adhesion of polymers. Wettability and other directly solvent-related properties, such as ion concentration have the greatest effect observed. We identify an ion-specific dependence (Hofmeister effect) of the desorption forces which is pronounced at high ionic strength. Here, the quasi infinite dilution of the polymer under investigation allows to access the whole soluble concentration range for ions.

The hydrophobic effect can be defined in terms of the thermodynamics associated with the transfer of a molecule into aqueous environment. In a thermodynamic analysis, we are able to reproduce characteristic temperature signatures including entropy and enthalpy convergence for amphiphilic proteins. In addition, an ion specific shift in these convergence temperatures is detected, when the polymers are pulled into electrolyte solution, which can be linked to the hydration behavior of the ions and the ion-specific (Hofmeister) series.

Based on these findings, we show that a single protein molecule can undergo a conformational transition induced by a surface depending on the substrate hydrophobicity and facilitated by increased temperature as well as by the presence of ions. Here, the structure of an amylodogenic spider silk protein and its stability is analyzed and compared to the properties of its assembled fibrous form.

Moreover, our molecular force sensors are also applied to translate cosolute binding equilibria into measurable forces and so to determine binding parameters such as the distances between neighbouring binding sites, binding free energies and association constants.

All these findings will help to attain a predictive understanding of the hydrophobic and

related effects and guide the development of functionalized nano-materials in contact with polymer solutions. Single molecule force sensors like those presented here might evolve to become a powerful tool in materials- and surface science, capable of meeting the growing requirements for analytic instrumentation in nanotechnology.

Introduction and Outline

Hydrophobic phenomena play a crucial role in self-assembly processes over multiple length scales, from the microscopic origins of inert gas solubility in water, to the mesoscopic organization of proteins and surfactant structures, to macroscopic phase separation [1]. Today these phenomena, such as the tendency for oil and water to segregate, are important in diverse applications: from the cleaning of laundry, to the creation of micro-emulsions in materials research, to the folding of proteins into functional complexes. The science of hydrophobicity quite possibly starts with the *similia similibus solvuntur* or like-likes-like principle of solubility and miscibility that is a traditional part of physical chemistry and, before that, alchemy [2,3]. Nowadays, studies of the hydrophobic effect are at the boundary line between physical chemistry and biophysics, with focus on water structure and thermodynamics.

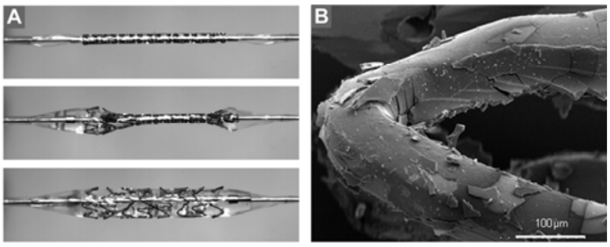

Figure 0.1.1: Expansion of a drug coated vascular stent graft. (A) The stent expansion with a balloon catheter takes only a few milliseconds. The high strains and forces that are acting on the device cause the applied coating to fail. The SEM image in (B) shows the brittle coating of 1% Rapamycin on the electropolished strut surface after expansion.

In particular, hydrophobically driven adhesion of macromolecules onto surfaces plays a vital role in biological processes and for the biocompatibility of engineered materials. For example, the adhesion between a cell and the surface of a cell growth support is determined by adherent integrins and other adhesion promoting molecules. In this case geometry, polarity and wettability of a surface determine the efficiency of cell attachment, growth and finally differentiation [4-7].

In implant technology, biomaterial-related infections pose serious problems and are the main cause of implant failure. Treatment of infected implants most commonly includes long-term application of antibiotics and frequently results in implant removal. Such infections start with the initial adhesion of blood plasma proteins and a subsequently growth of bacteria often accompanied by the formation of a biofilm [8-11]. A prominent approach to inhibiting implant infections is the local treatment by active agents coated onto the implant surface or incorporated into a polymer matrix [12,13]. The adhesion of these coatings has to be designed to keep up the functionality of the drug delivery system (figure 0.1.1). Therefore, understanding how to prevent or improve the adhesion of proteins and other biopolymers to surfaces under physiological conditions is fundamental for the engineering of biocompatible medical devices and anti-infective implants [14-17]. Given the specific needs of cardiovascular implants, tissue engineering templates and diagnostic microdevices, there is a new focus on the design of new materials. Biosurface engineering utilizes the adjustment of molecular level surface structure to obtain bioactive materials. Desired functions of biointerfaces are mainly based on principles of molecular recognition and adhesion. In order to understand protein adsorption patterns the surface properties of the substrate and their interplay with biopolymers, proteins, cosolutes and the solution conditions have to be considered [18]. Hydrophobic effects are present in all of these interactions and sometimes even prevailing.

In the first chapter, we will outline the evolution of the idea of hydrophobicity, provide basic definitions, and present the physics of polymer desorption in equilibrium as well as non-equilibrium. We will further discuss the equilibrium adsorption isotherm introduced by Gibbs and Langmuir and develop a one-dimensional binding model. Special emphasis will be put on all-atomistic molecular dynamics simulations as they will frequently complement our experimental studies. In preparation for the upcoming chapters, the different facets of single molecule force spectroscopy will be reviewed. The remainder of this manuscript is organized as follows: At the beginning of each chapter, highlighted by a colored textbox, a brief abstract will provide an overview of the main achievements. Following a short and more specific introduction to the particular topic, the experimental results will be present consecutively. After stating theoretical aspects in chapter 1, we will start with a thorough characterization of our single molecule sensors in chapter 2. Chapter 3 will deal with the different factors that play important roles in hydrophobically driven polymer adhesion at interfaces. In this context, special emphasis is put on the aging process of materials and its role in polymer interaction in chapter 4. In chapter 5 we will address entropy convergence as a fundamental concept in the description of hydrophobicity. Finally, the surface induced folding and unspecific cosolute binding to a single polymer will be investigated in chapter 6 and 7. The outlook addresses future prospects of single molecule sensor technology and the remaining challenges in this field of research.

Chapter 1

Armamentarium

1.1 The conceptions of hydrophobicity

The term hydrophobic (water-fearing) was initially introduced to describe the low solubility and the unusually strong attraction between small nonpolar molecules such as methane in water [19]. Hydrophobicity (also referred to as hydrophobic attraction, force, bond, hydration effect, etc.) is a familiar concept in the thermodynamics of non-polar molecules in aqueous media and is tightly related to the concept of entropy convergence in protein folding—the idea that the hydrophobic entropy change on folding nearly vanishes at a universal temperature [1,20].

As early as 1937, researchers recognized the complexity of the problem of the low affinity of nonpolar groups for water and postulated an entropic origin for the effect because of its strong temperature dependence [21]. In a landmark paper by Frank and Evans, a first attempt at providing a detailed theory of the hydrophobic effect was made [22]. Frank and Evans described water molecules rearranging into a microscopic ‘‘iceberg’’ around a nonpolar molecule and discussed the entropic consequences of this ‘‘freezing.’’ Several years later, Klotz developed a general theory of the bond between two nonpolar molecules [23], and in 1959, the term ‘‘hydrophobic bond’’ was introduced by Kauzmann to describe the tendency towards adhesion between the nonpolar groups of proteins in aqueous solution [24]. Kauzmann suggested that this bond was probably among the most important factors in the stabilization of certain folded configurations in native proteins. However, the use of the word ‘‘bond’’ was soon considered inappropriate, given that the attraction between nonpolar groups lacked any of the characteristic features that distinguish chemical bonds from van der Waals forces.

In the 1960s there existed the idea, based primarily on the work of Tanford, Kauzmann, Nemethy, and Scheraga, that there was a hydrophobic bond, viewed as the spontaneous tendency of nonpolar groups to adhere in water to minimize their contact with water molecules [24-28]. In 1954, Kirkwood noted that the role of water molecules in the average attraction between nonpolar groups might be larger than that of the direct van der Waals interaction between these groups [29]. Since then, one has to think of the hydrophobic forces between particles as being not only due to the properties of the particles themselves but rather because of the characteristics of the suspending solvent medium.

The concept of hydrophobicity is nowadays more broadly used to describe forces between all kinds of nonpolar objects in aqueous environments, implying a common mechanism for protein folding, micellization, self-assembly of lipids, oil–water demixing, and thus any supermolecular aggregation in water [30,31]. The rate of protein folding remains a very active research area and has become one of the primary motivations for developing an understanding of the hydrophobic interaction at molecular length scales, as has been the case since the pioneering work of Kauzmann [24] and Tanford [32].

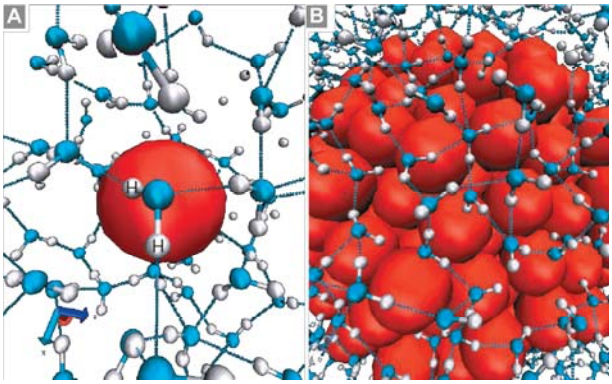

Figure 1.1.1: Length scale dependence of hydrophobicity [1,33,34]. (A) Water hydrogen bonding patterns simply go around a small hydrophobic solute (< 1nm, red). The blue and white particles represent the Oxygen (O) and hydrogen (H) atoms of the water molecules. The line indicate the H.bonds (O-H···O) of no more than 3.5 Å in length. There is an entropic cost to the free energy of solvation, because the presence of a small hydrophobic molecule limits the configuration space available for hydrogen bonding, but the overall amount of hydrogen bonds remains relatively unchanged. (B) In contrast, the solvation of extended hydrophobic surfaces has a disruptive effect on the water structure. Close proximity of water is energetically unfavorable, because it is impossible to maintain a hydrogen bond network adjacent to an extended surface. As a result, water density is depleted near the surface [35]. Illustration is taken from Chandler et al. [31].

For predicting protein structures and function the magnitude and nature of the hydrophobic attraction acting between peptide segments or a protein and a surface are central issues that have not been fully resolved yet. Complications arise when comparing experimental results that include the ‘‘degree of hydrophobicity’’ of the surfaces (as defined by contact angle measurements [36]), the effect of surface roughness, and the possible existence of a layer of gas or density-depleted water at the hydrophobic solid–liquid interface [35,37-40], which are assumed to affect the forces between surfaces [30,41]. One goal of this work is to experimentally isolate these different contributions and to develop a method to study them separately.

Much effort was put in force measurements between well defined model systems, for example mica surfaces made hydrophobic or micrometer-sized plastic beads. However, these systems are notoriously plagued by secondary effects, such as bubble adsorption and cavitation effects [42,43] or compositional rearrangements [44]. Unfortunately, even if bubbles and other complications can be excluded, the very short-ranged portion of the hydrophobic attraction between micrometer-sized surfaces could not be resolved experimentally so far because of mechanical instabilities of the measuring device [30]. Likewise, the complex scale dependence of the hydrophobic effect (figure 1.1.1) makes it nontrivial to relate the force between micrometer-sized particles to the one between molecules [1,33,34,45]. It transpires that for the understanding of hydrophobically driven protein collapse [46,47] and polymer adhesion [2] a model system on the molecular scale is needed [48-51].

1.2 The role of cosolvents for the hydrophobic effect

Many of the experimental techniques used to study biomolecules rely on cosolvents to crystallize, denature or stabilize proteins, thus an understanding of the cosolvent effect on hydrophobicity is of great practical importance to protein science. For aqueous solutions in biology, the situation discussed above is even more complex, because in nearly all cases the solvent is in fact an electrolyte solution, and the presence of ions gives rise to various effects. Besides the obvious screening of electrostatic forces, which only depends on the ionic strength, there are effects which strongly depend on the ion type. These effects are commonly called Hofmeister (or lyotropic) effects [52,53] and are ubiquitous: they have been observed for dozens of diverse measurements from surface tension to bacterial growth [53-56]. Often these interactions are specific to the protein and to the particular conditions employed (pH, temperature) [57-61] and become important at moderate to high salt concentrations (0.01 to 1 M) [52,62,63].

It is reasonably well-understood that salts can affect electrostatic interactions either through indirect screening of charge-charge interactions [64,65] or by direct binding and neutralization of charged groups [66]. Less well-understood is the mechanism by which salts affect the properties of uncharged or hydrophobic groups in aqueous solution. In Hofmeister's pioneering works of the late 19th century, he sorted the common salt ion pairs into series according to their effect on protein solubility and conformational stability [67]. This ranking for monoatomic ions correlates with surface charge density and polarizability, but for complex polyatomic ions, the underlying mechanisms for the Hofmeister series are less apparent [68]. For example, the guanidinium cation is an effective protein denaturant, while among anions, thiocyanate is a strong denaturant, chloride is essentially "neutral", and sulfate stabilizes proteins [69].

Quantification of the Hofmeister (solubility) effect of a salt is usually obtained via linear regression of the relative solubility of a chosen solute (e.g., polymers, proteins, or other organic molecules) versus the salt's concentration [70-73]. Although such measurements provide useful information on the salting-in and salting-out behavior of individual types of salt ions, they do not reveal the mechanism by which salts actually modulate solute behavior. Recent NMR studies have argued in favor of direct interactions between the salt and the non-polar group [74-76], whilst other views favor indirect interactions mediated by the hydration shells of the ions and the non-polar solutes [77]. One approach attempted by Ninham and Boström et al. describes the interactions between the ions and a protein surface by electrostatic and dispersion forces. On average, the ions thus "see" a more or less homogeneous surface. Here, specificity comes in mainly through the frequency dependent polarizability of the ions [78,79].

Implicit clues might be obtained from salt induced changes in other macroscopic solution properties such as surface tension, viscosity, partial molar volume and osmotic coefficient [52,80-83]. Changes in solution properties largely reflect changes to the behavior of the solvent, in this case water, and it seems reasonable therefore to assume that salts might influence the solubility of hydrophobic solutes by altering, in some way, the overall liquid water structure. It is well-known that ions differ widely in their effects on the local water structure [84-87]: Molecular Dynamics (MD) simulations, for example, have shown that small (charge-dense) ions exert strong orientational effects on water molecules within their first solvation shell (strongly hydrated), severely limiting the latter's abilities to form hydrogen bonds with other water molecules ("structure-maker", also named kosmotropes). Larger (charge diffuse) ions on the other hand, appear to behave more like hydrophobic solutes, with disturbances of the water hydrogen bonding network that is not followed by the formation of stronger ion–solvent interactions (weakly hydrated, "Structure-breaker" or chaotropes) [54,88,89] [i].

As a consequence, bulk water will repel chaotropic ions toward interfaces (e.g. air/water or oil/water), and tend to keep kosmotropic species in the bulk [90]. Experimental data and MD calculations predict that, in solution, fluoride and chloride ions remain in the bulk phase, while iodide and bromide ions approach the air/water interface [91-93]. An apparent confirmation of this process seems to be for example the asymmetric distribution of halide ions in seawater aerosols [91]. It has been shown quite recently that large ions (such as bromide or iodide) are attracted also to solid hydrophobic surfaces, smaller anions like chloride are only weakly adsorbed, and cations are repelled [93,94]; in dramatic contradiction to the classical view according to which ions are repelled from non-polar surfaces due to image-charge effects [95-97]. This implies that the hydrophobic effect in the presence of ions involves ion adsorption and thus induced electrostatic interactions, even if the hydrophobic surfaces themselves are normally electrically neutral.

For a complete analysis, the ions themselves have to be considered as solutes, which competitively adsorb at the surface and also at the macromolecule [18,79,98]. Remarkably, there is a strong similarity to the influence ions have on the surface tension of water [81,99-101]. The key to the understanding of Hofmeister effects is therefore thought to be related to the ion-induced change of the thermodynamics of the interfacial water layers. Indeed, good progress was made for the air-water interface, and the experimentally observed trends for the surface tension and the surface potential are well understood by now [94,95]. At solid surfaces, on the other hand, the Hofmeister series is unexplained so far, even for model surfaces. The reason is the complexity of the interfacial system, where forces of various origins are acting. Simulations and experiments consistently show that hydrophobic interactions are modified by the addition of salt in an ion-specific manner. The trends on hydrophobic solid surfaces are similar as for the air-water interface. The van der Waals or dispersion interaction is repulsive for all ions and therefore not responsible for the observed adsorption of ions on surfaces [96]. It follows that ion adsorption on surfaces is more complicated

---

[i] The term structure maker and breaker is better understood in terms of the effect of the solutes on the protein stability. Kosmotropes stabilize (don't denaturize) the proteins secondary structure, thus tend to precipitate the protein. Chaotropes on the other hand tend to solubilize the protein and might even denaturize the protein at higher concentration.

and depends on both, the ion interactions with polar and charged surface groups [98] as well as the modified properties of water in concentrated salt solutions. New insights can be expected from a fundamental thermodynamic analysis of the ion-specific phenomena at these interfaces, like the one described in chapter 5.

In a wider sense, with regard to the specific properties of the Hofmeister salts, this series can be extended from inorganic to organic cosolutes [63,66]. The selection of particular organic molecules as preferred osmotic regulators in biological systems appears to have evolved as a strategy to design a microenvironment for macromolecules compatible with, and even optimal for, enzymatic catalysis, biological recognition and conformational stability [102]. Somero and co-workers observed that a rather limited repertoire of small molecular weight organic compounds constitute the preferred response to osmotic perturbations in the most diverse organisms [103,104]. A number of methylamine solutes, such as trimethylamine N-oxide, sarcosine and betaine, polyols, sugars and amino acids such as glycine and glutamic acid, should therefore be added to the inorganic Hofmeister salts exhibiting stabilizing properties, others such as urea to those having a denaturizing effect on proteins[63]. We therefore address the stabilizing effect of osmolytes namely D-glucose on hydrophobic interactions explicitly in chapter 7.

1.3 AFM based force spectroscopy

Single molecule force spectroscopy is a technique based on the principle of the atomic force microscope (AFM) of Binnig, Quate and Gerber [105], the invention of which has opened new perspectives for the investigation of surfaces at high lateral and vertical resolution. Because of the possibility to use the AFM in aqueous environments it has become possible to image biological surfaces such as cells and protein layers at nm-resolution under physiological conditions. For a recent review of biological applications see refs. [106,107].

The detection of ultralow forces is an additional feature of the AFM. The principle is illustrated in figure 1.3.2. A soft cantilever of silicon nitride with a sharp tip of about 10 nm tip radius at its free end is moved along all three axes and positioned with nanometer accuracy relative to a sample surface with a piezoelectric actuator. It can be further used to contact a molecule on the substrate surface and to exert a force on it. This applied force is detected through the bending of the cantilever by means of an optical lever and a position sensitive photodiode which allows sensing molecular forces down to the piconewton range [108]. The theoretical limitation in sensitivity of this kind of experiment is imposed mainly by thermal fluctuations of the cantilever (see Appendix A) and is well below typical molecular forces [108]. The recorded force-separation traces make intramolecular stabilizing forces, structural energy barriers, mechanical properties, and even the ligand binding to proteins readily accessible [109].

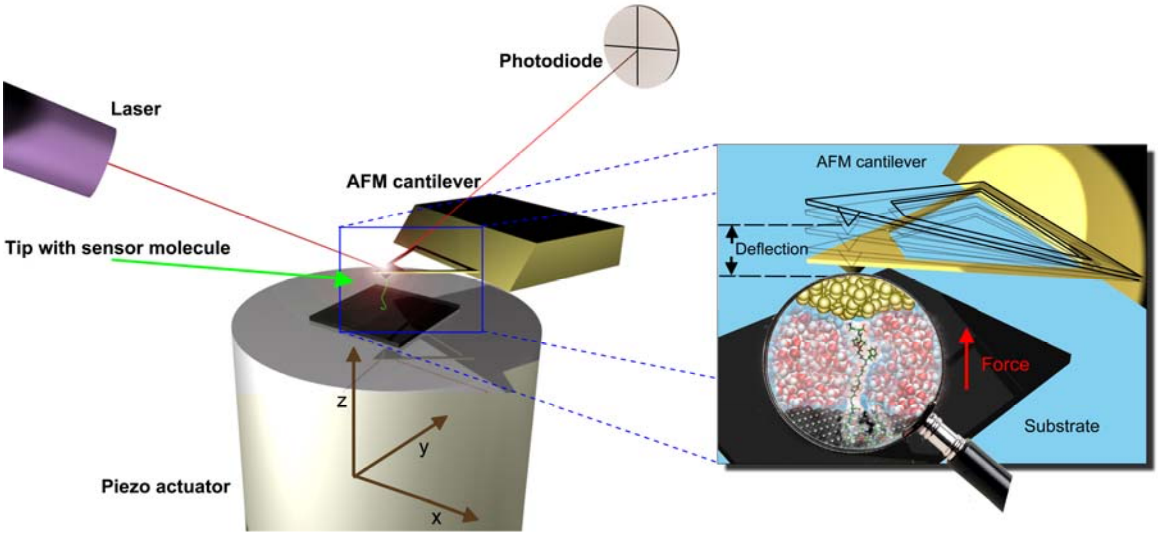

Figure 1.3.2: Principle of single molecule force spectroscopy (SMFS).

In force spectroscopy experiments so far the polymer under investigation has been tethered between cantilever tip and surface by unspecific attachment to the tip and substrate surface [110]. This kind of bonding is strong enough to provide stability for at least several seconds and has been utilized to study the reversible unfolding of titin domains [111], conformational transitions in polysaccharides [112], and specific antigen/antibody interaction forces [113]. Because physisorption, although thermally stable is in many cases insufficient the molecule was specifically bound to the substrate surface via chemical bonds in order to improve the long-term stability [114]. The attachment to the AFM tip that "picks up" the molecule is still unspecific in this case. This method still suffers from collective effects arising from confinements and interactions between substrate-grafted chains [115-117]. Typically, less than 1% of the experimental recordings reflect true single molecule events due to abundant surface and multiple-molecule interactions [118].

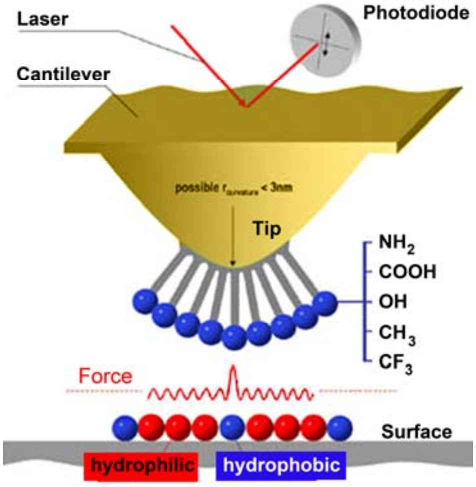

Figure 1.3.1: Schematic of chemical force microscopy with functionalized cantilever tips.

There is a wealth of data obtained with atomic force microscopy (AFM), where the cantilever tip is coated with polymers to measure the interaction strength of ligand-receptor bonds [119,120] or the adhesion forces from solid substrates [121-124]. In contrast to earlier measurements on pre-adsorbed polymer films, the substrate is no longer shielded by additional surface adsorbed polymer chains, and the interaction with the bare substrate can now be probed. Such experiments yield interaction forces, but not free energies related to the thermodynamic adsorption equilibrium. Moreover, the number of interacting polymers is generally not known in such experiments. A prominent application of this kind of tip modification with a uniform layer of chemical functional groups is chemical force microscopy (figure 1.3.1) [125,126].

Most recently, even though more complicated to achieve AFM based single molecule force spectroscopy (SMFS) has proven advantages over former approaches [127]. With the stable covalent attachment of the polymers to the AFM-tips, it became possible to investigate the adsorption process of the same set of molecules on a variety of surfaces and therefore deviations due to different sample preparations could be ruled out [128]. Furthermore, one can successfully avoid interference with other molecules and oligomeric structures. In this way sophisticated single molecule studies became possible, one of them being the realization of molecular scale machines such as the optomechanical switching of poly(azobenzene) which compares to a photonic muscle or motor, converting optical energy into mechanical work upon contraction [129].

In addition to intramolcular interactions (see also section 1.6) SMFS can be used to investigate the equilibrium adhesion of polymers onto solid substrates and to extract surface binding energies [130-134]. The equilibrium forces are characterized by well defined plateaus in the force extension trace [117,135]. Meanwhile the electrostatic contribution to the plateau force could be separated.[136] For polyelectrolytes on charged surfaces with charge density σ, the electrostatic part of the interaction is sensitive to the salt concentration, and the line charge density of the polymer τ can be determined [137]:

$$F_{Des}^{el} = F_0 + 4\pi l_B k_B T \sigma \kappa^{-1} \tau \qquad (1.1)$$

Here, l_B is the Bjerrum length and κ^{-1} the Debye length. On uncharged, non-polar surfaces, the adsorption force is commonly labeled as hydrophobic force. But as it turned out, the non-electrostatic part of the desorption force is dominant even in the case of charged polymers on charged surfaces [132,137]. Such intermolecular and intramolecular hydrophobic interactions that drive e.g. polymer collapse, adhesion, as well as salt specific effects at interfaces are far from being understood at the molecular scale [110,132,138,139].

1.4 Thermodynamics of polymer desorption – Equilibrium theory

In the following we summarize the equilibrium theory developed by Staple and Kreuzer to describe plateau forces like those measured with AFM. For a detailed description we refer to [M8]. In the measurement of plateau forces the experimentally accessible quantities are the constant plateau force F_{Des} and the maximum end-to-end length or maximum detachment length L_{max} to which the polymer can be stretched given its contour length L_c. Under equilibrium conditions the occurrence of plateau forces is a consequence of the fact that the portion of the polymer remaining adsorbed on the surface acts as a monomer reservoir at constant chemical potential μ for the stretched portion. Thus the slope of the force is given thermodynamically by

$$\left.\frac{\partial F}{\partial L}\right|_{T,\mu} = 0 \qquad (1.2)$$

as can be shown using the chain rule for implicit functions and the Gibbs-Duhem equation [140]. Because the adsorbed portion of the polymer is not truly infinite we need to equate its chemical potential with that of the stretched portion leading to the energy balance in terms of the Gibbs free energy.

The energy balance between the entire polymer adsorbed on the surface and the polymer in solution, completely detached from the surface is

$$G_{ads} + W = G_{sol} \qquad .(1.3)$$

When completely adsorbed on the surface and when completely detached from it, the polymer does not experience any force. Thus G_{ads} and G_{sol} are the Gibbs free energies under zero force. The work done to stretch the molecule to the maximum length before detachment is

$$W = W(L_{\max}) \approx F \cdot L_{\max} \qquad .(1.4)$$

To estimate the Gibbs free energies it is assumed that, adsorbed to the surface, the polymer is completely confined to a two-dimensional plane, whereas it has three degrees of freedom after detachment. To get some analytical results the freely jointed chain (FJC) can be used with contour length L_c and $N = L_c/L_K$ monomers of Kuhn length L_K. Note that the persistence length and thus the Kuhn length of a polymer are different for a molecule adsorbed on a surface from that in solution. Its Gibbs partition function reads (with dimension n = 2 or 3)

$$Z_G(F,T,N,n) = z(F,T,n)^N \qquad (1.5)$$

with

$$z(F,T,2) = \int \exp(\beta F L_K^{(2)} \cos\phi) d\phi \qquad ,(1.6)$$

$$z(F,T,3) = \int \sin\theta \exp(\beta F L_K^{(3)} \cos\theta) d\theta \qquad .(1.7)$$

Thus the Gibbs free energies and entropies at zero force are:

$$\begin{aligned} G_{ads} &\approx G_{FJC}(F=0,T,n=2) - N^{(2)} V_0 / N \\ &= -N^{(2)} k_B T \ln 2\pi - N^{(2)} V_0 / N \end{aligned} \qquad ,$$

$$\begin{aligned} G_{sol} &\approx G_{FJC}(F=0,T,n=3) \\ &= -N^{(3)} k_B T \ln 4\pi \end{aligned} \qquad ,(1.8)$$

where $N^{(3)} = L_c/L_K{}^{(3)}$ and $N^{(2)} = L_c/L_K{}^{(2)}$, respectively. From the energy balance (eq. 1.3) and the identity (1.4) one gets for the adsorption energy per unit length:

$$\begin{aligned} V_0 / N &\approx F L_{\max/} / L_c + \left(L_K^{(3)}\right)^{-1} k_B T \ln 4\pi \\ &- \left(L_K^{(2)}\right)^{-1} k_B T \ln 2\pi \end{aligned} \qquad .(1.9)$$

Next we develop a thermodynamic argument for the maximal length L_{max} to which the polymer can be stretched above the surface before its final bond with the surface is broken. Again it is considered that the experiment is done with such slow pulling speeds that the system remains in equilibrium. The fact that the pulling force $F = F_{Des}$ is constant implies that the Helmholtz free energy is linear in the length L

$$F(T,L) = F^{(2)}(T,L_c) + F_{Des} L \qquad ,(1.10)$$

where $F^{(2)}$ is the free energy of the adsorbed molecule. The maximum length attainable in equilibrium is given by the condition that the free energy (1.10) crosses that of the free molecule.

Adsorption energies are typically in the range of dispersion forces and hydrogen bonds, i.e. much less than covalent bonds or electrostatic forces. The values are somewhat larger when charges are present on the polyelectrolyte or on the surface. On the other hand, the change of entropy by reducing the length of a polymer by one unit is maximally $-k_B \ln 3$ for a 3-state model, i.e. $V_0 \approx F_{Des} L_c$ is a good estimate for the depth of the surface potential responsible for the adsorption of the polymer. We will make use of this relation to determine the adsorption energies of polymers on different substrates and under varying solvent conditions.

Weak adsorption or physisorption is not site specific because it is due to nonspecific dispersive forces or longer ranged hydrogen bonds. This implies that the surface corrugation, i.e. the lateral variation of the surface potential, is minimal, and thus the activation barrier to glide along the surface is small compared to the depth of the surface potential. This in turn, suggests that friction for the motion of the polymer along the surface is minimal, and maintenance of equilibrium at low AFM pulling speeds seems guaranteed throughout the experiment. The influence of surface corrugation on the desorption behavior has been simulated[141,142] (see also section 2.5) and we will examine the influence of the surface roughness in section 3.1.

As the anchor point of the polymer reaches a maximum length the polymer detaches itself from the surface and the force drops to zero: a region in the mechanical equation of state has been reached where metastability is observed. As in all measurements of metastability the experimental technique used determines the outcome to a large extent. Here we analyze stretching with an AFM in which the cantilever base is moved away from the surface with a time dependence z(t), e.g. at constant velocity. The force on the molecule is then given by

$$F(t) = k_c\left(z(t) - L(t)\right) \qquad ,(1.11)$$

where k_c is the cantilever stiffness and L(t) is the end-to-end length of that portion of the polymer detached from the surface. The change in force over a time interval Δt during detachment is then

$$\Delta F = k_c\left(\Delta z - \Delta L\right) \qquad .(1.12)$$

Here $\Delta z = z(t + \Delta t) - z(t)$ is the change in the cantilever position over the time interval Δt; if detachment occurs quickly on the timescale of the changes in z (i.e., for small velocities) one can take $z(t + \Delta t) \approx z(t)$ and one obtains:

$$\frac{\Delta F}{\Delta L} \approx -k_c \qquad .(1.13)$$

Thus, only in a measurement with an infinitely stiff cantilever the plateau force is expected to drop to zero abruptly (a discontinuity in the force-extension relation). For softer cantilevers, for which fluctuations become substantial, plateau forces decrease linearly to zero with a slope given by the cantilever stiffness. A polymer, detached from the surface, cannot counteract with a reaction force. This point is reproduced both in model calculations and experimental results, and is discussed in further detail in the following sections. Also note, that eq. (1.13) is valid both for equilibrium and for non-equilibrium experiments.

A polymer molecule attached to a surface experiences an attractive potential arising from bonds with the surface along its backbone. This situation has been modeled as the confinement of the molecule in an external potential [133,143]. Staple et al. developed an approach that yields an analytical result for the equilibrium statistical mechanics by working in the Helmholtz ensemble, where one end of the molecule is fixed at a distance h above the surface. Thus part of the molecule is stretched to an extent dictated by the surface bond strength: the stronger the bond the more the molecule outside the surface is stretched.

Under such conditions a fraction, N', of the N monomers of the molecule will be detached from the wall and the remaining N-N' will remain in the confining potential, gaining an extra energy V_0. Relating the number of monomers N to a contour length $L_c = N \cdot b$, the partition function is

$$Z(L_c, L) = \frac{1}{\lambda_{th}} \int_0^{L_c} Z_m(L_c^{(L)}, L) Z_S(L_c^{(S)}) dL_c^{(L)} \quad , \tag{1.14}$$

where λ_{th} is the thermal wavelength, $L_c^{(L)}$ is the component of that contour length which is desorbed from the surface, and $L_c^{(S)} = L_c - L_c^{(L)}$ is the component remaining on the surface; for brevity we omit the explicit dependence on the temperature T from our notation. Here $Z_m(L_c^{(L)}, L)$ is the partition function of the portion of the chain outside the confining potential, extended to an end-to-end length h above the surface. Similarly

$$\begin{aligned} Z_S(L_c^{(S)}) &= \frac{1}{\lambda_{th}} \int_0^{L_c^{(S)}} Z_S(L_c^{(S)}, l) dl \\ &= \frac{1}{\lambda_{th}} \int_0^{L_c^{(S)}} Z_m(L_c^{(S)}, l) \exp\left(\beta V_0 \frac{L_c^{(S)}}{L_c} \right) dl \end{aligned} \tag{1.15}$$

is the partition function of the portion of the chain in contact with the solid surface, accounting for the fact that it is free to attain any orientation and end-to-end length, gaining an energy V_0/L_c per unit length of the chain in the confining potential.

Thus far the Helmholtz ensemble for an isolated molecule is considered, with one end of the molecule constrained to a Length L above the surface. This choice of ensembles corresponds to the limit of stiff cantilever with respect to the molecule being stretched [144]. In actual AFM experiments the molecule is coupled to a cantilever with finite stiffness k_c; to account for this, a further convolution is needed with the partition function of the cantilever:

$$Z(L_c, z) = \frac{1}{\lambda_{th}} \int_0^{L_c} Z(L_c, L) Z_c(z - L) dL \, , \tag{1.16}$$

where L is the distance of the cantilever from the substrate and

$$Z_c(z - L) = \exp\left(-\frac{\beta k_c}{2} (z - L)^2 \right) \tag{1.17}$$

is the partition function of the cantilever.

The partition functions (1.14) and (1.16) assume that the polymer is in at least partial contact with both the AFM cantilever and the surface; this is the so-called “bridged” or partially adsorbed state. It is of course also possible for the polymer to be completely removed from the surface. The complete partition function accounting for these two states is:

$$Z_{tot}(L_c;z) = Z(L_c;z) + Z_F \,. \qquad (1.18)$$

Here the partition function for the completely desorbed chain is given by:

$$Z_F = Z_{tot}(L_c;0)\exp(-\beta F_0)\,, \qquad (1.19)$$

where F_0 is the Helmholtz free energy required to remove the polymer from the surface. Because the free energy change is due almost entirely to the confining potential (see last paragraph) it is possible to simplify the notation by setting $F_0 = V_0$.

Given the partition function Z_{tot}, all desired quantities including force-extension curves and fluctuations have been computed in past studies [145]. An important exception is that AFM measurements do not yield ensemble averages of partially adsorbed or completely desorbed (free) polymers. Rather, they measure the sudden desorption of a complete chain from the surface, visible as a sharp drop in the force. Thus, in practice it is useful to directly compare the partition functions for the partially adsorbed and the free molecules for the purposes of determining the force and length. For $Z(L_c;z) > Z_F$ the polymer is most likely to be found still in contact with the surface, and we assign to its partition function the value $Z(L_c;z)$. In this case the force can be computed as $F = -k_BT\partial \ln Z/\partial z|_{T,L_c}$ and the detachment length is $L = z - F/k_c$. For $Z(L_c;z) < Z_F$, the polymer is most likely detached from the surface and the force drops to zero.

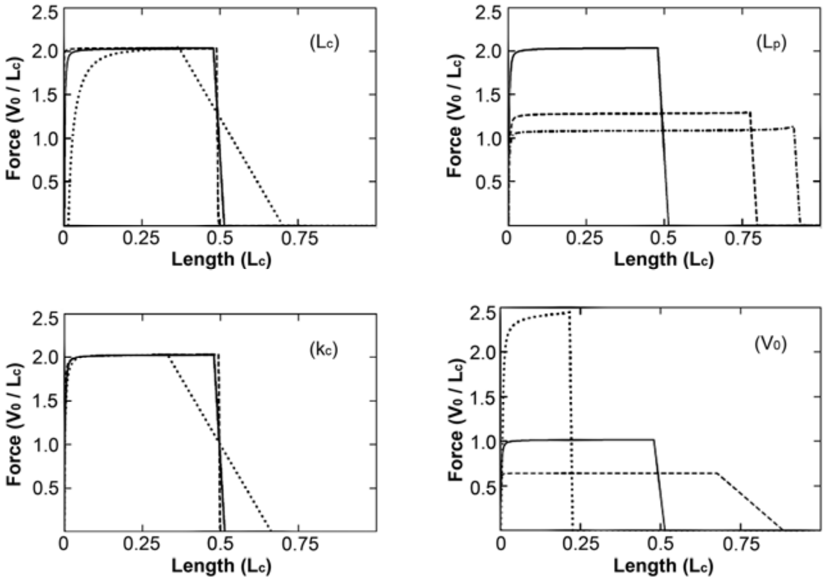

Figure 1.4.1: Equilibrium force-separation curves for polymer adsorption with varying parameter values. Figure is taken from [M8]. The solid curve is common to each panel and has parameters L_c = 100 nm, L_p = 0.4 nm, k_c = 10 pN/nm, and V_0/L_c = 100 meV/nm. Note that forces are plotted in the natural units of the adsorption strength, V_0/L_c, and lengths are plotted in units of L_c. Panels (L_c), (L_p), (k_c), and (V_0) show the variations of the master force-separation curve with each of those parameters, respectively, and all other parameters fixed as in the solid curve above. The temperature is fixed with T = 300 K for all curves. Parameters for individual panels are as follows: (L_c): dotted, solid, dashed curves have L_c = 10, 100, 1000 nm. (L_p): solid, dashed, dash-dot curves have L_p = 0.4, 4, 40 nm. (k_c): dotted, solid, dashed curves have k_c = 1, 10, 100 pN/nm. (V_0): dotted, solid, dashed curves have V_0/L_c = 10, 100, 1000 meV/nm, respectively.

Staple et al. have chosen adsorption energies V_0, cantilever spring constants k_c, persistence lengths L_p, and contour lengths L_c in the range of experiment. The maximum length attainable before the molecule loses contact with the surface varies from a small fraction of to the complete contour length, depending on the chosen parameters, see figure 1.4.1. Most important here are the persistence length and the adsorption energy: Stiff polymers require only little force to extend significantly, so polymers with a large persistence length tend to have large detachment lengths. Conversely, molecules that are only weakly bound to the surface (low adsorption energy) tend to detach sooner. For all curves, the slope in the detachment region is $-k_c$, as predicted by theory; the determination of the detachment slope is the primary effect of the cantilever spring-constant on the force-extension curve. Increasing the persistence length steepens the force-extension curve of the free molecule; this results in a decreased plateau force for adsorbed molecules, because at a given extension the restoring force of the molecule is much less. Equivalently, the maximum length increases such that the work required to remove the polymer from the surface (the area under the force-extension curve) is still the adsorption free energy.

We can summarize the main predictions of the equilibrium model derived by Staple et al which we will compare to our experimental results in chapter 2 as follows [140]:

(i) Plateau forces result from the fact that the portion of the polymer still adsorbed to the surface acts as a monomer reservoir at constant chemical potential.

(ii) In equilibrium, the maximum height attainable above the surface is controlled by the crossing of the free energies of the adsorbed and the free molecule.

(iii) The maximum height (in equilibrium) is always less than the contour length.

(iv) The maximum height and plateau force determine the strength of adsorption, i.e. the depth of the surface potential, given as an energy per unit length of polymer $V_0/L_c \approx F \cdot L_{max} / L_c$. For spider silk protein $F \approx 85$ pN and $L_{max}/L_c \approx 0.5$ at the lowest pulling peed where equilibrium is maintained. Thus we have $V_0/L_c \approx 0.27$ eV/nm.

(v) The slope with which the force decays to zero after the polymer has ruptured its last surface bond is always given by the inverse of the cantilever force constant whether pulling was done slowly in equilibrium or fast out of equilibrium. This fact can serve as an excellent check on the quality of the experimental results.

(vi) Plateau force fluctuations are controlled by the cantilever stiffness $(\delta F)^2 \approx k_c k_B T$. For typical experiments with $k_c = 10$ pN/nm we get $\delta F \approx 6$ pN, in agreement with the experimental force distributions (cf. section 2.7).

1.5 Non-equilibrium theory

The following nonequilibrium aspects of polymer desorption are based on theoretical considerations of Staple et al. (see also [M9]). If a molecule is quickly removed from a surface then non-equilibrium effects arise, which cannot be understood in terms of thermodynamic arguments alone. In analyzing previously published experimental data on plateau forces, Staple et al. came to the conclusion that, contrary to claims in the literature, most of these experiments were performed under non-equilibrium conditions. To account for non-equilibrium effects they extended the equilibrium model within a master equation approach [146,147].

Four different non-equilibrium effects can manifest themselves in pulling a molecule off a surface: (i) to change the desorbed contour length $L_c^{(L)}$, a bond with the surface has to be broken, (ii) to completely remove the molecule from the surface several bonds have to be broken simultaneously, (iii) for a new value of $L_c^{(L)}$ the end-to-end length L of the portion of the molecule not in touch with the surface has to adjust, and similarly (iv) the end-to-end length l of the portion of the molecule remaining on the surface with contour length $L_c^{(S)} = L_c - L_c^{(L)}$ must adjust. Processes (i) and (ii) are bond breaking, (iii) is internal relaxation with hydrodynamic damping the dominant effect in solution, and (iv) is dominated by friction with the surface. All four phenomena can be adequately described by Markov processes.

Simultaneous Desorption: Here, we describe the complete detachment of the polymer chain from the substrate as a two-state process. We define P_{ads}, the probability that the polymer is in at least partial contact with the surface, and $P_{sol} = 1 - P_{ads}$, the probability that the polymer has been completely removed from the surface. In equilibrium these probabilities depend only on the cantilever position z:

$$P_{ads}^{(eq)}(z) = \frac{Z(L_c;z)}{Z(L_c;z) + Z_F}. \qquad (1.20)$$

Out of equilibrium the probabilities $P_{ads}(t)$ and $P_{sol}(t) = 1 - P_{ads}(t)$ obey a master equation:

$$\frac{dP_{ads}}{dt} = W_{ads/sol}(z)P_{sol} - W_{sol/ads}(z)P_{ads}, \qquad (1.21)$$

where $W_{ads/sol}$ (z) and $W_{sol/ads}$ (z) are transition rates from the free to partially adsorbed states and vice versa. This equation follows, given the assumption that adsorption and desorption of individual monomers is fast on the timescale of desorption of the whole chain. For fixed cantilever position z the master equation (1.21) is solvable analytically:

$$\begin{aligned} dP_{ads}(t) = {} & \frac{W_{ads/sol}}{W_{ads/sol} + W_{sol/ads}} \\ & + \left(P_{ads}(0) + \frac{W_{ads/sol}}{W_{ads/sol} + W_{sol/ads}} \right), \qquad (1.22) \\ & \cdot \exp\left(-(W_{ads/sol} + W_{sol/ads})t \right) \end{aligned}$$

The time evolution $P_{ads}(t)$ for arbitrary cantilever motion z(t) can be obtained numerically by repeatedly applying Eqn. (1.22) over short intervals (short compared to the rate of change of the cantilever position z(t)). To complete the model explicit forms for the rates $W_{ads/sol}$ and $W_{sol/ads}$ are required. Such rates must satisfy detailed balance:

$$W_{ads/sol}(z)Z_F = W_{sol/ads}(z)Z(L_c;z), \qquad (1.23)$$

and can thus be written in the form:

$$W_{ads/sol}(z) = \omega_0 \left(\frac{Z(L_c;z)}{Z_F} \right)^{1-c},$$

$$W_{sol/ads}(z) = \omega_0 \left(\frac{Z(L_c;z)}{Z_F} \right)^{-c}, \qquad (1.24)$$

for $0 \le c \le 1$.

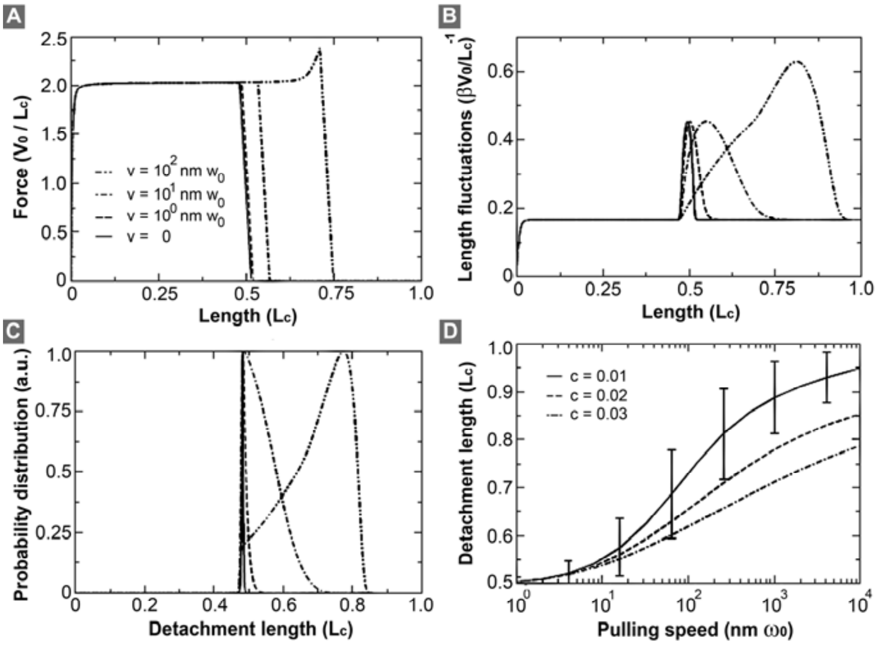

Figure 1.5.1: Non-equilibrium force-separation curves calculated in a two-state model of simultaneous desorption. The Figure is taken from [M9]. (A): Force-separation curves, showing an enhancement of the detachment length with pulling speed. (B): Length fluctuations, revealing a broadening and eventual enhancement of the fluctuations with pulling speed, centered around the detachment length. (C): Probability distribution of detachment length. All probability densities have been normalized to have equal maxima for plotting purposes. Common parameters for panels (A)-(C): $v = 10^0, 10^1, 10^2$ nm ω_0, for dashed, dash-dot, dash-dot-dot curves, respectively. All curves have detailed balance exponents c = 0.01. Solid curves were calculated in equilibrium. (D): Dependence of detachment length on pulling speed. Error bars are computed as the standard deviation of the distribution as in panel (C); for clarity of the plot these are presented only for one curve (c = 0.01), but values are representative of all three curves. Parameters: solid, dashed, dash-dot curves have detailed balance exponents c = 0.01, 0.02, and 0.03, respectively.

It is possible, in general, for such a system to have asymmetric adsorption/desorption rates. This asymmetry is captured by an exponent c in the transition rates; this exponent can be interpreted as the relative degree to which the applied force affects adsorption or desorption rates; $c = 0.5$ represents the case of symmetric rates, where $c < 0.5$ and $c > 0.5$ correspond to the cases where the applied force primarily affects the adsorption or desorption rates, respectively.

For the proportionality the simplest possible choice, was taken, namely that the rates are linear in an attempt frequency υ, and depend exponentially on a barrier height Q. These two effects can be combined into a single effective transition frequency $\omega_0 = \upsilon \exp(-\beta Q)$. In case of the widely used Bell model for example c is set to zero and in addition the reverse transition rates $W_{sol/ads}$ are neglected. In order to reproduce experimental data one then introduces an explicit dependence of the barrier height on the applied force. Although successful in intermediate regimes, such models typically violate detailed balance of desorption and re-adsorption by neglecting $W_{sol/ads}$ and thus only account for non-equilibrium processes but can not reproduce the equilibrium limit.

This model predicts an enhancement of the detachment length with velocity (figure 1.5.1). For values of c close to zero we find that this enhancement is significant and can cause the detachment length to asymptotically approach the contour length of the polymer (figure 1.5.1 (A)). In addition, the beginning of an enhanced force is visible in the highest velocity (dash-dot-dot curve) of figure 1.5.1 (A). In figure 1.5.1 (B) and (C) we present the non-equilibrium effects on length fluctuations and detachment length probability distributions. For intermediate velocities this dependence appears logarithmic (figure 1.5.1 (D)). On the other hand, in the limit of low pulling speed the detachment length of the polymer must converge to its equilibrium value. Similarly, in the limit of high pulling speed the detachment length approaches the contour length of the polymer. Thus, the dependence of detachment length on pulling speed necessarily varies sigmoidially from its equilibrium value at zero pulling speed to the contour length of the polymer at infinite pulling speed.

To simplify the physics behind the shape of the sigmoid we note that as you pull fast the force impulse has to travel down the backbone of the polymer for it to react mechanically, i.e. to break the bonds with the surface as the force signal reaches the end. The characteristic velocity of this impulse is $v_s = \omega_0 L_c$. Looking at the solution for the detachment length for small and large pulling speeds it suggests that a reasonable fitting function is given by

$$L_{\max} = L_c + \frac{2(h_{eq} - L_c)}{\exp(v/v_s) + 1} \qquad (1.25)$$

with $h_{eq} = L_c/2$.

1.6 Forced unfolding of proteins

In a typical unfolding experiment, which is always a non-equilibrium process, mechanical tension is applied to an individual molecule, and its forced unfolding is recorded in force-separation-traces. Due to the energy barriers of the folding potentials often being close to the thermal energy, both the extensions and the forces at which these barriers are overcome are subject to marked fluctuations caused by external experimental parameters such as the loading rate, the temperature [148], properties of the solution and other changes that result in a different bond strength [149,150]. As shown previously, contour length, which is independent of fluctuations and alterable experimental parameters, is a more appropriate variable than separation for the characterization of molecular energy landscapes and directly reflects the folding state of the molecule [151]. By transforming force-separation-traces into contour length space, histograms are obtained that directly represent the energy barriers. In contrast to force-separation-traces, such barrier position histograms can be averaged to investigate details of the unfolding potential. Averaging in contour length space preserves the details of the energy landscape due to the fluctuation independence of the individual traces in this representation. With known monomer length, this new coordinate can be scaled to the number of polymer units to localize the exact position of these energy barriers.

Several models have been developed to describe the elastic response of unfolded polypeptides in force-separation-traces. By solving these relations for contour length, the transformation function can be obtained with which the transformation from the separation space to the contour length space is performed. One of the most common models is the worm-like chain model (WLC) introduced by Bustamante et al. [152]. The entropic elasticity of the unfolded protein is determined by fitting eq. (1.26) to the measured traces of force versus separation, i.e. the distance between the polymer attachment points at the tip apex and at the surface (which corresponds to the piezo driving distance minus the tip deflection):

$$F(L, L_C) = \frac{k_B T}{p} \cdot \left(\frac{L}{L_C} + \frac{1}{(1 - L/L_C)^2} - \frac{1}{4} \right) \quad (1.26$$

with the polymer contour length L_C, and the persistence length p as fit parameters, $k_B T$ is the thermal energy. A typical value for the persistence length of a polypeptide which is a measure of the molecule's stiffness is 0.5 nm, which is also found in the analysis of the surface induced folding of engineered spider silk protein eADF-4 in chapter 6. However, it has been shown that the persistence length has to be adjusted to different force regimes [153]. Hence, modifications to this model like the quantum mechanical WLC have been developed that explicitly account for the backbone elasticity of the polymer and allow for a more accurate fit in the high force regime [154].

$$F(L_C) = \sum_{n=1}^{\infty} \gamma_n \left(\frac{L_C}{L_0} - 1\right)^n \qquad (1.27)$$

hereby, L_0 is the unit cell length, γ_1 represents the linear elastic modulus of the stretched polymer while the other coefficients are nonlinear corrections which become important at the higher force range probed in the experiments. The result of the quantum mechanical ab initio calculations at zero temperature showed already good agreement with the experimental curves in the high force regime (> 1 nN) for n = 2 and the corresponding polynomial representation reads:

$$F(L_C) = \gamma_1 \left(\frac{L_C}{L_0} - 1 \right)^1 + \gamma_2 \left(\frac{L_C}{L_0} - 1 \right)^2 \quad (1.28)$$

For peptides the elastic constants were found to be $\gamma_1 = 27.4$ nN and $\gamma_2 = 109.8$ nN [154].

In each model the force $F(L, L_C, \ldots)$ depends on the separation L, on the contour length L_C, and on parameters that are fixed for a particular experiment, e.g. temperature. Each data point $[F_i, L_i]$ from the extension space is then transformed into contour length space $[F_i, L_{Ci}(F_i, L_i)]$ under the constraints $F, x, L_C > 0$ and $x < L_C$. This is possible because for every value F_i there exists only one pair of variants $[L_i, L_{Ci}]$.The transfer function for the WLC model is obtained simply by solving eq. (1.26) for the contour length. The derived distributions of unfolding forces provide useful information on the unfolding barrier, the equilibrium rate constants to overcome this barrier and the potential width in force direction.

1.7 Probability distributions of unfolding forces

The process of unfolding a protein can be described as Markovian (Poisson) process [155] that has a force dependent probability for unfolding dP_U/dF. The force dependency comes from the additional linear potential due to the external force which causes a tilt of the energy landscape, and thus decreases the probability of bond survival [120]. As a consequence the barrier heights of folding and unfolding are altered. Under mechanical tension the unfolding of the peptide is favored while the refolding is decelerated (figure 1.7.1). This is the reason why only unfolding transitions are observed in a typical SMFS experiment, whereas refolding has only recently be detectable with much greater effort [156,157].

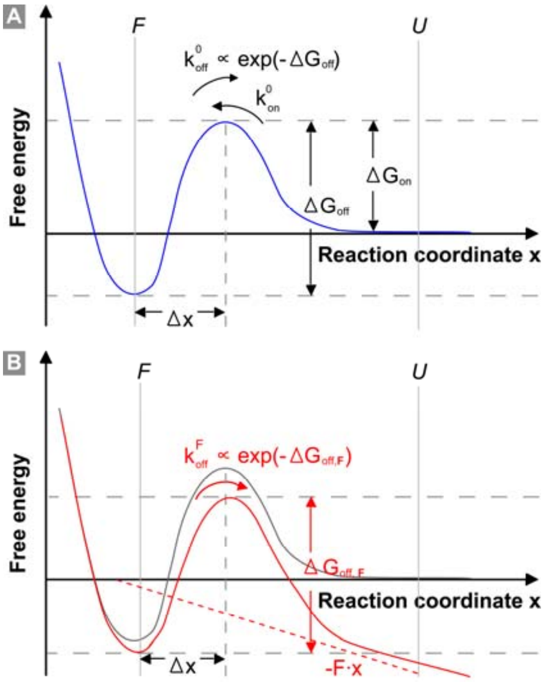

Figure 1.7.1: Two-dimensional energy landscape projected on the reaction coordinate x, here the pulling direction. The external force causes a tilt of the potential and the (un)folding probability is altered.

To determine the unfolding rate constant k^0 and the potential widths Δx, the respective unfolding force distributions are fit with a two-state model including the WLC-elasticity of the polypeptide spacers as introduced by Evans and Ritchie [158]. For this purpose, one calculates the force-dependent unfolding rate constant k^{off} by using Bell's equation [159]:

$$k^F = k^0 \exp\left(\frac{-F\Delta x}{k_B T}\right) \tag{1.29}$$

where k^0 denotes the unfolding rate at zero force F, Δx is the potential width and $k_B T$ is the thermal energy. The probability distribution dP_U/dF for a one-barrier binding potential then reads:

$$\frac{dP_U}{dF} = \frac{k^0}{dF/dt} \exp\left(\frac{-F\Delta x}{k_B T}\right) \cdot \exp\left(-\int_0^F \frac{k^0}{dF'/dt} \exp\left(-\frac{F\Delta x}{k_B T}\right) dF'\right) \tag{1.30}$$

where dF/dt denotes the loading rate. The loading rate is calculated from a WLC model with fixed polymer contour lengths obtained from the transition barrier histogram. The force-loading rate is determined recursively from eq. (1.26) with

$$t(L) = \frac{L + \frac{F(z)}{k_c}}{v_z} \tag{1.31}$$

k is the cantilever spring constant and v_z is the pulling velocity. Substitution of L by t in eq. (1.11) using eq. (1.31) yields the force as function of time F(t). After differentiation we get dF/dt.

Finally, the transition barrier height ΔG can be calculated using the Arrhenius equation:

$$\Delta G = -k_B T \ln\left(\frac{k^0}{A}\right) \tag{1.32}$$

with A being the Arrhenius pre-factor, which was determined for proteins to be of the order of $A=10^7$-10^9 [148,160,161]. This value has not been measured with satisfying precision yet and depends on the corrugation of the underlying energy surface. We will make use of eqs. (1.29) - (1.32) in chapter 6 to analyze the folding characteristics and the energy landscape of a single spider silk molecule. Alternatively, these information can be obtained by measuring the unbinding force as a function of the loading and applying the Bell-Evans or Kramers model [161]:

$$F = \frac{k_B T}{\Delta x} \ln\left(\frac{dF/dt}{k^0} \frac{\Delta x}{k_B T} \right) \qquad (1.33)$$

Because of the finite probability of the bonds to dissociate spontaneously, as the molecule acquires sufficient thermal energy from its surrounding thermal bath to overcome its activation barrier, such bonds will fail at any level of pulling force if a force is applied for a sufficiently long time span. Hence, as mentioned above, the strength of such a bond depends on the time derivative of the force, the so-called loading rate. Conceptually this picture is equivalent to the tilting of the energy landscape by the applied force in figure 1.7.1 [162].

1.8 Equilibrium theory of cosolute binding onto a single polymer

It is only recently that the theoretical aspects of the thermodynamics of the binding of small molecules onto a polymer under tension have been discussed[163]. Cosolutes associated with the polymer surface exhibit a higher concentration along the polymer contour in comparison to the bulk solution. The excess of the cosolutes per unit area, the Gibbs surface excess Γ, is given by the Gibbs adsorption isotherm that relates Γ to the chemical potential μ of the cosolute in solution and to the surface tension[164]. To obtain the one dimensional form of the Gibbs adsorption isotherm suitable to describe the adsorption of ligands onto a one-dimensional polymer, the surface tension is replaced by a line tension that is related to but not identical with the pulling force F_{Des}. In addition, the surface excess per area is replaced by a surface excess per length. This yields the following equation for a single molecule under fixed desorption force F_{Des} in line with eq. (17) from ref. [163]:

$$\Gamma = \theta / d = -\left.\frac{\partial \tau}{\partial \mu}\right|_{F_{Des}} \qquad (1.34)$$

where τ is the line tension of the polymer. In order to connect the Gibbs equation with a physical model for the adsorption process we split Γ into a dimensionless fraction of binding sites occupied by ligands θ and an adsorption site length at saturation d. In the following, we will use eq. (1.34) to predict the binding thermodynamics of ligands onto polymers based on the measured desorption force (chapter 7).

We can integrate eq. (1.34) to obtain the line tension τ as a function of cosolute chemical potential, which allows us to analyze cosolute binding without the need for theoretical assumptions beyond the existence of thermodynamic equilibrium. However, we have to discuss the dependence of θ itself on chemical potential of the cosolute. Assuming negligible cosolute interactions, identical adsorption sites on the polymer with equal free energy of adsorption, and no more than a monolayer of associated cosolutes, this relationship is given by the Langmuir isotherm [164]:

$$\theta = \frac{Ka}{1+Ka} \tag{1.35}$$

where a = exp(μ/k_BT) denotes the ligand activity and K is the association constant of the ligand to the polymer. K is defined by the ratio of an adsorption rate constant and a desorption rate constant, K = K_{on} / K_{off} (cf. figure 7.1.1). With regard to the AFM measurements with non-ionic cosolutes, the above assumptions are not considered to be a limiting simplification. A discussion of the validity of the Langmuir model in the case of electrolyte solutions and charged cosolutes can be found in ref. [84] and for two domain ligands in ref. [165].

Substitution of θ in eq. (1.34) by eq. (1.35) leads to the analytical solution of the Gibbs isotherm which reads:

$$\tau = -d^{-1} k_B T \ln(1+Ka) \tag{1.36}$$

Note that the line tension is not the stretching force but rather the chemical potential per unit length of the polymer. Considering the equilibrium between the surface-adsorbed polymer state, characterized by ligand association constant K_S and adsorbed distance d_s, and the bulk polymer state, characterized by ligand association constant K_b and adsorbed distance d_b, gives rise to the line tension difference Δτ:

$$\frac{\Delta\tau}{k_B T} = d_S^{-1} \ln(1+aK_S) - d_b^{-1} \ln(1+aK_b) \tag{1.37}$$

This line tension difference is the main contributing factor to the ligand-activity dependent contribution to the desorption force F_{Des} measured in a single-molecule experiment. A small correction arises from the stretching contribution to the line tension difference which depends on F_{Des}. Fitting eq. (1.37) to the measured forces as a function of ligand activity allows us to determine the binding distances d_b, d_s and the association constants K_b and K_s, especially if results for different surfaces are fitted simultaneously with the additional constraint of K_b and d_b being equal for all surfaces tested (see chapter 7).

The Gibbs free energies of binding to a single binding site on the polymer can then be calculated for both states according to

$$\Delta G = -RT \ln(K) \tag{1.38}$$

wherein R is the molar gas constant.

1.9 All atomistic molecular dynamics simulations

For the case of single-polymer desorption as performed in a typical AFM experiment, MD simulations with explicit water can be performed for exactly the same system studied experimentally because the number of water molecules displaced is small and equilibration is fast [49]. In experiments only the sum of the various contributions to the total attractive interaction is measured. In the simulations, on the other hand, it is possible to additionally disentangle interactions between water, solvent, and the surface from each other [49,166]. However the timescale of pulling in simulations is typically of the order of 1ms^{-1} and 5 to 6 orders of magnitude higher than in the AFM experiment.

In the former Derjaguin-Landau-Verwey-Overbeek (DLVO) approach [167], the force between uncharged bodies immersed in water is explained solely in terms of dispersion or van der Waals interactions. Nowadays, solvent mediated effects are thought to play an equally or even more important role [30,31]. Insight into the interplay between the different contributions and thus into the nanoscopic mechanism underlying the hydrophobic effect can be gained from simulations: in ref. [49] Horinek et al. showed how the various energetic contributions stemming from the interactions between peptide (P), surface (S), and water (W) atoms sum up to the total desorption energy per peptide monomer, U, according to $U = U_{PP} + U_{PW} + U_{WW} + U_{PS} + U_{WS}$ (figure 1.9.1). We knowingly call the resulting interaction a free energy of desorption to distinguish it from the standard adsorption free energy. As will be discussed in more detail later on, the desorption force measured with the AFM includes the polymeric response in the stretched state, whereas the reference state of the ordinary polymer adsorption scenario is the strain free polymer configuration in solution. However, as we will show in the following, this difference is generally small and makes a distinction become redundant (see also eq. (1.9)).

We distinguish process I, in which the peptide is brought from the adsorbed state to a state that is stretched between surface and terminal peptide group that closely mimics the SMFS experiment. In process II the peptide is transferred from the adsorbed state to an unperturbed bulk state, which correctly describes the thermodynamic adsorption equilibrium of a peptide in solution. For both processes I and II the water–water and peptide–surface contributions to the internal energy, U_{WW} and U_{PS}, are positive and larger than the resulting total energy U and free energy A. Both the van der Waals interaction between surface and peptide (included by means of the simulation force field in a heuristic fashion[49]) and the solvation energy are thus important. However, they are considerably compensated by the water–surface and peptide– water contributions, U_{WS} and U_{PW}. Interestingly, the peptide–peptide interaction, U_{PP}, often neglected in theoretical considerations, is quite large and differs in sign between the two desorption scenarios.

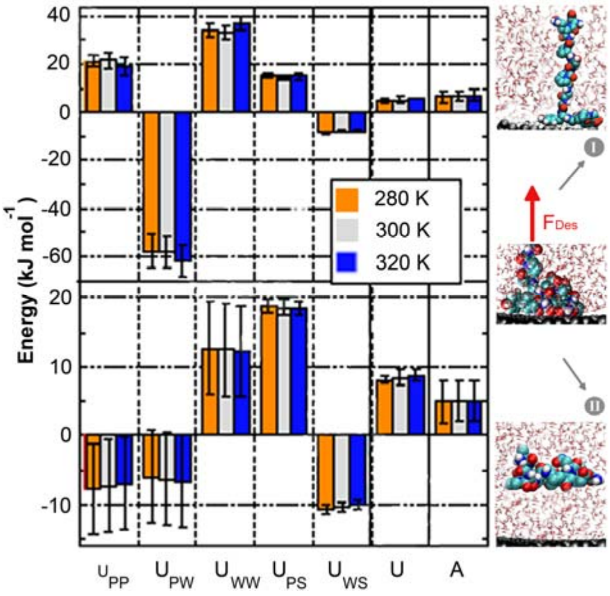

Figure 1.9.1: Decomposition of the total internal energy per monomer, U, into the contributions from interactions between peptide (P), surface (S), and water (W) for three different temperatures and compared with the free energy A. The figure is derived from ref. [49].The upper histogram gives the energy cost for desorbing peptide fragment 3 into a stretched conformation (process I), similar to the AFM experiment, and the lower histogram has the totally relaxed and solvated peptide conformation as the reference state, as applicable to equilibrium adsorption from a bulk solution (process II). In both cases, the various internal energy contributions are larger in magnitude than the total internal energy U, which is similar for both scenarios.

From the free energy A it follows that the entropy S = (U - A)/T is negative (unfavorable) for process I, i.e. the system loses entropy as the peptide is brought into the stretched conformation, but is positive (favorable) for process II, i.e., the system gains entropy as the peptide leaves the surface adsorbed state. This difference in entropy can be explained by the conformational entropy of the peptide, which is maximal in the bulk state, intermediate in the surface-adsorbed state, and minimal in the stretched state. We will discuss this unfavorable entropy observed in the AFM experiment again in chapter 5 when we elucidate the origins of entropy convergence.

Horinek et al. stated that the good agreement between $U_{PS} + U_{WS}$ and U is most likely coincidental [49]. It is related to the fact that the peptide–peptide interaction U_{PP} in the present case almost exactly cancels the water contributions $U_{PW} + U_{WW}$. However, the comparison of our experimental desorption forces with these simulations necessitates several simplifications and assumptions. (i) Because of simulation time constraints, pulling rates in the simulations are orders of magnitude higher than in experiments. Therefore, a direct comparison of desorption forces from simulation and experiment is only justified if thermal equilibrium is achieved in the pulling simulations. By carefully considering different desorption rates and comparing with static simulations, it was shown that adsorbed peptides equilibrated very fast on simulation time scales on hydrophobic surfaces [49]. This situation was very different on hydrophilic surfaces, where equilibration could not be achieved on the nano-second time scale and equilibrium desorption free energies could not be determined by simulations. (ii) In the simulations the peptide strand is necessarily much shorter than in the experiment.

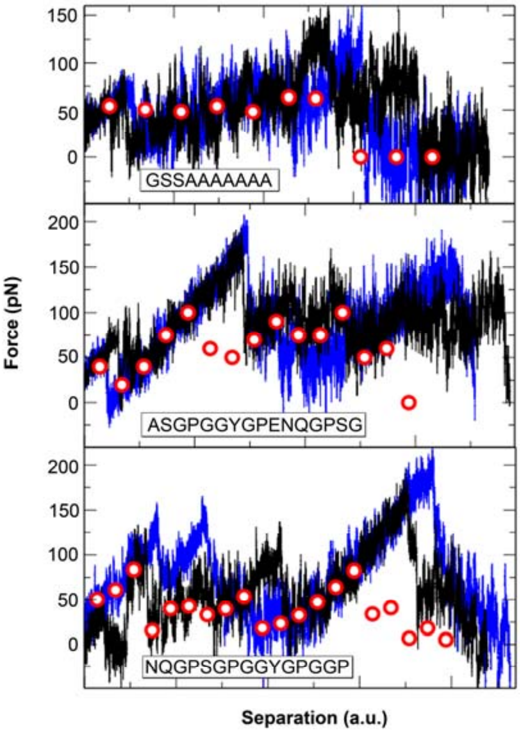

Figure 1.9.2: Desorption force F_{Des} of three eADF-4 fragments on hydrophobic diamond as a function of AFM tip separation L obtained with static simulations (blue points), where the restrain potential acting on the first amino acid is at a constant position for 8 ns, and two dynamic pulling simulations (black and red curves), where the restrain potential is moved away from the surface at a rate of v_0 =0.1 m/s. The sequence of each fragment is given in terms of the one-letter amino-acid notation in each plot. The average desorption forces from static simulations are 54 pN for fragment 1, 64 pN for fragment 2, and 40 pN for fragment 3. The figure is taken from ref. [96].

While in the experiment the already desorbed peptide strand acts as a flexible tether that averages out the force acting on the AFM cantilever, leading to flat force plateaus, in the simulations the molecular tether is much shorter. As a consequence the sequence dependence of the adsorption strength is clearly resolved with a spiky force response that is related to the hydrophobicity variation, as has been demonstrated for a monomer of spider silk eADF-4 (C16), which was split into three pieces for computational efficiency (figure 1.9.2).

The unexpected simulation result is that almost a complete cancellation of individual energy contributions takes place, meaning that the hydrophobic effect results from subtle balancing. Specifically, both the water structural forces and the direct dispersion interactions between polymer and surface contribute significantly to the total hydrophobic attraction. Understanding hydrophobicity thus involves unraveling the interplay between those two factors. This is done experimentally by employing single molecule sensors characterized in the next chapter to study hydrophobic hydration as well as dispersive forces in more detail (chapter 3).

Chapter 2

Single Molecule Adhesion Mechanics

In this chapter we characterize the molecular sensor consisting of a single polymer covalently bound to an AFM cantilever tip. The equilibrium desorption provides sharply peaked force and length distributions. The characteristic detachment length of a recombinant protein is used to unambiguously identify the probe molecule. Tip passivation and equilibrium conditions make the study of desorption free energies possible. Our investigation of the nano-tribology of individual molecules on corrugated surfaces reveals the absence of any notably friction on the molecular scale as long as velocity independent force plateaus are observed.

Apart from its value as a model system with well characterized and easily tunable parameters to study hydrophobic phenomena, this kind of molecular sensor device is of direct relevance for a number of technical applications. Among them the adhesion of polymers onto solid substrates is of particular interest as it becomes more and more important in modern technologies, especially to create new composite materials, resins or sensor devices such as lab-on-chip applications. In most composite materials proper adhesion strength in between the composites is crucial for the functionality of the compound. For example the adhesion of varnish has to be extremely strong, while adhesion of active agents onto drug eluting implants should be reversible and the adsorption of proteins onto the walls of biomedical devices for in vitro diagnostic systems should not take place at all. In addition, most materials such as glues should keep up their functionality in aqueous environment or like in medical technology even work at physiological conditions, which underlines the importance of the influence of water and salt. Up to now it has not been possible to calculate or predict the adhesion of a compound of materials due to the complex interplay of interactions. Therefore, we have had to rely on destructive testing methods for the adhesion of polymer coatings [168-170]. In the following we will use a single molecule sensor to investigate polymer-surface interactions on the molecular scale. We will show that we overcome all limitations that made force measurements across liquids by AFM “an art form” [53]: The main challenges with single molecule experiments on hydrophobic substrates are the unspecific interaction between AFM-tip and substrate, aggregation of the hydrophobic polymers and adsorption of contaminants present in air or dispersed in solution (most contaminations will quickly settle on the water-substrate interface). Finally, air bubbles are of importance – they considerably influence the long range hydrophobicity[167,171]. Despite these challenging problems the need for detailed single molecule investigations which are comparable to theory justifies the effort as the hydrophobic effect manifests itself in many fields, already described in the introductory section and section 1.1.

2.1 Equilibrium desorption of a single molecule

The covalent attachment of single polymers onto an AFM-tip via flexible linkers of poly(ethylene glycol) (PEG) [172-174] is described in detail in the Materials and Methods section (Appendix C). PEG itself has already been studied extensively in SMFS experiments [175]. Covalent attachment of the polymer via a peptide bond provided the long-term stability necessary to measure for hours with one and the same molecule under different conditions. The principle of measurement is illustrated in figure 2.1.1 where a single polymer is covalently attached to an AFM-tip, brought into contact with a solid substrate in electrolyte solution and then pulled from the solid surface. In the following, we call the combination of AFM-tip and single polymer the molecular sensor. Before describing the influence of various salts and polymer and surface properties on the adhesion, we give a thorough characterization of our molecular probes.

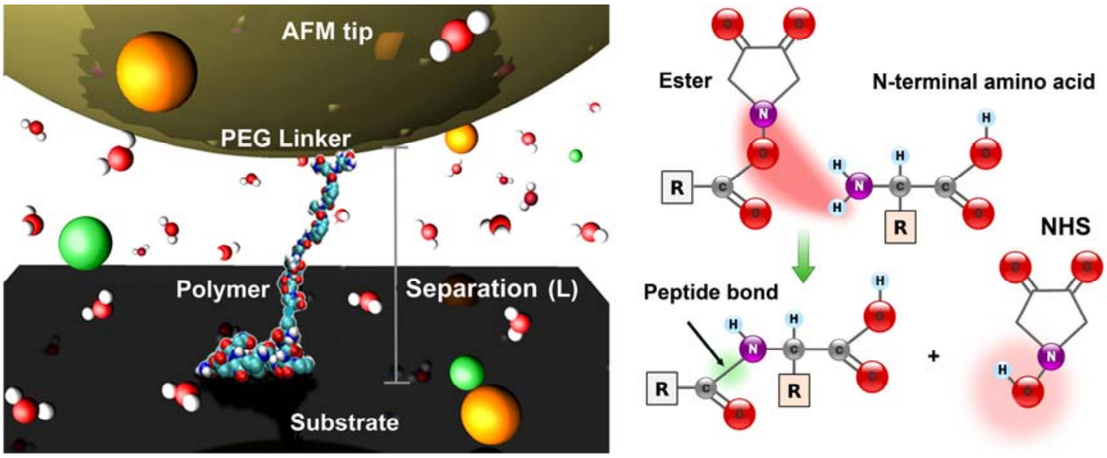

Figure 2.1.1: Scheme of a single molecule desorption measurement in electrolyte solution (left) and sensor coupling chemistry (right).

Figure 2.1.2 (A) shows the superposition of twenty representative force separation traces obtained by SMFS of eADF-4 (C_{16}) [176,177], a genetically engineered variant of the spider silk protein ADF4 (Araneus diadematus fibroin) of the garden cross spider (see section D.2) in aqueous NaCl solution on hydrogenated diamond. They have a regular sequence, a defined length and can readily be purified in adequate quantities [177]. Adhesion measurement of the single molecule at the interface is not disturbed by cavitation as it is in more macroscopic force detecting devices.[30]

For low separations, there is strong direct tip-surface interaction, which is difficult to interpret and undesired in the present context. It can be suppressed or even prevented by tip passivation (see section 2.6). For separations above approximately 50 nm, the force becomes independent of the separation until it abruptly drops to the zero line when the polymer finally detaches from the surface in a single step (detachment or rupture length). The constant plateau force in the middle region of the force-separation curve in figure 2.1.2 (A) comes from attractive polymer-surface interactions. The area under the plateau corresponds to the desorption free energy per unit length (see next paragraph).

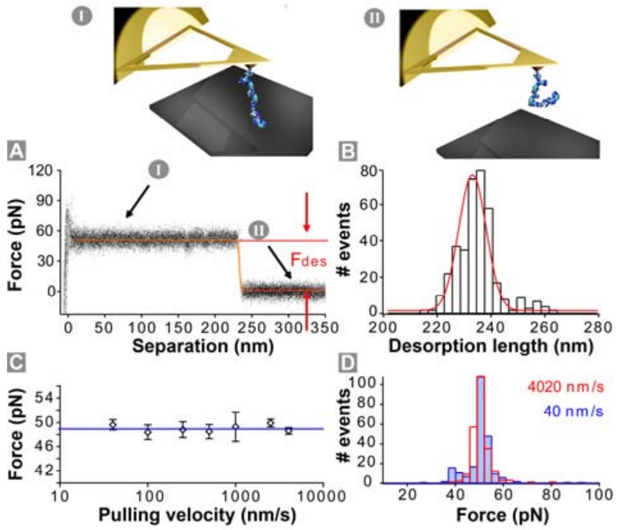

Figure 2.1.2: Equilibrium desorption of a polymer from a solid substrate. (A) Superposition of 20 typical force-separation traces of eADF-4 on H-terminated diamond. The detachment of the molecule from the surface is indicated by a sudden drop of the force plateau to the zero line (at around 230 nm). The area under the sigmoidal fit to the trace (orange) gives the adsorption free energy per molecule. (B) The Gaussian distributed desorption length is sharply peaked and reproduces the molecular length of eADF-4 (plus PEG spacer) very well. (C) The mean desorption force derived from distributions of likewise Gaussian shape (D) is independent of pulling speed.

A multi step appearance of the force separation trace would indicate desorption of multiple molecules starting with the shortest and ending with the longest molecule. The detection of only a single plateau in all force-separation traces confirms that we have by preparation only one molecule attached at the tip apex. This allowed recording up to 2000 force extension traces with one and the same molecule in various buffers. The long-term stability of the sensor reached by covalent bonds allowed a direct comparison of the desorption forces under different buffer conditions. The analysis of several hundred of single step traces yielded sharply peaked plateau force distributions (figure 2.1.2 (D)) and desorption lengths (figure 2.1.2 (B)). By taking advantage of this characteristic, the genetically engineered spider silk molecule is clearly identified by its well defined length. The desorption length of eADF-4 is Gaussian distributed (figure 2.1.2 (B)) and sharply peaked. The mean desorption length of 231 nm amounts to 89% of the expected polymer contour length of eADF-4 of 210 nm (assuming a length of 0.365 nm for each of the 575 amino acids) plus 49 nm PEG spacer length in its fully stretched conformation (136 CH_2CH_2O-monomers with 0.36 nm per monomer in the all-trans conformation, which is almost exclusively occupied at forces above 60 pN) [175]. Considering the polydispersity of the PEG linker of about 1.13, this is in good agreement with previous theoretical estimates (see section 1.5). The slight deviation from the total contour length is caused by conformational chain fluctuations during desorption. The defined length of the protein provides a good finger print of the investigated polymer and allows an unambiguous characterization of the acting forces. Upon restriction to plateaus with the expected rupture length plus minus 50% very small force distributions with an error of less than 10% are obtained (figure 2.1.2).

The observation of velocity independent plateaus of constant force is the hallmark of pulling a single molecule from the surface in thermodynamic equilibrium. This is in contrast to the stretching of individual molecules fixed between AFM tip and substrate via covalent bonds, receptor-ligand binding or polymer entanglement, which takes place under non-equilibrium conditions [145,178].

There have been previous attempts to explain the occurrence of force plateaus in single chain desorption experiments: one is based on pulling a charged chain from a charged surface [134,179], and another is based on the rate of extension [135,180]. Châtellier, et al. describe the pulling of a single polyelectrolyte chain off a charged surface using scaling arguments [134]. They argued that the force profile reaches a plateau for extensions beyond the Debye screening length of the solution. The magnitude of the plateau force is indicative of the energy required to transfer monomers to the bulk solution from the electrical double layer near the surface. These explanations have been experimentally verified using AFM on polyelectrolytes adsorbed onto charged surfaces. Hugel et al. showed the dependence of the magnitude of the force plateau upon the polymer charge and electrolyte concentration. In a generalized theoretical treatment, Haupt et al. described the force profile of a single chain which adsorbs onto a surface in a series of loops [180]. At separation rates which are faster than the rate of dissociation of the monomer-surface contact, the force profiles appear as a consecutive series of Langevin events, each corresponding to the stretching of an isolated loop of the chain. However, at slower separation rates where the monomer-surface contact has enough time to detach and re-form many times on the time scale of the pulling experiment, the force measured provides information about the strength of the contacts averaged over the length of the chain. In other words, if the rate of withdrawal of the AFM tip is slow on the scale of the internal relaxation times in which the polymer chain relaxes to its internal free-energy minimum, the force will be constant, in line with the theoretical considerations of Staple et al. (section 1.4). Furthermore, these authors claimed a relation between the appearance of plateaus in the force-separation traces and the conditions of the suspending liquid being “poor” for the solvation of the molecule [110].

In the following, we will reconsider the requirements for the force being independent of separation based on our experiments with different polymers on various substrates under varying solvent conditions. As can be seen from Figure 2.1.2 (C) and (D), the mean force obtained from Gaussian distributions is not rate dependent, but rather stays constant over a wide range of pulling speeds. This observation already points to a negligible molecular friction and absent energy dissipation of eADF-4 on H-terminated diamond.

This finding is corroborated in figure 2.1.3, where a single eADF-4 molecule is partially desorbed from a diamond surface and afterwards readsorbed. Starting with the molecule in its adsorbed state, the AFM tip was moved away from the surface, leaving about 120 nm of the polymer chain (about half the polymer contour length) adsorbed at the surface (time index 0 s). The tip was further retracted 80 nm with 1 µm/s (1) and moved again the same distance towards the surface with the same velocity (2). We then waited for 7 seconds (0 µm/s) while the molecule was stretched between surface and tip apex (3). Finally, we performed another retract-approach cycle over a distance of 80 nm at a third velocity of 4 µm/s (4)-(5).

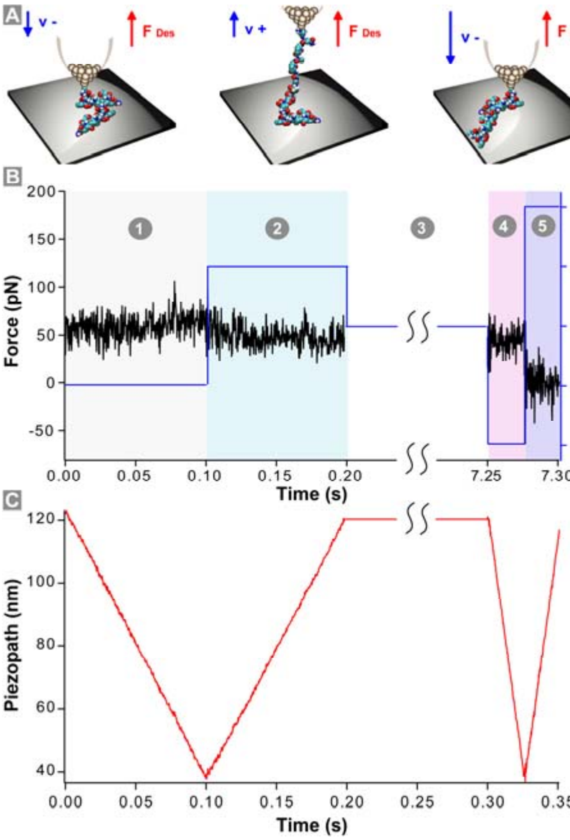

Figure 2.1.3: Velocity independence of equilibrium desorption force. (A) Scheme of a retract approach cycle with eADF-4 bound to the AFM tip and adsorbed onto the substrate. (B) During desorption, the force plateau is neither affected by pulling speed nor by pulling direction. (C) The movement of the piezo actuator. A negative slope indicates the approach of cantilever and surface, a positive slope represents the retract phase.

During this procedure the recorded plateau force remained constant until the force suddenly dropped to the zero line in a single step indicating a single protein detaching from the surface.

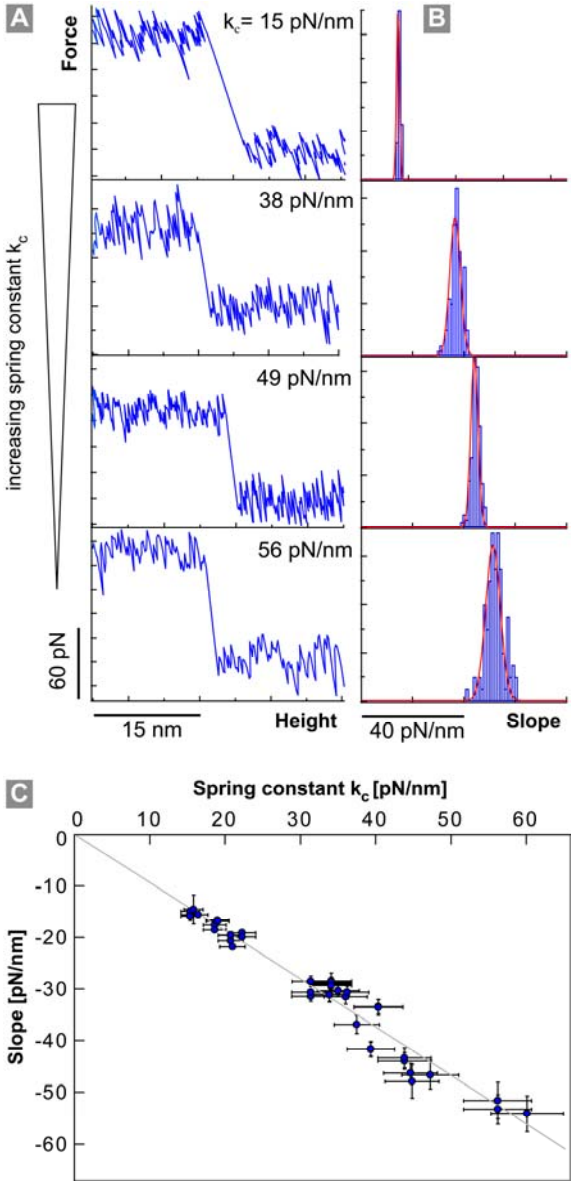

Figure 2.1.4: Variation of the detachment slope with cantilever spring constant k_c. (A) With increasing stiffness of the cantilever, the slope of the retraction curve becomes steeper and (B) the average value is shifted to higher values. (C) Detachment slope as a function of the cantilever spring constant k_c. The graph depicts 45 different desorption experiments of eADF-4 with varying PEG linker length, salt concentration and temperature. The slope equals $-k_c$ regardless of the experimental conditions.

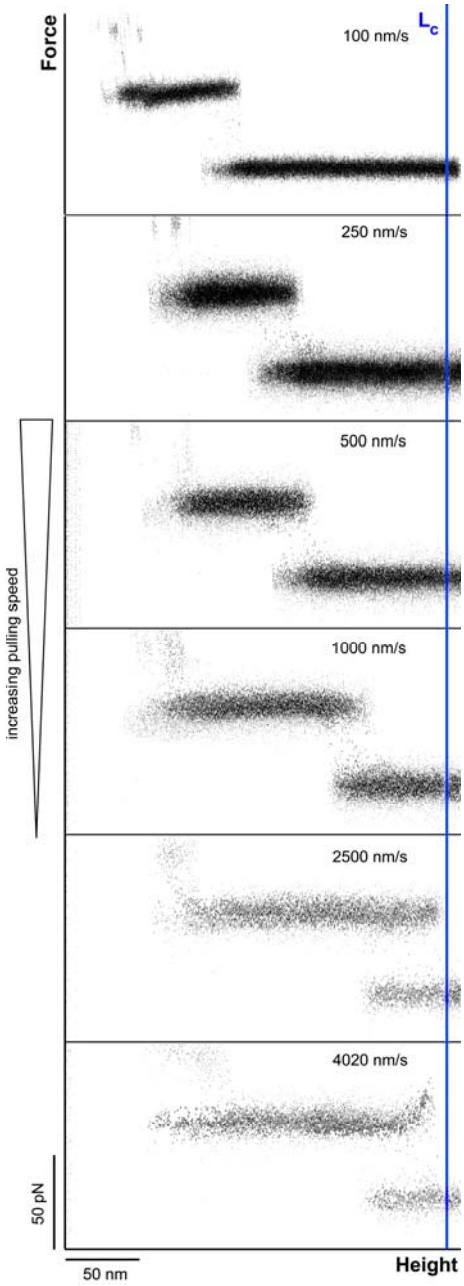

Figure 2.2.1: Dependence of the desorption length on the pulling velocity. For each experiment with different velocity the superposition of 20 typical retract curves is shown. With increasing retract speed the plateau elongates and the measured detachment length L_{max} approaches the contour length L_c of protein plus linker. The data acquisition rate of $5 \cdot 10^6$ Hz was kept constant.

Note that the recorded force likewise acts on the cantilever during re-adsorption (v-) as it does during desorption (v+) and is therefore not only independent from pulling velocity, but also from pulling direction. These results imply that the adsorbed chain section reaches equilibrium on the time scales of the experiment, and define the observed force plateaus as equilibrium desorption. As long as velocity independent force plateaus are obtained, molecular friction is low and lateral movement is not constrained.

In addition, the prediction of the thermodynamic equilibrium model (section 1.4) was tested by plotting the average detachment slope as a function of the estimated spring constant k_c for 45 different experiments and cantilevers with bound eADF-4, respectively (figure 2.1.4). The detachment slope reflects the cantilever spring constant one to one independently of the length of linker used, of the pulling velocity (500 or 1000 nm/s), of the ionic strength of the electrolyte solution (ranging from 20 to 500 mM) and of the temperature (25 to 47 °C).

2.2 Indications of non-equilibrium effects

We now address the situation where internal relaxation times are slow on the timescale of pulling the polymer off the surface. In this case, as discussed in section 1.5, non-equilibrium effects will show up: The maximum detachment length increases with pulling speed in a characteristic sigmoid shape, from its equilibrium value to the full contour length. At the highest pulling speeds there is a terminal enhancement of the force (see figure 2.2.1).

For the experimental data on eADF-4 a least squares fit (eq. 1.25) with $h_{eq} = L_c/2$ allows us to determine the relaxation time of the polymer. We measure $L_c = 226 \pm 9$ nm and $v_s = 565 \pm 145$ nm/s (see figure 2.2.2). This implies that the relaxation time $\tau = \omega_0^{-1} = L_c/v_s = 0.4$ s. Its persistence length of 0.4 nm is much shorter than for DNA with 40 nm, making it more flexible and thus much slower in its relaxation. The relaxation time for DNA has been estimated to be of the order of 10^{-4} s [147] and a value of $2 \cdot 10^{-5}$ s has also been measured with SMFS [181]. (Furthermore, the relaxation time measured for DNA was with respect to stretching (local deformations), whereas the relaxation time presented here is measured with respect to a desorption process involving the whole chain.)

We find that weakly adsorbed polymers, such as spider silk, are well described by a local equilibrium while in contact with a solid surface. In this situation the dominant non-equilibrium effect is the complete detachment of the chain from the surface, which is well described as a two-state Markov process. Although the experimentally observed dependence of the detachment length on pulling speed is logarithmic, the complete dependence is necessarily sigmoidal: it must converge to the equilibrium limit and contour length of the polymer in the limits of low and high pulling speed, respectively.

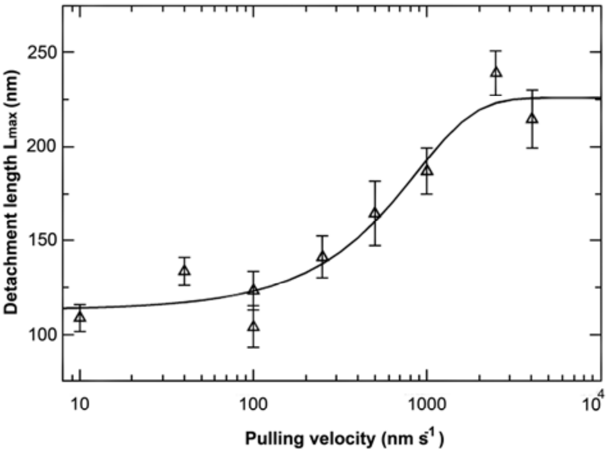

Figure 2.2.2: Detachment length as a function of pulling velocity. The red curve is a fit of eq. (1.25) to the experimental data with $L_c = 226 \pm 9$ nm and $v_s = 565 \pm 145$ nm/s.

2.3 Desorption free energy of single polymers

Due to the equilibration on experimental timescales, the forced desorption can be directly related to the adsorption equilibrium of polymers and their adsorption free energy [49,132]. The experimental equilibrium conditions allow free energies of adsorption to be extracted from the measured traces in a simple manner, forming the area under the force plateau (figure 2.3.1). For a better comparability, this energy is given in units of k_BT per monomer and amino acid, respectively (1 k_BT equals about 2.4 kJ mol^{-1}). Aside from a small entropic conformational contribution related to the polymeric force response (cf. eq. (1.9)), the average adsorption free energy per amino acid amounts to:

$$W = F \cdot l \tag{2.1}$$

The monomer length for allylamine is l = 0.25 nm and for an amino acid l = 0.37 nm [132,133].

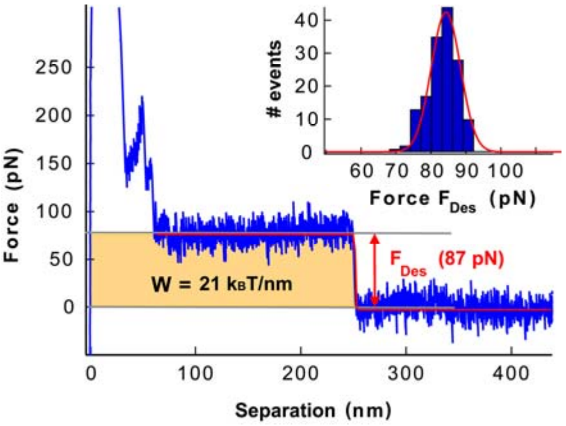

Figure 2.3.1: Molecular desorption free energy. A Typical AFM force-separation trace for the desorption of eADF-4 from polished 316L in PBS at 36.5°C is shown. The step height of a sigmoidal fit to the trace directly corresponds to the desorption force in thermal equilibrium, while the area under the force plateau corresponds to the desorption free energy of the molecule (W). The inset shows the Gaussian distribution of desorption forces obtained from 150 approach-retract cycles.

2.4 Macromolecular friction of single polymers on solid surfaces

In the case of negligible friction, the polymer maximizes its contact area to the surface under the constraint that its end is attached to the AFM tip. Here, we presume that the system is given enough time to equilibrate as evidenced by our experiments. For unfavorable entropies balancing enthalpies favorable for adsorption, the polymer might exhibit a more complex conformation when making contact with the surface. Partially folded segments forming loops in solution perpendicular to the surface plane are therefore not considered in the following discussion and we can define an angle ϕ between the desorbed part of the polymer and the surface normal (figure 2.4.1). The polymer will be peeled off vertically in case of vertical cantilever motion. For non-negligible friction, the angle ϕ will deviate from zero. For a constant tip velocity v_z the sliding friction coefficient per unit length ζ can be estimated from the experimental data[142] :

$$\gamma = \frac{v_z \xi L_C}{W} \qquad (2.2)$$

where L_C is the contour length on the surface and W is the adsorption free energy of the polymer per unit length. Thus, γ is a measure of the ratio of friction *vs.* adsorption strength and thus of the angle ϕ between polymer chain and surface normal. Figure 2.4.1 illustrates both scenarios: low friction (blue) and high friction (green).

An important result of ref. [141] is that, as soon as ϕ deviates detectably from zero, no plateau force will be measured. This is the case for $\gamma < 0.1$. The upper limit of the friction coefficient becomes $\zeta_{max} \approx 1.3 \cdot 10^{-8}$ kg/s. The fact that in our observations the force-separation traces always exhibit perfect plateaus on all surfaces comprising polished and microporous steel (see also section 3.1) signifies that the polymer can freely glide over the surface and that the desorbed polymer chain stays almost vertically ($\phi \approx 0$) aligned between tip and surface (figure 2.4.1 (A), blue trace).

In case of a corrugated surface a nonzero attachment angle is of particular interest: as can be seen from Figure 2.4.1 (B) the molecule fills the pores of the rough surface as long as the angle ϕ is very small (blue trace). However at a higher friction (which was not observed in the present case) the polymer would desorb from concave regions on the surface during movement and thus leave uncovered voids at the topographic pits (green trace). The latter mechanism has a significant impact on the failure of an adhesive joint at the material interface.

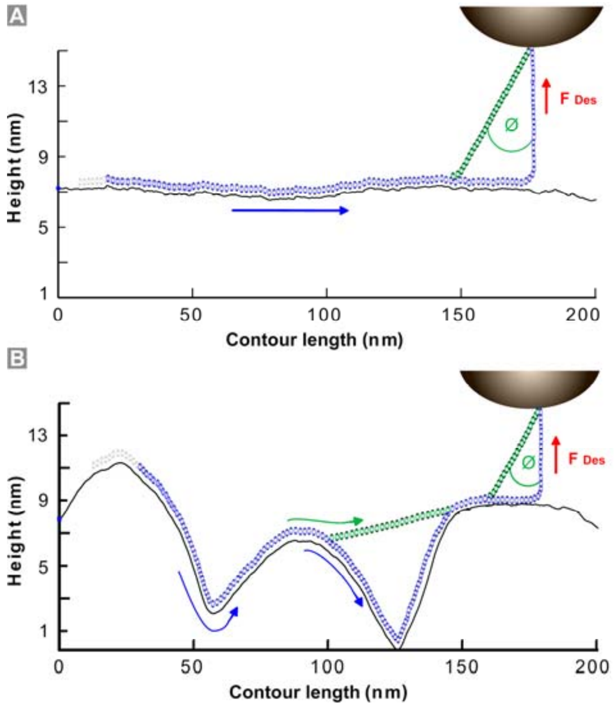

Figure 2.4.1: Schematic view of the desorption of a polymer along its contour on (A) polished and (B) rough steel (cf. figure 3.1.1). The polymer is drawn to scale, assuming a length of 0.4 nm for an amino acid of a polypeptide. The polymers are desorbed by an AFM tip that moves perpendicularly away from the surface (direction of the red arrows). For both surfaces we show the low friction case (a, $\phi \approx 0$) and the high friction case (b, $\phi > 0$). Note that molecular friction depends on the length of the adsorbed polymer chain.

In summary, Figure 2.4.1 illustrates our picture for the case of a polished (top) and a rough substrate (bottom) with a low ($\phi = 0$) and high ($\phi > 0$) friction coefficient. At low friction, the number of contact sites per monomer is about the same on both surfaces.

The derived picture is supported by our previous finding that the plateau force is independent of pulling velocity and pulling direction, which hints at a negligible friction on the molecular scale.

2.5 A comparison to MD-simulations

Further evidence for the absence of friction in the SMFS data is drawn from fully atomistic molecular dynamics simulations with explicit water. The lateral motion of spider silk fragments under the influence of an AFM tip was studied on hydrogenated (hydrophobic) and oxidized (hydrophilic) diamond surfaces [49,96].

The hydrophobic surface serves as a model system for surfaces that do not bear any local binding sites, whereas the hydrophilic surface provides local binding sites in the form of hydroxyl groups. These have the ability to form localized hydrogen bonds with the spider silk molecule. From the simulation results [141] it was inferred that in SMFS experiments of eADF-4 composed of 575 amino acids with a total contour length L = 210 nm with a pulling rate of 1 µm/s the expected friction forces are 2 fN on the hydrophobic surface and 60 fN on the hydrophilic surface. The presence of hydrogen bonding sites on the surface thus results in a 30-fold increase in the friction force, but friction effects still remain a negligible contribution to the overall desorption force.

The typical adsorption free energies of 7-8 k_BT in our experiment are surprisingly consistent with recent MD simulations [49]. The remarkable agreement between experiments and simulations showed that the latter are well capable of capturing the essence of the hydrophobic attraction and that this combined approach is well suited to solve the puzzle that hydrophicity still presents.

2.6 Sensor passivation - Suppression of unspecific tip adhesion

The fact that simultaneous interactions of the polymer with two surfaces – the substrate and the cantilever tip - have to be considered gives rise to differential adhesion aspects which might obscure the results [115]. Moreover, the strong interaction between the tip and the hydrophobic surface may mask the desorption event of a single sensor molecule. In the present study, unspecific interactions between the AFM-tip and the underlying substrate are suppressed by passivation of the tip with PEG. PEG is well known to prevent polymers such as polypeptides to adsorb onto PEG-grafted surfaces [182]. The efficiency of this protection layer depends on the grafting density, molecular weight and temperature [183-186]. Figure 2.6.1 shows the effect of PEG spacers differing in molecular weight on the suppression of this unspecific adhesion. Clearly, PEG with a molecular weight of 6 kg mol^{-1} or 10 kg mol^{-1} can significantly reduce the adhesion peak. In addition, by the use of spacers the probe molecule shifts away from the tip apex, increasing the separation at which the force drops to zero. Furthermore the sharpness of the distribution increases with spacer length, likely attributed to the passivating properties of the underlying PEG layer.

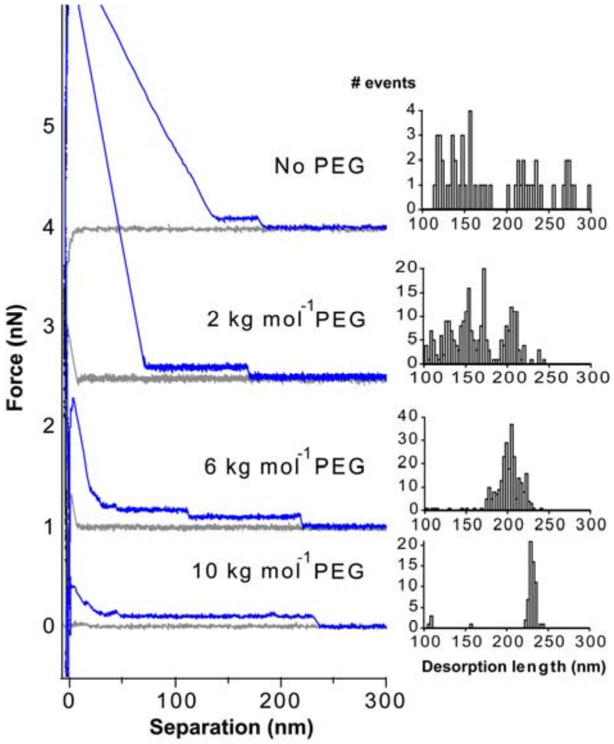

Figure 2.6.1: Tip passivation with PEG. We show four different desorption experiments with eADF-4 in 20 mM phosphate buffer. The cantilever is brought into contact with the surface (grey trace). Then the tip is retracted and the desorption force and rupture length of the molecule are measured (blue trace). We used different molar masses of PEG ranging from 2 to 10 kg mol^{-1}. The upper force-extension trace represents measurements with the protein directly coupled to the tip without spacers. As depicted by the corresponding length histograms in the right panel, the use of longer spacers not only causes the rupture length to increase but also results in a sharper rupture length distribution. Traces are vertically offset by 1 nN.

As might have been expected, the attraction of the probe molecule onto the tip surface resulted in a shortening of the detected detachment lengths and in a broadening of the distributions, as observed here for the bare tip or the low molecular weight PEG. Furthermore, the adsorption of and contamination with molecules from solution would result in a notable unspecific adhesion peak. Both can be successfully prevented by passivation with long enough PEG spacers.

2.7 Error estimate for SMFS experiments

In figure 2.7.1 (A) a couple of force-extension traces for the desorption of the polymers at different days and for different cantilevers are shown with the corresponding desorption force distributions. The solid substrate is an H-terminated diamond surface with a contact angle of about 80°, while the spider silk protein in this case is the eADF-4 motive. We used the 6 kg mol^{-1} PEG, because we got a much better yield of single molecules attached to the AFM-tip than with the 10 kg mol^{-1} PEG. The distribution of detachment lengths is always similar to the one shown in Figure 2.6.1 for the 6 kg/mol PEG. Shorter plateaus might result from strong unspecific adhesion of parts of the chain to the cantilever, or from an attachment at a larger end distance, e.g. one of the 18 glutamines contained in eADF-4 or an amine group in the centre region in case of poly(allylamine) (PAAm).

Relative values: When using one and the same cantilever for more than one experiment, any systematic error can be neglected, unless different cantilevers are compared (see last paragraph). The only remaining uncertainty still to be considered originates from the statistical nature of the desorption process. The statistics of the desorption process yields a Gaussian distribution of forces with a typical full width at half maximum of less than 2% for 100 recorded force plateaus, which is the minimum number of plateaus we used for one data point.

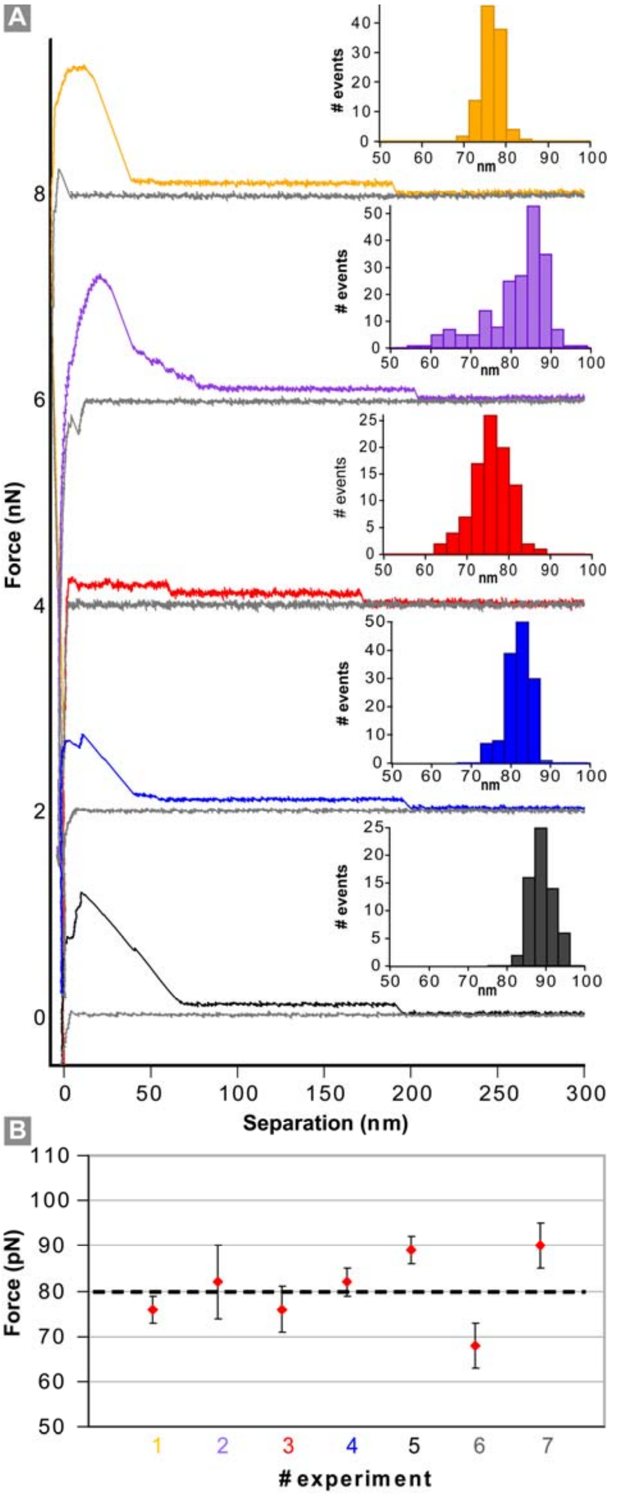

Figure 2.7.1: Data scattering due to cantilever calibration. (A) Different colors mark different experiments performed in 0.5 M NaCl solution with 6 kg mol^{-1} PEG linker. Each represented by a typical force-separation curve and force distribution. Traces are vertically offset by 2 nN. (B) The variation of the desorption forces from the experiments shown in (A). The dashed line marks the force average.

Absolute values: If we compare experiments from different days with different cantilevers the deviation between experiments is higher than the error from the force distributions, because of the uncertainties in the determination of the spring constant and invOLS. When averaging over at least five indentations, the contribution from the determination of the invOLS is less than 1%. The main error stems from the uncertainty in the determination of the cantilever spring constant. When two different cantilevers were used the standard deviation of two data points according to the theory of small samples is ±13% with a probability of 95.5% to find the true value within this range. If five experiments (instead of two) were carried out under exact the same conditions but again with different cantilevers the deviation was reduced to an uncertainty of ±10%. Finally, we performed one experiment seven times with different cantilevers. Figure 2.7.1 (B) displays the result of seven experiments and allows estimating the deviation in this case to be about 8%.

2.8 Concluding remarks

To gain a basic understanding of the interactions at the molecular level we developed an AFM-based molecular sensor which is capable of measuring forces between an individual polymer and different surfaces in a variety of different solutions. Measurements with one and the same molecule allows us to track the influence of various parameters on the interaction between a single polymer and an interface independently from each other and to determine adhesion forces, surface binding energies and friction coefficients. In addition, due to its small size and the proximity to equilibrium this system can be treated with MD simulations. The latter allow extracting all different contributions to the adhesion free energy and provide a completely new insight into the interactions at the molecular level. Passivation of the tip surface avoids interference of the measurements by direct tip-substrate interactions or cavitation effects. These molecular sensors have been well characterized and statistical uncertainties for the results can be given.

Chapter 3

Hydrophobic Interactions at the Solid-Liquid Interface

The nanostructure of materials is supposed to affect polymer adhesion at the solid/liquid interface by variations of the exposed surface area. In contrast, our studies on the adhesion of single spider silk proteins onto smooth and rough steel surfaces show no effect of the surface morphology. This is explained by the negligible friction and the high in-plane mobility discussed in the previous chapter. We delineate further properties that determine single molecule adhesion onto solid substrates in aqueous environment. Wettability as well as electrical properties of the substrate and the polymer are varied. In addition, we study the influence of the solvent composition, in particular the effect of ions, on the molecular adhesion at the solid-liquid interface. Surprisingly, the polymer and surface related properties account for only small changes in adhesion force, while dissolved ions show a much larger ion-specific (Hofmeister) effect. These results point at the energy of solvation as the most important contribution to adhesion for a wide variety of polymers and substrate materials.

Nanoscopic modifications of surface properties are state of the art in many fields, ranging from materials science, through medicine, to nutrition science. They aim at controlling the interaction of macromolecules at the solid/aqueous interface. Colloid stabilization, polymeric lubrication, adhesive bonding and drug release, to name but a few, make use of nano-structures and chemical modifications to design molecular adhesion properties. Understanding how to prevent or enhance the adhesion of proteins and other biopolymers onto surfaces under physiological conditions is fundamental for the engineering of biocompatible medical devices and anti-infective implants [4,5,8]. A prominent approach to improve biocompatibility involves introducing surface functional groups by chemical treatments modifying polymer affinity [17,187,188]. In addition, surface geometry, polarity and wettability are known to play an important role in polymer adhesion [6,16,121].

Up to now studies on the influence of surface structure on polymer, cell or bacteria adhesion have focused on the number of cells or organisms[189,190], the mass and conformation of polypeptides[191,192] and the interactions of polymer layers with a solid substrate.[121-124] The adsorption and desorption kinetics under force for different surface morphologies have not to our knowledge been systematically addressed at the single molecule level. Common techniques for measuring adhesion properties comprise surface plasmon resonance (SPR) [193], total internal reflection fluorescence (TIRF) [194], ellipsometry [195], neutron reflectometry [196] and radio labeling [197]. These bulk studies scrutinize the amount of proteins adsorbed at the surface for example in dependence on the surface charge [193,195], the ion exchange capacity and the protein isoelectrical point [198] as well as the effect of surface chemistry [196-200] and roughness [191,201,202]. Based on experiments such as tensiometry and goniometry and SPR with polymer solutions other authors previously emphasized the role of solvent in adhesion phenomena [198-200]. Here we determine complementary parameters, namely the adhesion force and the adhesion free energy of individual polymers. There is a wealth of data obtained with AFM, where the cantilever tip is coated with polymers to measure the adhesion forces from solid substrates [121-123]. Such experiments yield interaction forces, but not free energies related to the thermodynamic adsorption equilibrium. Moreover, the number of interacting polymers is generally not known in such experiments. SMFS has been used previously to determine the influence of surfactants [203], charge contributions [132,134,137], and polymer design [130,138,204] on the adhesion strength. The results point to a considerable contribution of the non-electrostatic interactions of hydrophobic origin to these adhesion phenomena.

3.1 Effect of surface roughness

To elucidate the influence of the surface structure on polymer-surface interactions, we performed SMFS on a single eADF-4 molecule in aqueous PBS solution (Dulbecco’s phosphate buffered saline) at 36.5°C, and determined its adsorption free energy on polished and microporous steel surfaces. Stainless steel is one of the most prevalent implantable materials, in particular in cardiologic and orthopedic interventions [205]. Microporous steel surfaces, like those investigated here, are a promising approach for controlled drug deposition and retarded drug release [206].

Figure 3.1.1 (A) and (F) show electron micrographs of polished and microporous surgical stainless steel 316L, respectively, at 1200x magnification. Polishing of the steel blanks resulted in smooth and homogeneous surfaces with no greater cavities. Some pits that appear as darker spots surrounded by brighter rings are similar in size to the particles of the polish, and can be attributed to abrasion. Because in the AFM experiments the approach of the cantilever to the sample surface was monitored by optical microscopy of comparable magnification, those pits were avoided in SMFS experiments. In contrast to polished 316L, the microporous surface exhibits sharp edges and pore-like structures uniformly distributed over the whole surface. The topography on smaller scales was obtained with an AFM on the same samples used for SMFS, and confirmed the considerable differences in topography for the investigated specimens (figure 3.1.1 (B), (G)). The values of the root mean square (RMS) roughness, $R_{q,}$ were determined from 50 µm x 50 µm sized AFM height images. For polished and microporous steel, R_q was 13 nm and 494 nm, respectively. Cross-section profiles of the two steel surfaces at the micrometer scale are depicted in figure 3.1.1 (C) and (H), and at the nanoscale in figure 3.1.1 (D) and (I). They illustrate that the difference in roughness continues on the molecular length scale (of the order of the Kuhn length of the polymer) that is supposed to affect the interaction of biopolymers with the surface due to an increased effective surface area and surface tension, respectively.[202]

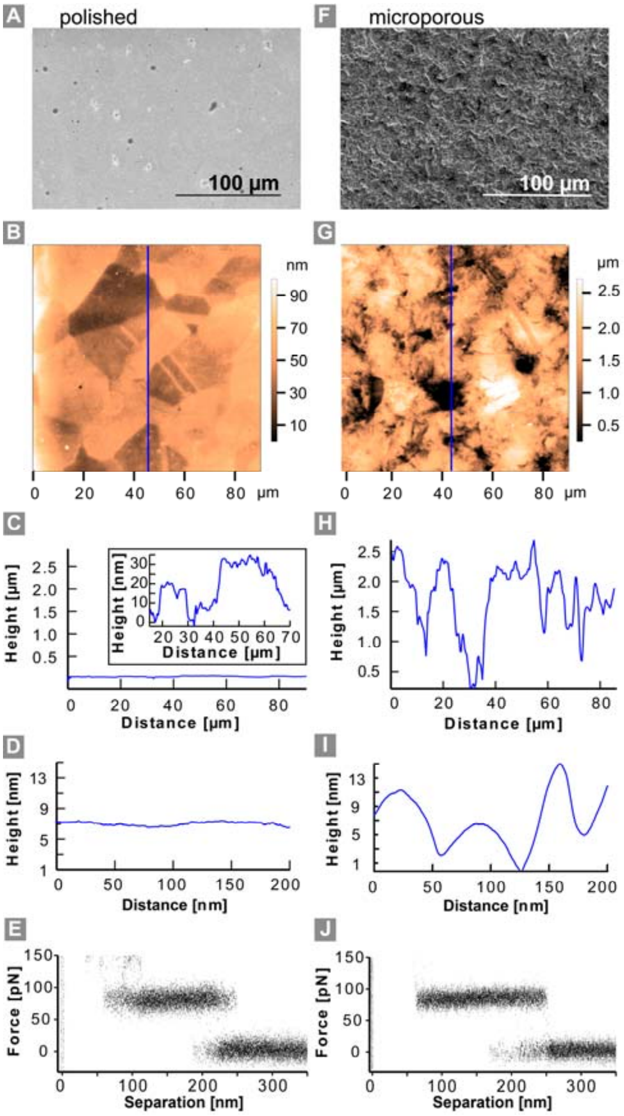

Figure 3.1.1: SEM (A) and AFM images (B) of a polished surface of surgical stainless steel blanks. The corresponding profile for a 50 X 50 µm² area image (B) is depicted in (C) and for a detailed scan of 200 x 200 nm² in (D). The inset in (C) shows a zoom into the height scale. (E) Superposition of 20 force plateaus of eADF-4 on polished steel. The corresponding images for a microporous stainless steel surface are illustrated in (F) – (J).

To separate the contribution of surface morphology from that of surface chemistry, we confirmed the identical surface composition of polished and microporous 316L by energy-dispersive X-ray (EDX) spectroscopy. Besides a small fraction of alumina and oxygen which originates from the use of Al_2O_3 as sandblasting material, the chemical composition was identical to the polished specimen (figure 3.1.2).

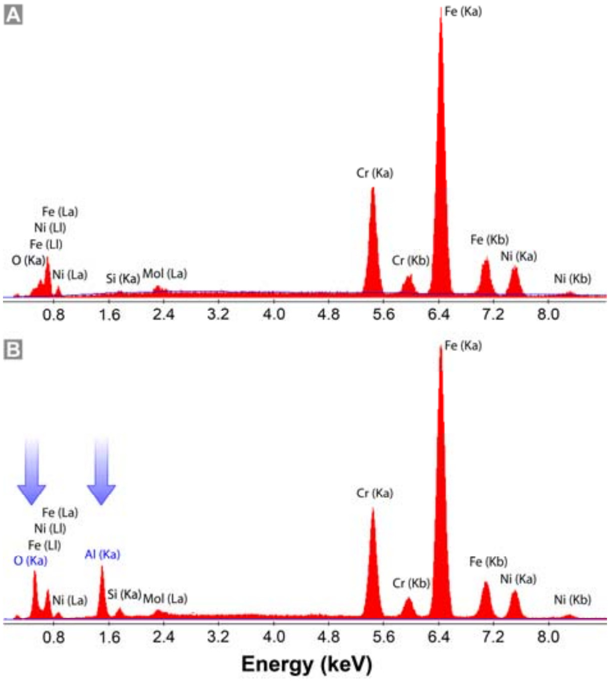

Figure 3.1.2: EDX analysis of surgical stainless steel after surface treatments. (A) spectra of polished and (B) sandblasted steel samples. The blue arrows indicate the changes upon surface treatment.

The binding of the polymer to metal is expected to occur mainly via hydrogen bonds. These bonds have a typical strength of several k_BT, and a typical time scale for bond breaking that is low enough to allow for equilibrium conditions to be achieved in the single-molecule experiment. Pinning points with higher adhesion strength and much slower dynamics would be necessary to observe friction effects at the single-molecule level. As we do not observe friction effects on surfaces of either roughness, we can conclude that a boss or a dip in the surface does not create spots, where increased hydrogen bonding can strongly bind an amino acid of the protein and thus increase the adsorption force.

From a macroscopic point of view, an increase in the effective surface area by increasing the surface roughness is supposed to enhance adhesion in different ways. For example, the mechanical anchoring via surface voids and pores is often associated with a stabilization caused by polymer entanglement.[207] Entanglement, mechanical and diffusive adhesion describe interactions in a polymer film and do not apply to an isolated molecule. Here, we probe the influence of surface structure on the dispersive adhesion of a single polymer. The seemingly counterintuitive result points to a molecular adhesion mechanism with negligible topographic and friction effects on interactions at the molecular scale. The reported influence of surface structure on cell adhesion or on the adherence of an applied coating might therefore be related to cell morphology, to the mechanical interlock of the adhesive material that fills the voids or pores of the surface, to the stabilization by polymer entanglement or to the occurrence of specific bonds, but, as we have shown here, not to single polymer-substrate interactions.

3.2 Impact of substrate hydrophobicity (wettability) on molecular adhesion

In order to achieve a continuously tunable wettability while keeping the element composition as constant as possible, we varied the composition of self-assembled monolayers (SAM) of alkanethiol with different end groups [208,209], namely OH and CH_3 (see Materials and Methods section for details). The surface hydrophobicity increased with increasing CH_3-termination and resulted in higher contact angles.

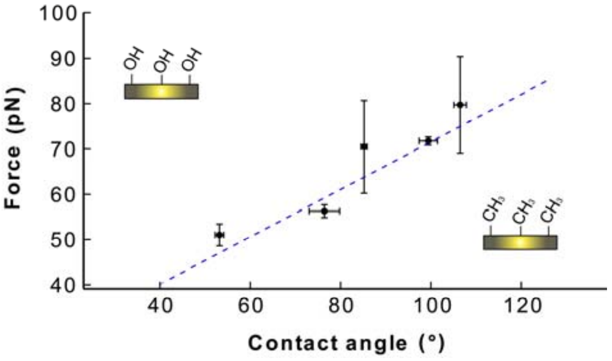

Figure 3.2.1: Influence of substrate wettability on adhesion forces. Desorption forces of PAAm on alkanethiol SAMs of different hydrophobicity in NaCl solution (for the size of the error bars see 2.7). The amount of CH_3 groups is increased from the left to the right and results in an increase in contact angle.

As molecular sensor we apply poly(allylamine) (PAAm) [210,211] PAAm is widely used as gene carrier and phosphate binding agent in pharmaceutical therapy [212,213]. Moreover it effectively immobilizes cells [214,215]. In contrast to the slightly negatively charged and mildly hydrophobic eADF-4, PAAm is hydrophilic and positively charged. Both polymers have similar molecular weights around 50 kDa (see Materials and Methods section for details). Figure 3.2.1 shows the desorption forces of PAAm in dependence on the contact angles given by an increased CH_3-termination. The desorption force increases monotonically with rising contact angle. The energy cost (per monomer) can be estimated from the slope to $0.031 \pm 0.003\ k_BT/°$ - assuming a linear dependence.

3.3 Influence of substrate electronic properties on single polymer adhesion

In the following, we also vary the composition of surface, polymer and solvent in order to achieve significant changes of adhesion forces and free energies, respectively. We thereby focus on hydrophobicity and electrical properties. Apart from conductive polished stainless steel (316L) and insulating poly(tetrafluorethylene) (PTFE), we investigate polycrystalline diamond, which is chemically modified to adjust its conductivity [216,217]. Oxidized diamond is isolating while hydrogenated diamond exhibits p-type conductivity [218,219].

In figure 3.3.1 four substrates with highly different electrical properties and wettability are investigated (different colors of the bars). The contact angles are given in table 3.3.1 and the electrical properties range from isolating (PTFE, O-diamond) to semi-conductive (H-diamond) to conductive (stainless steel). The successful modification of the diamond material by oxidation and hydrogenation was confirmed using Kelvin probe microscopy (KPFM) [220] on a patterned surface with both terminations (see section 4.2). All substrates in figure 3.3.1 (A) are probed with one and the same AFM-tip and sensor molecule, respectively. First, we applied the same polymer (PAAm) as in the previous section. The observed changes in adhesion force are resolvable within the resolution limit of our measurement. It is the chemical modification of the diamond material resulting in different conductivity, wettability and surface potential, which in particular leads to detectable changes in adsorption forces. Surprisingly, however, the forces and adsorption free energies do not differ by more than 6 % (table 3.3.1). The difference between the insulating and highly hydrophobic PTFE and the conductive and hydrophilic steel is a little larger, but also less than 15%. Therefore, in case of single PAAm molecules in water the adhesion is hardly influenced by the investigated surface properties.

Regardless of the considerable differences of the substrate materials and the polymers used, the observed changes are unexpectedly small. The variable composition of PTFE, steel, H- and O-terminated diamond, as well as the resulting difference of electronic and wetting properties, do not manifest themselves in different desorption free energies. Even the different termination of diamond, which leads to a pronounced variation in the surface potential, results in only a tiny change in the desorption free energy of no more than 1 k_BT per monomer.

Table 3.3.1: Adsorption free energies and static water contact angle of PAAm recorded in PBS at 36.5 °C for different substrate materials.

Substrate	Adsorption free energy [k_BT]	Contact angle [°]
O-terminated diamond	7.7±0.1	47±5
H-terminated diamond	7.3±0.1	53±3
Polished steel 316L	7.8±0.3	76±3
PTFE	7.9±0.2	130±9

Only in the case of SAMs does the systematical alteration of surface hydrophobicity upon the replacement of OH groups by CH_3 groups (all other properties being equal) lead to a little stronger effect on the adhesion strength (figure 3.2.1).

What could be the reason for the surprisingly weak – and sometimes even absent – influence of surface properties such as conductivity, wettability and surface potential on single polymer adhesion? One possible explanation is that the higher surface energy of a more polar surface (which facilitates the wetting of the surface formerly occupied by the adsorbed molecule and favors desorption), simultaneously leads to an increased dispersive interaction between surface and polymer (which hampers desorption). These two contributions (solvation and dispersion) could in part compensate each other, making the energy of solvation a decisive quantity.

This argument is underlined by previous studies on the non-uniform increase of the plateau height with the number of adsorbed carboxymethycellulose molecules [221]. In brief, these authors explain that the polymer-water interface is increased as the chain is pulled monomer by monomer out of the polymer film. For the case of separated molecules, the plateau height would simply be the plateau height for a single molecule times the number of molecules that are desorbed at a time and would result in a discrete distribution of equal step heights. Instead, a significant lower step height is observed for the second simultaneous desorption event, further decreasing with the number of additional plateaus. The force increment with the number of molecules could be explained by a simple geometric model based on polymer bundle formation upon H-bonding. The packaging minimizes the surface area of the molecules which is exposed to the solvent. The good agreement of this model with the experimental data suggested solvation forces to be dominating.

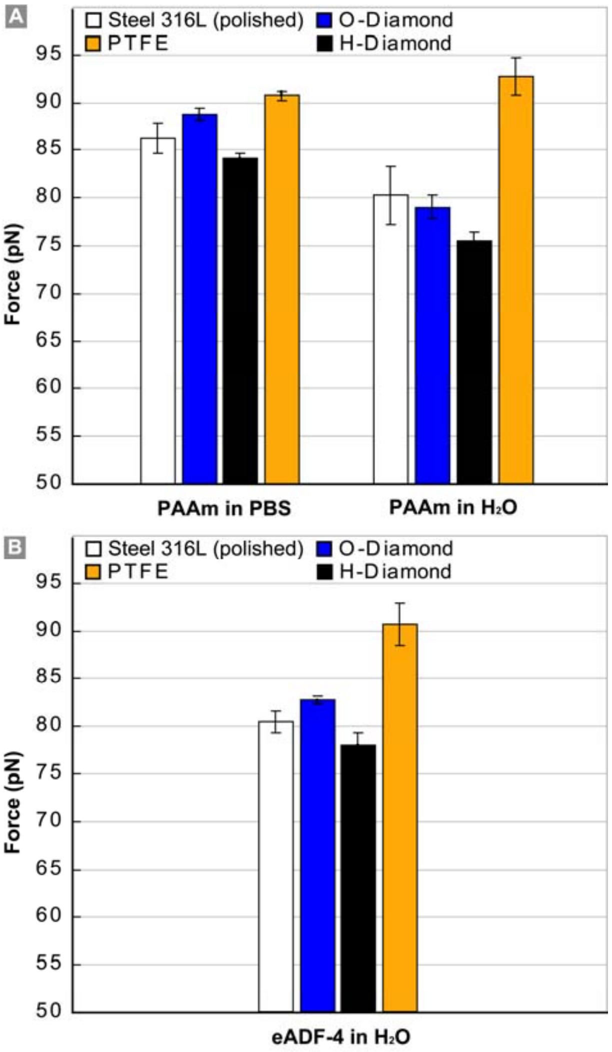

Figure 3.3.1: (A) Desorption forces in H_2O for PAAm on surfaces varying in their conductivity, wettability and surface potential. (B) The same experiment as in (A) for eADF-4 to indicate the effect of polymer composition on the desorption forces. (C) Measurements in PBS delineate the influence of ions on the desorption forces obtained with PAAm (compare to (A)).

Finally, we speculate that for many systems in aqueous environment (like the ones investigated here), the adsorbed amount of polymer as well as the adhesion of coatings is only marginally determined by the adsorption strength of a single polymer, but much more by cohesion effects. As described earlier, previous SMFS studies showed that the adsorption strength of polymers roughly is proportional to the number of chains which are desorbed in parallel [128,221,222]. Hence, the cohesion of a couple of polymers, which have to be desorbed in parallel, will already increase the adhesion strength significantly.

3.4 Contribution of polymer composition to single molecule adhesion

As surface properties played only a minor role in single polymer adhesion for the positively charged and hydrophilic PAAm, we used mildly hydrophobic eADF-4 bearing only a few negative charges to test the same substrate materials again for their polymer affinity. The results are depicted in Figure 3.3.1 (B). Within the uncertainties of our measurement, the forces needed to desorb the polymers from the surfaces in water are the same for PAAm (A) and eADF-4 (B). As the highly unequal polymers PAAm and eADF-4 did not show any differences despite a force resolution of about 3 pN (i.e. less than 4 % of the measured total values), we argue that both the investigated substrate properties (conductivity, wettability, surface potential) as well as the polymer properties (hydrophobicity, charge) play only an ancillary role in the equilibrium desorption process in aqueous environment (at least as long as the polymers are highly mobile in the plane of the substrate, i.e. as long as we observe plateaus of constant force).

3.5 Effect of ions on single polymer adhesion – The Hofmeister effect

Finally, we tried to provoke a significant change in single polymer adhesion by adding salts to the solvent. Instead of using pure water, we measured in isotonic PBS solution with Mg^{2+} and Ca^{2+}, which contains 142 mM chloride salts and 10 mM phosphate salts. As in the previous section, we measured with PAAm on steel, PTFE, H-terminated and O-terminated diamond. Figure 3.3.1 (C) shows an increase of about 10% (compared to (A) and (B)) on all but the PTFE substrate. This represents a large change in force and desorption free energy compared to the variation of the parameters discussed above namely the composition of the substrate or the polymer. Note that for PTFE the desorption force remains unaffected.

This noteworthy effect of around 10% due to the presence of ions in the solvent points to either an electrostatic (screening) or solvation effect. The amine groups of the polycation PAAm are partially protonated (about 80% of the monomers) and therefore positively charged at physiological pH [132]. The spider silk motif C16 of eADF-4 exhibits only 16 amino acid residues that can dissociate in aqueous environment and become negatively charged. In the following we provide two arguments as to why electrostatics does not explain our observations. Firstly, the different surfaces are affected by ion adsorption at the solid/electrolyte interface in different ways. Metal oxides, for example, have a strong affinity for cations from solution. Hydrogenated diamond, on the other hand, preferentially binds anions to its surface [218].

In our experiments, however, we observe the same trend upon the addition of salt for both surfaces. Secondly, the measurement on the mildly negatively charged spider silk eADF-4 should reverse the effect compared to the positively charged PAAm in the case of pure electrostatic interaction. Again, this is in clear contrast to the experimental observations. The same increase of comparable magnitude is measured for both polymers. Accordingly, another mechanism is needed to account for the higher forces in the presence of ions. The ions in the PBS buffer can have a stabilizing effect on the water structure and therefore act as kosmotropic Hofmeister salts. It is noteworthy that kosmotropic co-solvents which are excluded from the protein surface and cause proteins to favorably interact, to assemble and finally to salt-out, can render surfaces highly protein-resistant if immobilized on that surface [223]. In addition, this effect is closely linked to the hydrophobic effect, which together with the presence of salt, accounted for the most pronounced effect on single polymer adhesion in the present case. However, this salt dependent effect is absent on PTFE for both eADF-4 and PAAm – one reason could be the fluorophobic properties of PTFE which might lead to a negligible ion interaction, and therefore an undisturbed water structure [224].

Figure 3.5.1 illustrates the effect of salt concentrations. The desorption force stays constant at concentrations of up to 1M before the forces increase non-monotonically. The increase is different for different salts, kosmotropic phosphate has a stronger effect compared to chloride salt.

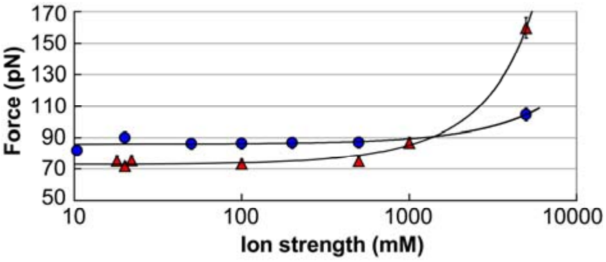

Figure 3.5.1: Increase of the desorption force of eADF-4 on H-diamond with salt concentration. The slope is non-monotonic and is more pronounced at concentrations above 500mM. The force increment is larger for the more kosmotropic phosphate salt compared to chloride. Data points are obtained with one and the same cantilever.

Next we compared the effect of different salts on the desorption force. We chose ionic strengths of 0.5 M and 5 M because the salt effect increases with salt concentration. All possible charge effects are screened and the salts are still not precipitating at these concentrations.

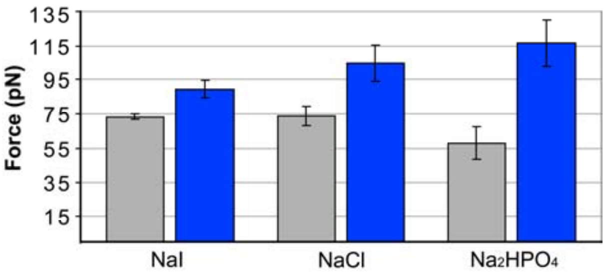

Figure 3.5.2: The desorption force of eADF-4 on diamond in sodium salt solutions. At a concentration of 0.5 M there is no measurable influence of the ions (grey bars), whereas a clear impact of the anions becomes visible at 5 M (orange bars). The trend follows the Hofmeister series.

The comparison of the forces acting at different salt concentrations of our solutes demonstrates that Hofmeister effects are either not present or very weak at medium salt concentration, but are very strong in the high salt regime (figures 3.5.1 and 3.5.2). As expected, the strong kosmotrope phosphate considerably increases the desorption force, while the less kosmotropic chloride has a still more stabilizing effect than iodide. Figure 3.5.3 depicts the Hofmeister series for anions, measured by desorption of spider silk protein eADF-4 from H-diamond at high ionic strength. It is noteworthy that we also observe an effect from the exchange of the cation: potassium seems to have a more stabilizing effect on the hydrophobic attraction of the protein with the surface than sodium. This effect is in agreement with the stabilizing power of anions and cations in salting out proteins as given by hundreds of publications (see ref. [52] and references therein), here from ref. [56]: $CO_3^{2-} > SO_4^{2-} > H_2PO_4^- > F^- > Cl^- > Br^- > NO_3^- > I^- > ClO_4^- > SCN^-$.

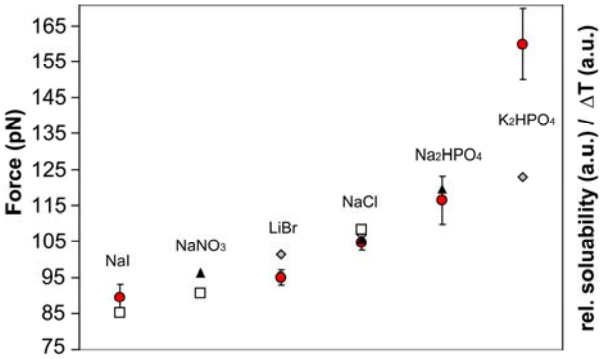

Figure 3.5.3: Anionic Hofmeister series for desorption of eADF-4 from H-diamond and comparison of single molecule desorption and bulk experiments. The salt concentration is 5M. Desorption forces (circles) for eADF-4 from H-terminated diamond, change in ProtL mid-denaturing temperatures, ΔT, upon addition of 0.8 M salt (triangles) [62] and relative solubility of benzene in 1 M salt (squares) [73].

The average adsorption free energy per amino acid at 5M is abaut 8 k_BT, 9 k_BT and 10 k_BT for NaI, NaCl and NaH_2PO_4, respectively (k_BT = 4.2 pN·nm at a temperature of 300K). The stabilizing energy (the additional adsorption free energy upon the addition of salt) for the 5 M phosphate buffer is even as high as 14 k_BT per amino acid. This energy gain is compared to typical equilibrium energies for protein folding [225] and huge in comparison to the unzipping of coiled coils with an energy of about 0.5 k_BT per amino acid[226]. In contrast, the water-water interaction has an energy of up to 10 k_BT at room temperature[75].

Typical concentrations of salts used to drive many biochemical laboratory processes are in the molar range. For example, 2 M $(NH_4)_2SO_4$ (~ 50% saturated) is a typical concentration to precipitate proteins and 3 M guanidine chloride (GdmCl) is a typical protein denaturing solution [227]. We state that these concentrations are substantially higher than under most physiological conditions. The total ionic strength of physiological serum is about 0.15 mol l^{-1}, however the ionic strength in ion channels can be of several mol l^{-1} [60].

We checked this series on a second engineered spider silk eADF-3 ($(QAQ)_8NR3$), revealing a similar general trend [228] (figure 3.5.4). What is the effect of the polymer's hydrophobicity on the desorption force? The protein eADF-3 is less hydrophobic than eADF-4 [177,229], namely -0.92 for C_{16} and -0.46 for $(QAQ)_8NR3$ (calculated after Kyte et al.[230]), and is supposed to lead to a stronger adhesion. We therefore expect a higher desorption force for eADF-4 on a hydrophobic substrate (all charges should be screened). The stabilizing power of the Hofmeister ions however is comparable as shown in figure 3.5.4. Note that the measurements have been performed with different cantilever and an additional uncertainty of at least 13% has to be considered. This indicates again the minor role of the polymer composition for this kind of hydrophobic attraction of a single molecule on a surface (compare to section 3.4). These findings are in agreement with solubility studies where the Setchenow constants which describe the solubility of a solute in electrolyte solution in dependence of the ionic strength, are usually highly correlated with one another, even though they are derived from solubility studies of quite different solutes [166]. And consistent with this, the regression studies of Schumpe et al. invoke only an additive constant to account for differences in solutes [231]. Our result indicate once more that the identity of the solute is of secondary importance in determining their sensitivity to the presence of salts.

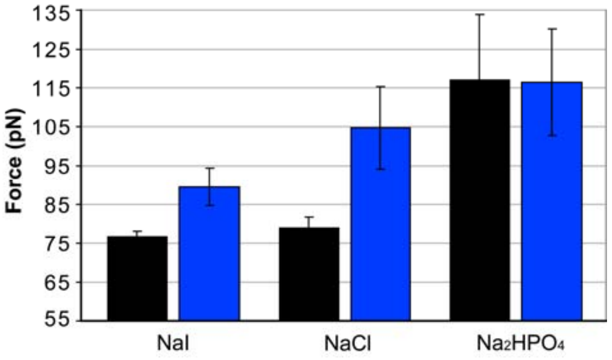

Figure 3.5.4: Effect of polymer hydrophobicity on Hofmeister effect. Desorption forces of hydrophobic eADF-4 on diamond in the electrolyte solutions (blue) are shown together with desorption forces of the less hydrophobic eADF-3 (black).

In figure 3.5.3 we compare our results with studies on the effect of Hofmeister ions on protein solubility[73] and protein denaturation[62] corresponding to observations made in solution. As mentioned before, the general trend at high salt concentration is the same. However, the absolute values demonstrate that the stabilizing effect is much more pronounced in the bulk experiments. This might be due to the extremely low concentration of proteins in our experiment, (in general an isolated molecule at the cantilever tip), which would mean that salting out or denaturation would be a very cooperative effect (comparable to the critical micelle concentration of lipids in water[232]). Another reason might be the regulation of water structural, dispersive and cosolute forces at the surface that has been discussed already in section 3.3.

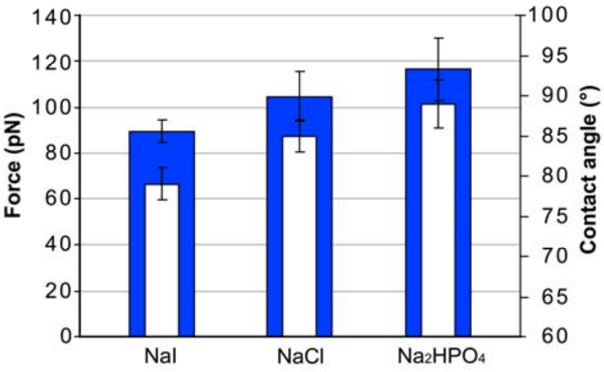

Figure 3.5.5: Comparison of desorption forces of eADF-4 on hydrophobic diamond in aqueous salt solutions and the respective contact angles.

Finally, we compare the desorption forces obtained on hydrophobic diamond for different salts at high ionic strength with the respective contact angles representing surface tension. As one can see from figure 3.5.5, the trend is almost the same for static contact angles and desorption forces measured on the same surfaces. This similarity corroborates previous observations of a close relation between hydrophobic effects and surface tension measurements [81,101].

3.6 Influence of solvent pH

In order to elucidate the role of the pH of the aqueous media for the polymer-surface interaction and to ensure that the observed changes in adhesion force in case of different salt solutions are not just the result of a change of the dissociation of chemical group accompanying a change in pH, we varied the pH by changing the salt solution of moderate ionic strength (500 mM). Note that not only the pH of the buffer solution is changed, but also the size, polarity and valency of the anion (figure 3.5.1). But at these concentrations electrostatic interactions are screened and ion-specific effects are minor (cf. section 3.5).

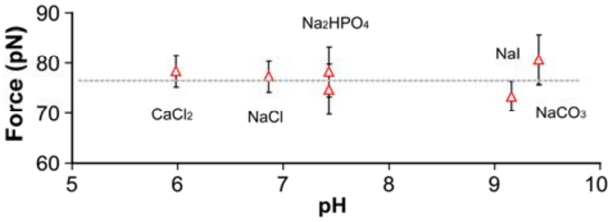

Figure 3.6.1: Desorption force independence from solution pH. The forces remain constant throughout the pH range covered by different salts at 500 mM concentration.

We can exclude any considerable influence of the solvent pH on the hydrophobic attraction of the polymers. The electrostatic forces due to the effect of pH on the line charge density of the polymer i.e. a different degree of dissociation of side groups, results in no measurable effect, as could be expected from the small number of possible charges of the proteins investigated here. The influence of pH only becomes relevant in case of highly charged polymers (polyelectrolytes) on charged surfaces [115].

3.7 Concluding remarks

Our AFM-based single molecule approach similar to a “nano-peel test” demonstrates negligible friction effects on the adhesion of single polymers on surgical stainless steel independent of the nano-scale roughness. This “sliding adhesion” manifests itself in similar adsorption free energies per molecule regardless of the surface roughness. The experiments clearly show an equilibrium situation, despite the formation of hydrogen bonds between polymer and surface. Moreover, we used the single molecule sensors to determine single polymer adhesion in terms of their adsorption free energies onto various substrate materials. Surprisingly, most material properties like roughness, conductivity, surface potential and even composition hardly influence single molecule adhesion under equilibrium conditions. Directly solvent-related properties, such as wettability and ion concentration have a much greater effect, but still less than 50%. The reason for the very similar adhesion forces might be a compensation of solvent-surface interactions and dispersive forces between polymer and surface. Our findings demonstrate that chemical modifications are in fact capable of fine-tuning the surface adhesion of polymers, but as long as the polymers are mobile in the plane of the substrate (which has always been the case for the wide variety of substrates investigated here), these effects are marginal.

We could clearly identify an ion-specific dependence of the desorption forces. Are the presented results just a new manifestation of the Hofmeister effect? In principle yes, but this system offers a completely new quality of data which can not be obtained by any other method: i) The small size of the system allows a direct comparison with MD-simulations (cf. 1.3 and 2.4), ii) the quasi infinite dilution of polymer allows to access the whole soluble concentration range for ions, iii) distributions of physical values are obtained, different populations are therefore not hidden in average values, iv) the effect of salt and polymer hydrophobicity can be investigated separately. For these reasons such experiments are expected to lead to a better understanding of Hofmeister and hydrophobic effects. Of course, more measurements at many different salt concentrations and with various ions and polymers are necessary to put existing theoretical models to test and to allow for new (unified) descriptions.

Chapter 4

Aging of Hydrophobic and Hydrophilic Diamond

In the following, dynamic force spectroscopy with a single polymer sensor demonstrates that hydrogenation and oxidation of polycrystalline diamond effectively control molecular adhesion in terms of adsorption free energies. We find that aging considerably changes these properties and originates from the rapid formation of a thin (< 2 nm), extremely resistant contamination layer as well as degradation of the artificial surface termination on longer time scales. This aging also affects the wettability, morphology and the electrical properties of the surfaces.

As the size of devices diminishes to the nano-scale, effective control of their surface properties becomes more and more important to ensure their prolonged performance. At the nano-scale interfacial properties can differ from the macroscopic properties including conductivity, electron affinity, surface potential and reactivity [233]. Here we use our single molecule sensors to study molecular adsorption free energies in liquid under variable conditions over longer periods of time. The nano-scale precision and the excellent sensitivity to surface properties already exemplified in the previous chapter are demonstrated by the investigation of the aging of diamond, which was chemically modified to control its conductivity, surface potential and wettability.

Diamond exhibits extraordinary mechanical properties and is chemically inert as well as biocompatible. It is therefore suitable for biomedical applications [216,234] as cell growth support [217,235] and as refinement of medical indwelling devices [236,237]. In addition to the exceptional material characteristics, hydrogenated diamond exhibits p-type surface conductivity, whereas oxidized diamond is insulating [219]. These electronic properties have advanced the further development of diamond-based sensor devices, such as electrochemical sensors [238], biosensors [239,240] and ion-sensitive field effect transistors (ISFET) in bioelectronics [218,241,242]. The application of diamond-based devices that take advantage of diamond's unique surface properties, be it in air, in aqueous solution or even in blood, necessitates stable surface conditions and interfacial properties in order to ensure the long lasting functionality of the device. It has just been the limited chemical stability under physiological conditions that has hampered the implementation of silicon and other semiconductive material in similar devices. Implanted medical devices should stay intact for months or even years without the need for removal due to restricted biocompatibility and foreign body reactions.

4.1 Alteration of adhesion properties of PAAm onto diamond over time

We utilize SMFS in order to determine the adsorption free energy of PAAm on diamond surfaces of different termination and different age (figure 4.1.1 (A)).

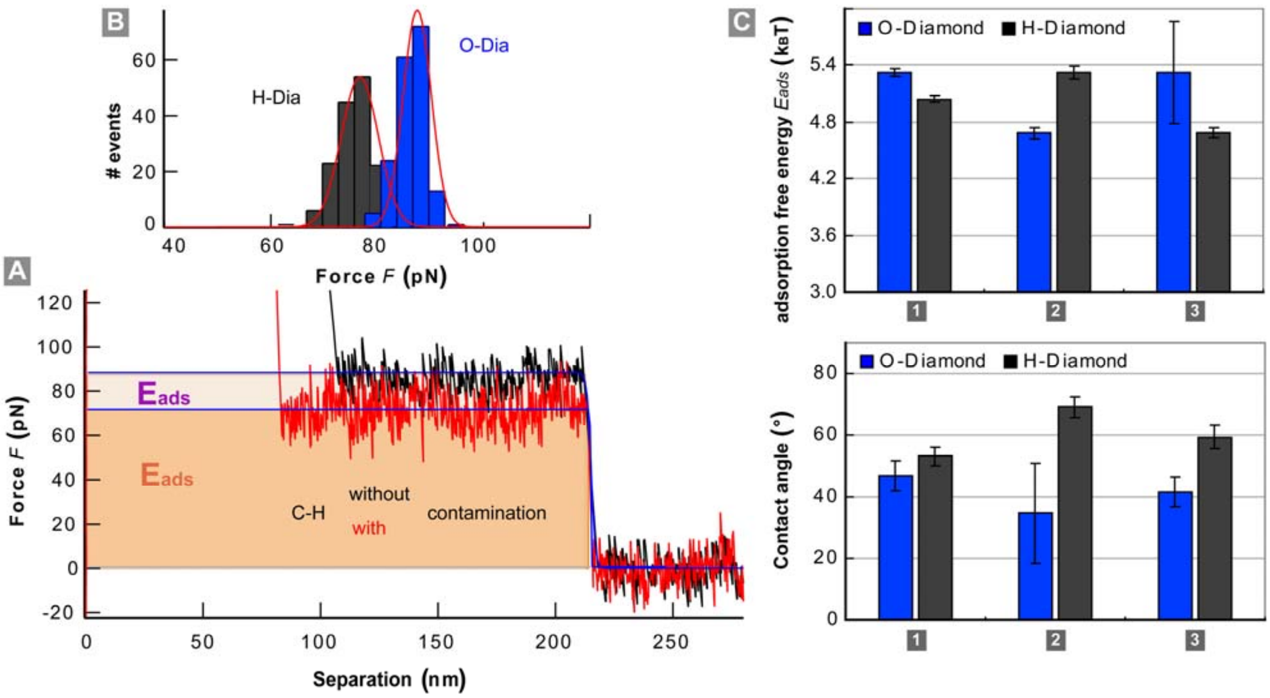

Figure 4.1.1: Consistency of adsorption free energy and contact angle alterations over time. (A) Typical force-separation traces recorded on freshly hydrogenated diamond (black) and on a contamination layer on the same surface (red). The desorption force was determined by the step height of sigmoidal fit-function to the force-separation trace (blue line). (B) The force distributions for PAAm on H-terminated (black) and O-terminated diamond (blue) are Gaussian and sharply peaked. These distributions point at a uniform contamination coverage of the surface. (C) Adsorption free energies per monomer from SMFS (top) and contact angles (bottom) for PAAm on H-terminated (black) and O-terminated diamond (blue) on the same surface (1) half a year old, (2) cleaned, with renewed termination and (3) again 2 months later (cf. Figure 4.1.2 A). The forces on both surfaces were recorded with the same single polymer sensor.

The distribution of plateau forces for H- and O-terminated diamond are given in figure 4.1.1 (B)).[ii] The general observed trend of measuring higher adsorption forces and therefore free energies on freshly prepared, hydrophobic diamond compared to hydrophilic diamond is even reversed after two months and can be restored after new termination. These adsorption free energies per monomer on both kinds of terminations mirror the change of the contact angle, thus wettability (figure 4.1.1 (C)). Moreover, there is a relation between the adsorption free energies and the surface energy of diamond as revealed by contact angle measurements with varying reference liquids on the same surfaces of different termination and age (table 4.1.1). Higher surface energies correspond to lower adsorption free energies.

[ii] Cluster formation of adsorbates on the surface can be excluded because we do neither observe an inhomogeneous coverage of the surface in the AFM images nor a broadening of the force distributions or the existence of two or more peaks in our force histograms (Figure 1C). On the contrary, the recorded force histograms are always sharp, only the mean value is shifted. For that reason we assume a uniform distribution of contaminants on the C-H and C-O surface.

Table 4.1.1: Adsorption free energies W per unit length for PAAm recorded in PBS at 36.5 °C with SMFS and surface energy γ_S on hydrogenated and oxidized diamond from contact angles: cleaned (2) and half year old (1) (compare to figure 1D)

Substrate	γ_S [mJ m^{-2}]	W [10^{-9} mJ m^{-1}]
O-term. diamond (2)	77.8±0.7	78.1±1.1
H-term. diamond (1)	54.9±1.2	84.1±0.6
H-term. diamond (2)	18.8±1.3	88.7±1.0

4.2 Change of diamond surface potential over time

Surface potential scans of the patterned C-H/C-O surface over a period of nearly one year corroborate our findings. For a new sample the surface topography of a square area of 50 µm scan size (figure 4.2.1 (A)) obtained by Kelvin probe force microscopy (KPFM) exhibits a mean roughness of less than 3 nm. The surface potential image of the same section of a new specimen reveals a regular pattern of dark (oxygen terminated, C-O) spots on a bright (hydrogen terminated, C-H) background (figure 4.2.1 (B)). Along the cross-section profile, the surface potential difference drops from 240 mV in the C-H region to about -50 mV in the C-O regions. This decrease in potential of 290 mV corresponds to a higher work function of the C-O surface compared to the C-H regions and is in good quantitative agreement with previous studies on single crystalline diamond [243]. The KPFM data clearly shows that we succeeded in generating a dense and uniform surface coverage with H- and O-atoms, respectively.

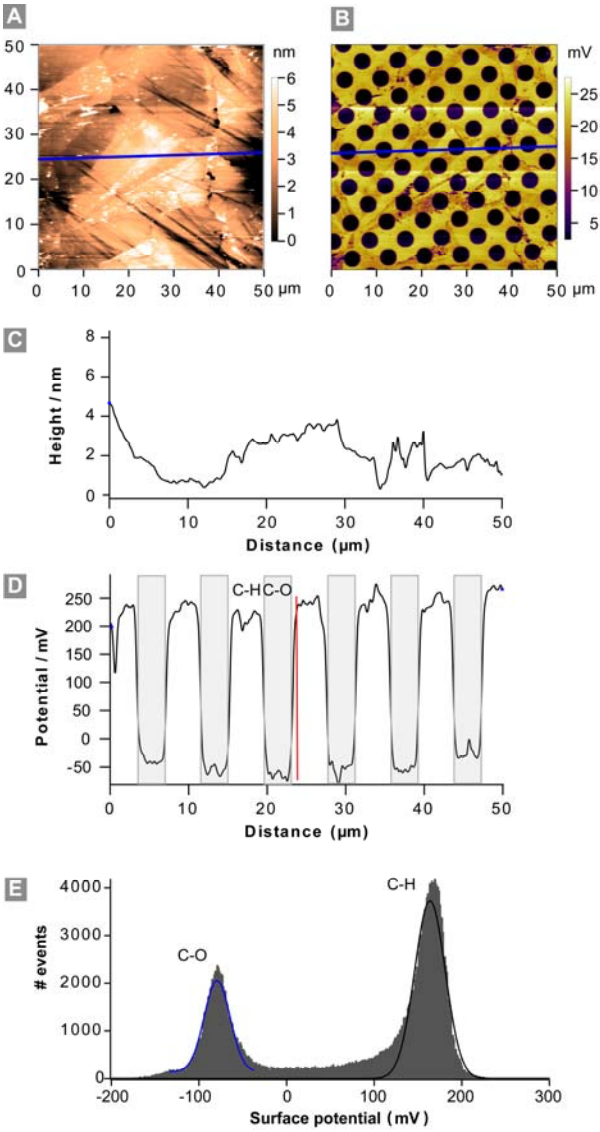

Figure 4.2.1: Oxidized and hydrogenated checker board diamond surface. Topography (A) and surface potential (B) of a polycrystalline diamond with oxygen (dark) and hydrogen (bright) termination obtained by KPFM. Pictures were taken two hours after processing. The corresponding cross sections (C) and (D) are recorded along the blue lines in (A) and (B). The white and grey areas in the potential profile mark the C-H and C-O regions, respectively. (E) Histogram of a KPFM surface potential image of a C-O/C-H patterned diamond sample. Two sharp peaks in the potential distribution indicate the uniformity of the surface termination.

It is noteworthy that the potential across the C-H/C-O boundary exhibits a pronounced slope over about 1.5 µm distance instead of a steep decay (indicated by a red vertical line in the potential profile in figure 4.2.1 (D)). This trace appearance is not the result of a limited lateral resolution of the KPFM measurement, since that can be estimated as 5z for z > 3 nm (here: z = 10nm) with z being the tip-surface separation [244]. Accordingly, our resolution is about 50 nm, which is an order of magnitude smaller than the measured decay length. Two possible explanations of such a potential decay across several micrometers from the material boundary are a stray capacitance of the cantilever [245] and a charge depletion region at the C-H/C-O interface [243].

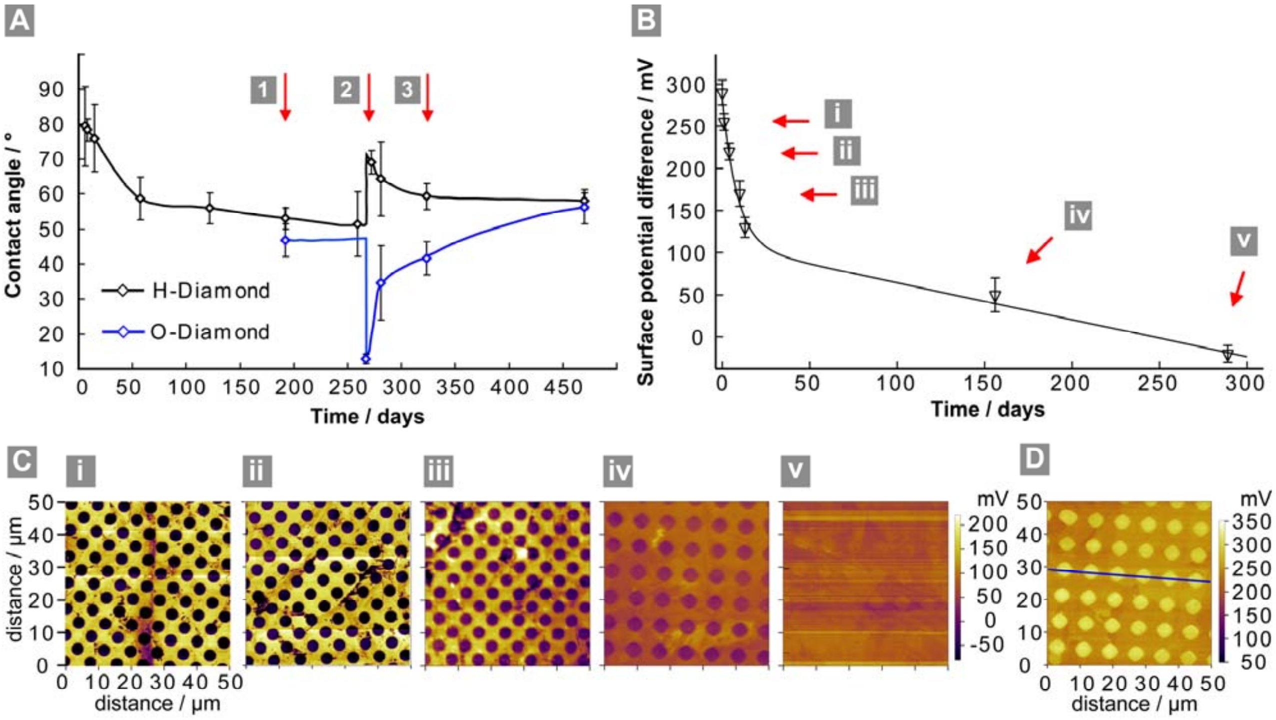

Figure 4.2.2: Time dependent change of contact angles and surface potential. (A) Static water contact angle on H-terminated (black) and O-terminated (blue) diamond over time. 260 days after the initial treatment of the surfaces, the termination was renewed. The red arrows indicate the points in time when SMFS was conducted on these surfaces. (B) Time dependent decay of the surface potential difference on C-H/C-O patterned diamond. (C) Surface potential images obtained using KPFM of a C-H/C-O surface over time (same color scale for all images (i)-(v)). (D) The same surface as in (C,v) after mechanical cleaning.

We analyzed the time dependent change of the measured static contact angle on hydrogenated (black) and oxidized (blue) diamond in more detail over a time period of several hundred days (figure 4.2.2 (A)). The aging effect on wettability for both diamond surfaces starts immediately after surface treatment and saturates after the first 50 days. Both surfaces were stored in vacuum[iii] except for the time span during the SMFS measurements that were performed in

---

[iii] Contamination by oil from the vacuum pump was excluded. Control experiments on samples stored under ambient conditions gave similar results, however we concede that the storage in vacuum might slow down the contamination process.

electrolyte solution. The hydrophobicity of the H-terminated surface decreased nearly exponentially during half a year. 260 days after the initial termination of the substrate, the termination was renewed, which resulted in a rise of the contact angle to almost the starting level followed by a similar exponential decay over time. This behavior is likewise observed for the O-terminated diamond but with the opposite sign. After half a year, they approach the same value although the contact angle initially differed by more than 70 °.

As depicted in Figure 4.2.2 (B), the decay of the surface potential difference between C-H and C-O regions over time is similar to that of the contact angles. The early surface potential difference of 290 mV is even inverted after 300 days of storage. Figure 4.2.2 (C) (i)-(v) illustrates the aging effect on the surface contact potential of both terminations. The sharp contrast of the dark C-O and the bright C-H regions is blurred with time. The final potential difference of -20 mV barely reproduces the surface pattern.

Considering the origin of this aging process likewise observed in SMFS and contact angle measurements, one can think of two possible mechanisms, which can act on both surfaces, namely i) contaminations that cover the surface (such a molecule-thin adsorbate layer was previously verified on hydrogenated diamond) [246] and ii) the conversion of the artificial surface termination which has been predicted theoretically [247,248].

4.3 Origins of the diamond aging process

Figure 4.3.1 (A) shows a typical tapping mode AFM image of an O-terminated diamond surface after 50 days. For all other images in figure 4.3.1, possible persistent pollutants that were still present on the diamond surface despite thorough ultrasonic cleaning were scraped off using contact mode AFM. One can clearly identify a height difference in the topography image by

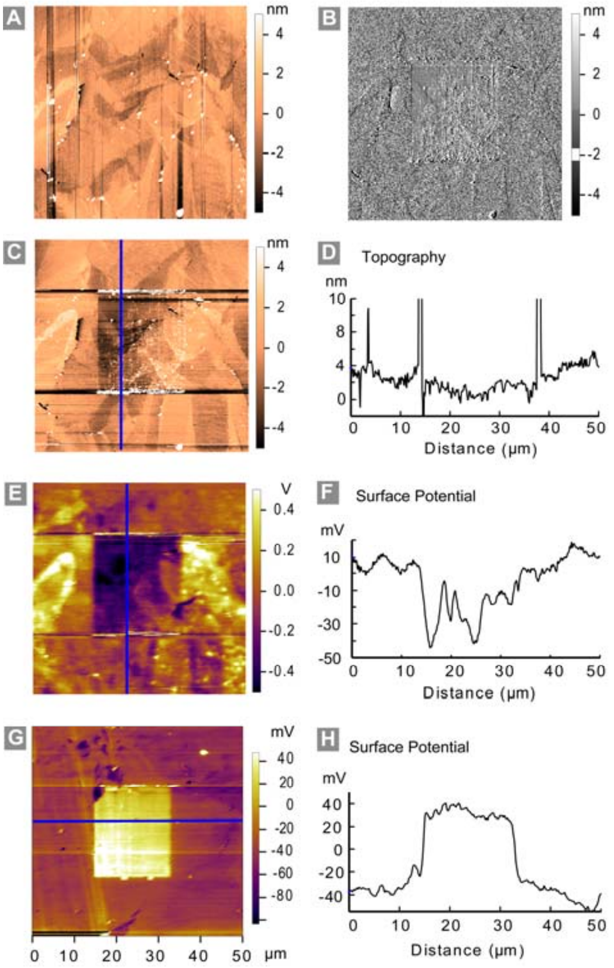

Figure 4.3.1: Contamination layer on H- and O-terminated diamond. (A) Intermittent contact-mode AFM height image of a 50 mm_50 mm surface area of O-terminated polycrystalline diamond. (B–F) The same surface area after scraping, using contact-mode scanning in the central square with maximal load. Images of the amplitude signal (B), topography (C), and the surface potential (E) are shown. Topography and surface potential cross-sections along the white lines are depicted in (D) and (F), respectively. A surface-potential image of an H-terminated diamond after scratching of a square area of 20-mm edge size is shown in (G) and the corresponding potential cross-section in (H).

observing the darker contrast compared to the surrounding area and two brighter bands indicating accumulated material on both sides of the scan lines (figure 4.3.1 (C), (D)). The height difference is between 1 nm and 2 nm. The amplitude image (figure 4.3.1 (B)) reveals a granular structure of the topmost surface layer while the exposed surface underneath is very smooth. Finally, the KPFM image (figure 4.3.1 (E), (F)) shows a uniform square of lower potential in the scratched area surrounded by a more inhomogeneous potential landscape. The surface potential difference between the covered and the cleaned surface area is about 40 mV. We utilized the same procedure on H-terminated diamond and found a mechanically removable thin layer with comparable characteristics as well. But in contrast to the O-terminated diamond, the surface potential image shows a higher surface potential of the exposed square area compared to the covered surface (figure 4.3.1 (G), (H)). Despite the different sign, the potential difference (70 mV) is of the same order of magnitude in both cases. Rezek and Nebel concluded that the thin layer of non-diamond material they observed after high temperature hydrogen plasma treatment was restricted to hydrogenated diamond and originated from a carbon deposit generated during the plasma cooling process [246]. In the light of our new experiments, it transpires that besides this possible contamination during processing, an additional contamination layer is continuously formed over time which likewise affects the hydrophobic C-H as well as the hydrophilic C-O surfaces. This layer is highly resistant to common chemical cleaning procedures in both cases. Mechanical cleaning on the other hand could cleanse the samples from at least most of the surface adsorbates and resulted in a visibly reversed surface potential of the nearly one year old patterned surfaces (figure 4.2.2 (D)). The surface potential difference of this cleaned sample (-70 mV after 300 days) is considerably different from the initial state (290 mV). Mechanical cleaning of 13-day old sample surfaces however, restored the surface potentials of C-H and C-O areas completely (data not shown). This inversion clearly proves that besides a contamination the artificial surface termination is also affected by thermodynamically driven conversion of surface functional groups.

To further investigate the nature of aging of the surface termination on diamond, we revisited the change of contact angle over time after eliminating most of the chemical resistant contamination layer through mechanical cleaning of the surface (figure 4.3.2). This allows for the separation of the influence of pollutants from that of the thermodynamically driven conversion of surface groups and thus for the time resolved observation of the surface stability. For two different diamond surfaces (A) and (B) terminated with hydrogen, contact angles were immediately measured after surface processing of 87±4 ° (A) and 78±2 ° (B). Despite ultrasonic cleaning, the contact angle decreased to 64±5 ° (A) after one month of storage and 65±2 ° (B) after eight months. After the contamination layer was removed using mechanical cleaning, the contact angle of the one-month old sample reversed to 80±2 ° (A), slightly below the initial value. Eight months after processing, the contact angle upon mechanical cleaning did not recover, but even further decrease to 49±2 ° (B). Also, in the case of the O-terminated specimen (C), the contact angle increased from 12±2 ° to 61±4 ° after eight months and then dropped to 41±2 ° after mechanical cleaning, far above the initial value.

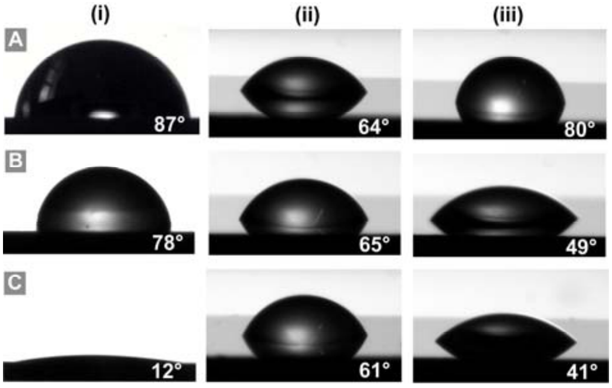

Figure 4.3.2: Effect of contamination and degradation on contact angles. Static water contact angles on H-terminated (A), (B) and O-terminated (C) diamond immediately after surface termination (i), several months after initial processing (ii), and finally mechanically cleaned to remove any contamination layer present on the surface (iii).

These results are consistent with the observed inversion of the surface potential and indicate a degradation of the artificially produced termination of diamond that is time dependent and affects C-H as well as C-O groups. However, in contrast to the formation of the surface-covering contamination layer that starts immediately after the processing of the surface modification, the conversion of surface groups takes longer to become effective.

4.4 Concluding remarks

In summary, we conclude that oxidation and hydrogenation of polycrystalline diamond surfaces effectively control molecular adhesion in terms of adsorption free energies. However this artificial termination exhibits aging that also affects the wettability, morphology and the electrical properties of the surfaces. Our long-term observations reveal the origin and the time scales of the aging process. We were able to identify two significant contributions to aging – the physisorption of atmospheric adsorbates on the time scale of days and conversion of surface chemical groups on the time scale of months. The differences in adsorption free energy per length, the surface potential differences and the surface energies at the respective points in time reveal a clear relation between these quantities.

Our single molecule sensor proved extraordinary sensitivity to changes of the surface conditions and is therefore a necessary complementary technique to contact angle measurements. The latter necessitates a rather flat, dry and clean surface area suitable for at least a 1 µl droplet. SMFS is not limited by these requirements but allows for the observation under physiological “real life” conditions on nanometer-sized structures.

Chapter 5

Hydrophobicity and the Concept of Entropy Convergence

Characterization of the hydration thermodynamics is among the major objectives when it comes to understand the stability of proteins in biological systems. To bridge the gap between the previously studied solvation of small non-polar model compounds and the hydrophobic attraction in protein folding we use our single molecule sensors to investigate the hydrophobic hydration thermodynamics of macromolecules. This method allows analyzing the influence of chain entropy on basic thermodynamic parameters. We find that the phenomena of entropy and enthalpy convergence inherently coupled to hydrophobic hydration on nanometer length scale is still observable in the case of polymers and that the characteristic convergence temperatures are shifted to the biological relevant regime. Solvent additives such as salts strongly affect the hydration thermodynamics and reveal a connection of the hydrophobic and the Hofmeister effect in terms of an ion specific shift of the particular convergence temperatures.

Despite many decades of research on hydrophobic attraction, our understanding of key phenomena of hydrophobic origin is still incomplete. Surprisingly, these include the effects of changing even the most elementary thermodynamic variables such as temperature or key solution properties, such as salt concentration and composition [249]. Following the convention of several previous authors [1,2,31,250], we define the hydrophobic effect in terms of the thermodynamics associated with the transfer of a molecule into aqueous environment.

One of the most astonishing observations associated with the hydrophobic effect is that the entropies of transfer of non-polar molecules from either the gas, liquid or solid phase into water converge at a common temperature [1,20]. Similar behavior was noticed in microcalorimetry experiments on unfolding of several globular proteins [59,251]. This analogy supported the hydrophobic core model of protein folding: during unfolding predominantly nonpolar residues are transferred from a mostly nonpolar protein core into water [252,253]. Although other interactions, such as electrostatic interactions and intramolecular (or water mediated) hydrogen bonding, cannot be neglected in a complete treatment of the thermodynamic stability of amphiphilic molecules such as proteins and their assemblies. Nevertheless, a predictive understanding of the stability of hydrated amphiphilic macromolecules necessitates a thorough quantitative description of hydrophobic driving forces as a major contributing factor [232,254].

Hydrophobic temperature signatures, namely entropy and enthalpy convergence are the prime target of studies of hydrophobic phenomena [1]. The most successful explanation for this convergence in case of small molecules has related the convergence temperature to the equation of state of pure water [1]. Convergence, however, is not expected to be universal, but depends on the size of the solute [33]. Small solutes can be accommodated in the open hydrogen-bonded structure of liquid water by molecular-scale thermal fluctuations, whereas the hydration of larger solutes requires the formation of an interface similar to the vapor-liquid interface of water [39] (see figure 1.1.1). In the context of soluble proteins, due to this length scale dependence the applicability of entropy convergence has been questioned [33,255]. Here, we investigate the hydration thermodynamics of macromolecules with the help of single molecule sensors and find that the basic concept of entropy and enthalpy convergence is still applicable at these length scales. The measured ion specific shift of convergence temperatures relates the hydrophobic attraction to the Hofmeister effect.

5.1 Universal convergence for different types of polymers

On the example of three different polymers, PAAm, poly(Glu), and eADF-4, we investigate the influence of the polymer composition on hydration thermodynamics as well as the effect of dissolved ions.

Measurements were performed in water or aqueous solution of NaCl or K_2HPO_4 at different temperatures and constant pressure. Pulling at one end of the polymer stretches the molecule during desorption into a fully extended conformation in solution, and thus successfully avoids coiling or aggregation of parts of the polymer. This can be verified by the sharp distribution of detachment length that approximates the expected contour length of the polymer (comparable to figure 2.1.2).

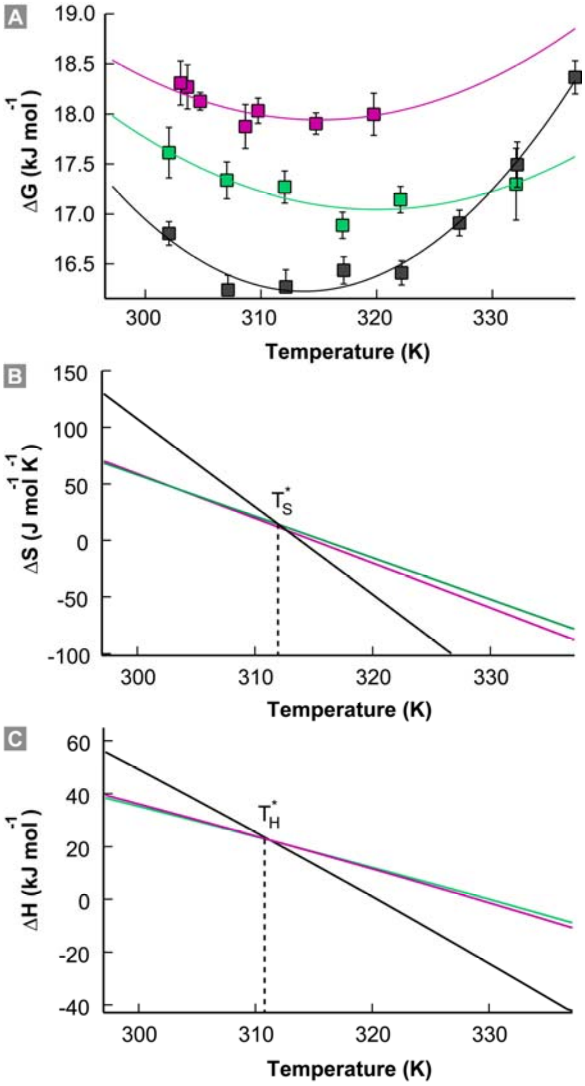

Figure 5.1.1: (A) free energy (B) entropy and (C) enthalpy change upon solvation of spider silk eADF-4 (black), poly(Glu) (violet), and PAAm (green) in water at varying temperature.

The difference in free energy, ΔG, controls the transfer of the polymer from the solid/liquid interface into solution and can be separated into an entropy difference, $\Delta S = -\delta/\delta T \cdot \Delta G$, and an enthalpy difference $\Delta H = \Delta G - T\Delta S$. As can be seen from figure 5.1.1, unfavorable enthalpy changes (figure 5.1.1 (C)) dominate the room-temperature hydration and are partly compensated by favorable entropy changes (figure 5.1.1

(B)).[iv] In addition, the entropies and enthalpies of hydrophobic hydration are strongly temperature dependent. The entropy difference decreases rapidly with temperature leading to the reversed situation with unfavorable entropy dominating the free energy, partly compensated by a favorable enthalpy change.[v] Thus ΔH which is positive and reasonable large in magnitude, decreases with temperature and becomes even negative at above 320 K. Accordingly, ΔG would also decreases with temperature. On the other hand, a process that requires specific spatial organization of hydrogen bonding patterns comprises an important entropic component and ΔG increases with temperature if the entropic cost becomes dominant [31]. Together the resulting free energy cost ΔG of hydration is non-monotonic and the resulting solubility represented by ΔG/T [250] exhibits a solubility maximum in the range 313-316 K (figure 5.1.2).

As expected the temperature dependence varies with varying degree of polar groups. The mildly hydrophobic eADF-4 with a large number of non-polar amino acid residues exhibits a greater sensitivity on temperature than Poly(Glu) or PAAm. The entropy variations from one polymer to another are small in a limited temperature range around $T_S^* = 311$ K, close to the temperatures at which they become zero. The enthalpy changes likewise converge around $T_H^* = 311$ K. The origin of this approximate convergence is by now well understood [1,252]. It is a typical feature of hydrophobic hydration and is common to both the hydration of small hydrophobic model compounds such as rare gases [256], alkanes [257], alcohols [258] and cyclic dipeptides [259] as well as protein unfolding thermodynamics [260].

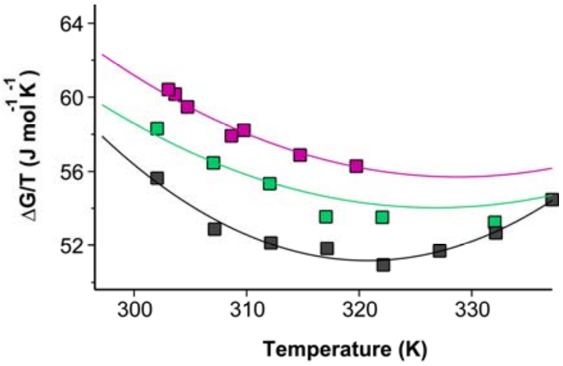

Figure 5.1.2: Massieu-Planck function for the solvation of eADF-4 (black), Poly(Glu) (violet), and PAAm (green) which is related to the solubility maximum of the polymers.

Our results show that this characteristic fingerprint of hydrophobic hydration is also present in the forced hydration of proteins and polymers from a nonpolar surface into water. However, T_S^* and T_H^* are shifted to lower temperatures compared to the hydration of small molecules. Most interestingly, the resulting range for these exceptional temperatures around 311 K in the case of polymers lies well in the biologically functional regime.

The fact that T_H^* and T_S^* are almost the

[iv] The predominant enthalpic role in hydrophobic hydration at room temperature for the amphiphilic molecules is replaced by dominating entropies in the case of the model compounds which are almost exclusively of nonpolar character.

[v] The reason for this is that the free energy of a process involving significant changes in the number of molecule interactions, such as the breaking of hydrogen bonds is dominated by its enthalpic component. With a sufficient increase in temperature, however the extent of hydrogen bonding between water molecules diminishes, and maintaining hydrogen bonds becomes less important.

same for polymer hydration indicates that polar and non-polar interactions are similarly important, in concert with calorimetry data on protein stability, which likewise provided equal convergence temperatures for ΔH and ΔS [251]. In contrast, it was shown for the solvation of small particles which were almost exclusively non-polar in nature, that with decreasing polar content, T_H* shifts to lower temperatures, away from T_S* [251]. Hence, the relative position of T_H* and T_S* can be taken as indication of the partial polar contribution to the hydrophobic attraction. Based on the solvation experiments of compounds with varying amount of non-polar groups it has been hypothesized that the hydrophobic (non-polar) contribution to ΔH and ΔS at their respective convergence temperatures are zero, because at these temperatures the solvation process obviously becomes independent of the variable non-polar contribution. ΔH at T_H* (ΔH*) can then be attributed to polar and van der Waals interactions, while the value of ΔS at T_S* (ΔS*) can be attributed primarily to configurational entropy. As we are solvating a long polymer in an extended conformation, ΔS* will include not only ΔS of hydration of the polar groups, but also translational and vibrational contributions, and contributions from internal and overall molecular rotations. In the present case both contributions, ΔH and ΔS are large in magnitude, however the net effect is small compared to the total values and hints towards a subtle balance of the enthalpic and entropic changes (figure 5.1.3), in agreement with recent MD simulations on the hydrophobic effect on polymer desorption [49].

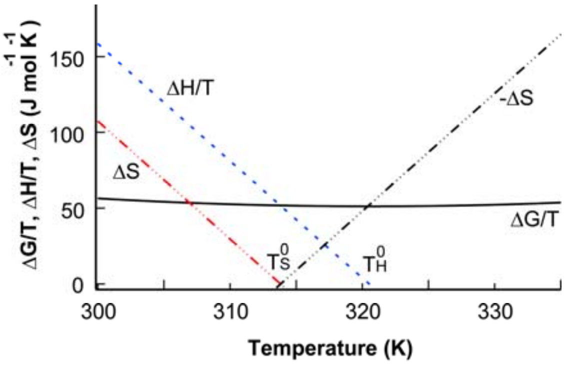

Figure 5.1.3: Massieu-Planck function and its constituting enthalpy and entropy change for the hydrophobic hydration of eADF-4 in water. T_S^0 and T_H^0 represent the temperatures of zero entropy and enthalpy, respectively. At T_S^0, ΔG has its minimum, ΔG/T becomes minimal for $T=T_H^0$. ΔS and ΔH/T are large in magnitude, but are nearly cancelling each other and result in only a small net effect in terms of ΔG/T.

Care must be taken in applying former conclusions derived from model compound data to larger systems such as proteins [48]. Huang and Chandler [33] argued that for species larger than ~ 10 Å entropy convergence does not occur, and therefore proteins would not exhibit this phenomenon. In our approach, the external force which transfers the molecule from the surface adsorbed state into the stretched state in solution prevents the formation of a coil conformation and might provide a small surface curvature of the molecule small enough to ensure hydrophobic hydration below the critical length scale. The amino acids are pulled one by one from the interface. This opens an avenue to the systematic investigation of the contribution of different amino acids to the hydropobic attraction of proteins, as we show here on the example of poly(Glu), or the evaluation of the net effect of a specific protein sequence like in case of eADF-4.

The forced desorption at nearly infinite dilution (single molecular level) avoids clumping or clustering of residues. Such clustering however does occur in bulk solution and in effect produces hydrophobic units of various sizes. As a consequence convergence might occur at lower temperature or might even be no more detectable [33].

5.2 Ion induced shift in convergence temperatures

It has been hypothesized that the effect of ions might be reflected in either the absence of convergence temperatures or a shift of these temperatures compared to pure water [261]. In the following, we will put this hypothesis to the proof. We measured the free energy of solvation for eADF-4 from hydrophobic, hydrogenated diamond into aqueous solution of NaCl and K_2HPO_4 at different salt concentrations (50 mM and 500 mM) and varying temperature. The free energy of hydration increases with increasing salt concentration, in line with previous theoretical considerations (figure 5.2.1 (A)) [254]. In both salt solutions up to 300 K, the free energy of transfer is composed of favorable entropies and unfavorable enthalpies. We find the strengthening of the hydrophobic attraction in this temperature range to be predominantly enthalpic in origin and entropic at higher temperatures (figure 5.2.1 (B), (C)).

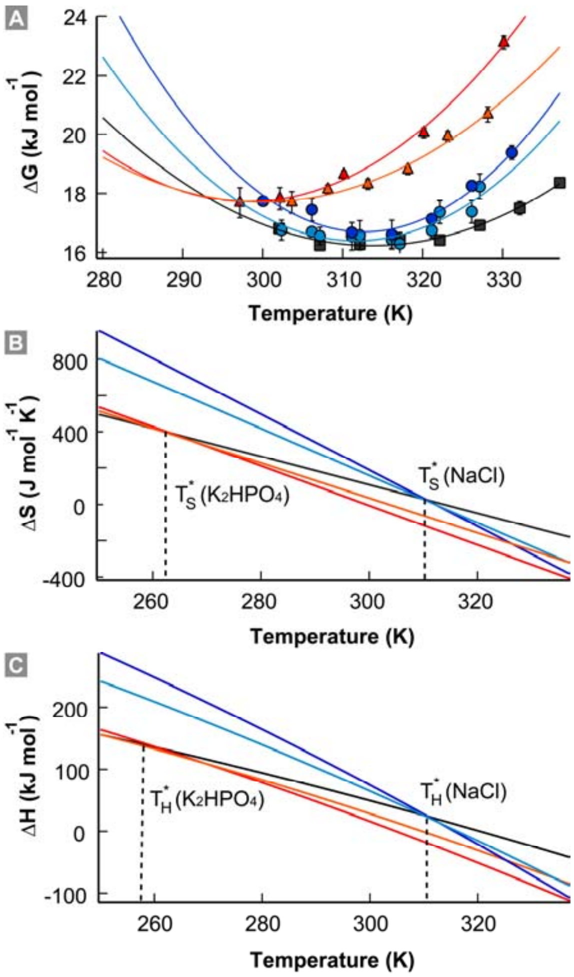

Figure 5.2.1: (A) free energy, (B) entropy, and (C) enthalpy change upon solvation of spider silk eADF-4 in water (black) and aqueous solution of NaCl (50 mM, bright blue, 500 mM, dark blue) and K_2HPO_4 (50 mM, orange, 500 mM, red).

Salt effects on the hydrophobic interaction have been the subject of several recent experimental and molecular dynamics simulation studies [130,166,249,262,263]. Their results on the hydrophobic attraction for molecular sized solutes in NaCl solutions are consistent with our finding of the hydration of small solutes in NaCl solution being prevalently enthalpic in origin at room temperature.

This justifies the comparison of the

additional entropic cost ΔS caused by the salt in our single molecule experiments with the entropic change ΔS^{Str} associated with the water structural changes upon ion addition. The latter was found to be related to the kosmotropicity of the ion, as reviewed in [89]. If one isolates the entropy changes related to the ions by subtracting the hydration entropies obtained with eADF-4 in electrolyte solution from those in water, it becomes apparent that the resulting ΔΔS related to the presence of K_2HPO_4 is negative over almost the whole accessible temperature range (figure 5.2.2).

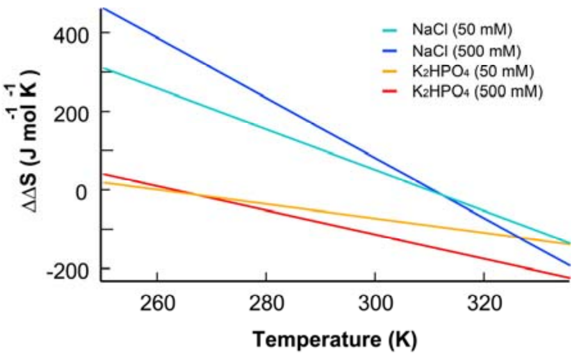

Figure 5.2.2: Difference in entropy change between the hydrophobic hydration of eADF-4 in electrolyte solution and pure water (ΔΔS) which is linked to the structural entropy change of water upon solvation of the respective salt ions (ΔS^{Str}). ΔΔS for K_2HPO_4 is negative throughout the relevant temperature range, marking it kosmotropic, whereas ΔΔS for NaCl changes sign at 312 K and must be considered as chaotropic below this temperature. The color code is the same as in the previous figure.

Negative values for ΔS^{Str} define the ion as kosmotropic (strongly hydrated, stabilizing protein structure), whereas positive values are typical for chaotropic ions (weakly hydrated, destabilizing). In case of NaCl we face a very interesting behavior, the corresponding values for ΔS^{Str} are highly temperature dependent and change sign at about 312 K. This implies that NaCl can act as chaotropic as well as kosmotropic cosolvent, depending on the current temperature. The values found for NaCl and K_2HPO_4 are in fairly good agreement with the values for the structural entropy change listed in reference [89] and citations therein. This surprising result may shed some light on the controversy of how to characterize NaCl which is sometimes considered chaotropic and sometimes kosmotropic in nature.

The difference in their attractive interactions with water manifests itself in different values for ΔS for NaCl and K_2HPO_4 along with different temperature dependencies. These properties also arise from the particular positions of the entropy convergence temperatures. This gives rise to the idea of using T_S* as indicator for the stabilizing properties of a specific ion in solution. Accordingly, the classification as kosmotrope or chaotrope could be done based on the position of T_S*. The Hofmeister series ranks salts, in part, according to the reduction of solubility of nonpolar compounds or protein stability. A future verification of an analogy between additional salts of this series and the shift in T_S* could corroborate our assumption.

5.3 Concluding remarks

In summary, the interactions of non-polar model solutes such as cylic dipeptides, alkanes, alcohols etc. are intermolecular, while those in a protein are intramolecular and thus largely dependent on the chain entropy. Former theoretical considerations on the hydrophobic hydration of model solutes in accord with experimental results have formed the basis for thermodynamic treatment of the hydrophobic attraction. However there is quite a gap to the stability analysis of proteins. The polypeptide backbone with enormous steric effects could easily interfere with the concept of entropy convergence. Evidently, this is not the case. We were able to reproduce characteristic temperature signatures including entropy and enthalpy convergence for amphiphilic proteins and homopolymers. In addition an ion specific shift in these convergence temperatures was detected, when the polymers were pulled into electrolyte solution, which could be linked to the hydration behavior of the ions and the Hofmeister series. In the next chapter we will use the effect of temperature and salt on the hydrophobic forces to control protein folding at surfaces. Further studies of this sort will contribute to a better understanding of the functional temperature ranges of biophysical structures and aqueous phase nanotechnology designed by analogy with the molecular machinery of biophysics.

Chapter 6

Surface Induced Protein Folding

Amyloidogenic peptides are well known due to their tight relation to protein-misfolding diseases, but they do also often have regular biological function. Even though the ability to adopt amyloid conformation is supposed to be generic, the propensity to do so can vary markedly depending on the environment. In this chapter we take advantage of our single molecule sensors to ensure that the populations of the different conformational states are not affected by possible oligomeric precursors from solution. We prove that structure formation within a single spider silk protein is induced in the vicinity of surfaces with high surface energy, and can be prohibited in the presence of hydrophobic surfaces. This transition from the unstructured native state into the final fold is also facilitated by adding salts as well as by rising temperature. Finally, the molecular structure at the surface and its stability are determined, which show striking similarities with the conformation of amyloidogenic peptides in their fibrilar assemblies.

Amyloidosis is a mechanism that underlies many protein-misfolding diseases, it is initiated by a structural transition from natively unfolded to β-sheet conformation followed by a nucleation dependent aggregation process [264]. The ability of peptides to form amyloid structures is not restricted to those proteins associated with recognized clinical disorders, including type II diabetes, Alzheimer, Parkinson's, prion, and Huntington disease [265], but is also present in high-performance protein nanomaterials such as silk [266,267]. In addition, amyloid formation is now recognized as a generic feature of polypeptides of diverse amino acid sequences [268]. Evidence has accumulated that the formation of this secondary structure can be induced within the protein in the vicinity of a surface such as a lipid membrane [269-271].

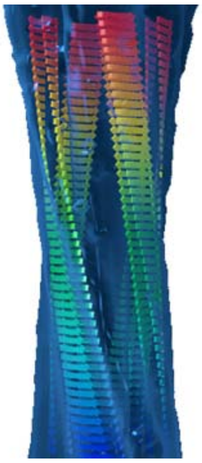

Figure 6.0.1: Schematic of the structure of the molecular assemblies within an amyloid fibril. Multiple peptides adopt a cross β-structure. On larger scale the β-sheet structures are twisted.

The final fibrous form of amyloids is easy to observe and the growth of fibers on surfaces has already been followed in real time [272]. But not much is known about the early ordered structures and their initial assembly. These ideas are motivating the investigation of the most elementary steps in the folding process, namely the role of the individual molecule, by both experimental [273-277] and theoretical approach [278]. Investigations so far have focused on the molecule's properties within the fibrilar assemblies. In contrast, we use SMFS to measure with a single spider silk protein on different substrate materials under various solvent conditions. We investigate the surface induced structure formation of eADF-4. The protein is natively unfolded in solution, but adopts β-sheet structure when assembled into fibrils [266]. However, little is known about the folded structure of the individual protein, because neither natural nor engineered spider-silk have been crystallized so far.

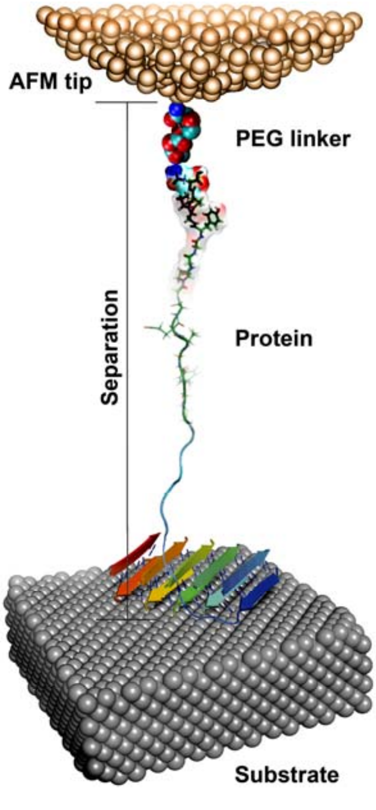

Figure 6.0.1: Sketch of a single molecule desorption experiment of eADF-4 attached to the AFM tip via a PEG linker (not to scale). Here the molecule exhibits β-sheet structure on the solid surface.

For the following experiments a single eADF-4 molecule was used as molecular sensor (figure 6.0.1) to measure in solution of varying temperature ranging from 20 to 70 °C. As described earlier, the tip with the protein was brought in contact with the solid for one second to adsorb and possibly to form its secondary structure before being retracted. This is done several hundred times to analyze the stochastic nature of desorption and eventually of mechanical unfolding.

According to the common practice, the forced desorption of eADF-4 from its N-terminal to its C-terminal end upon retraction of the cantilever at a velocity of 1 µm/s occurred close to equilibrium under most conditions as indicated by the observed velocity independent force plateaus (figure 6.1.1) [49]. A plateau length equal to the contour length of the polymer (like in most traces in figure 6.1.1), is indicative of missing stable structural features that resist forces higher than the plateau force.

6.1 Temperature facilitated folding of eADF-4 on hydrophilic steel surfaces

The traces above 48 °C in figure 6.1.1 are qualitatively different. Here, a regular pattern of peaks with amplitudes ranging from 70 to 200 pN appear on top of the desorption plateau. They are the characteristic finger print for unfolding of secondary structural elements [118]. The observation of the full contour length of eADF-4 at 48°C indicates the complete unfolding of all secondary structures.

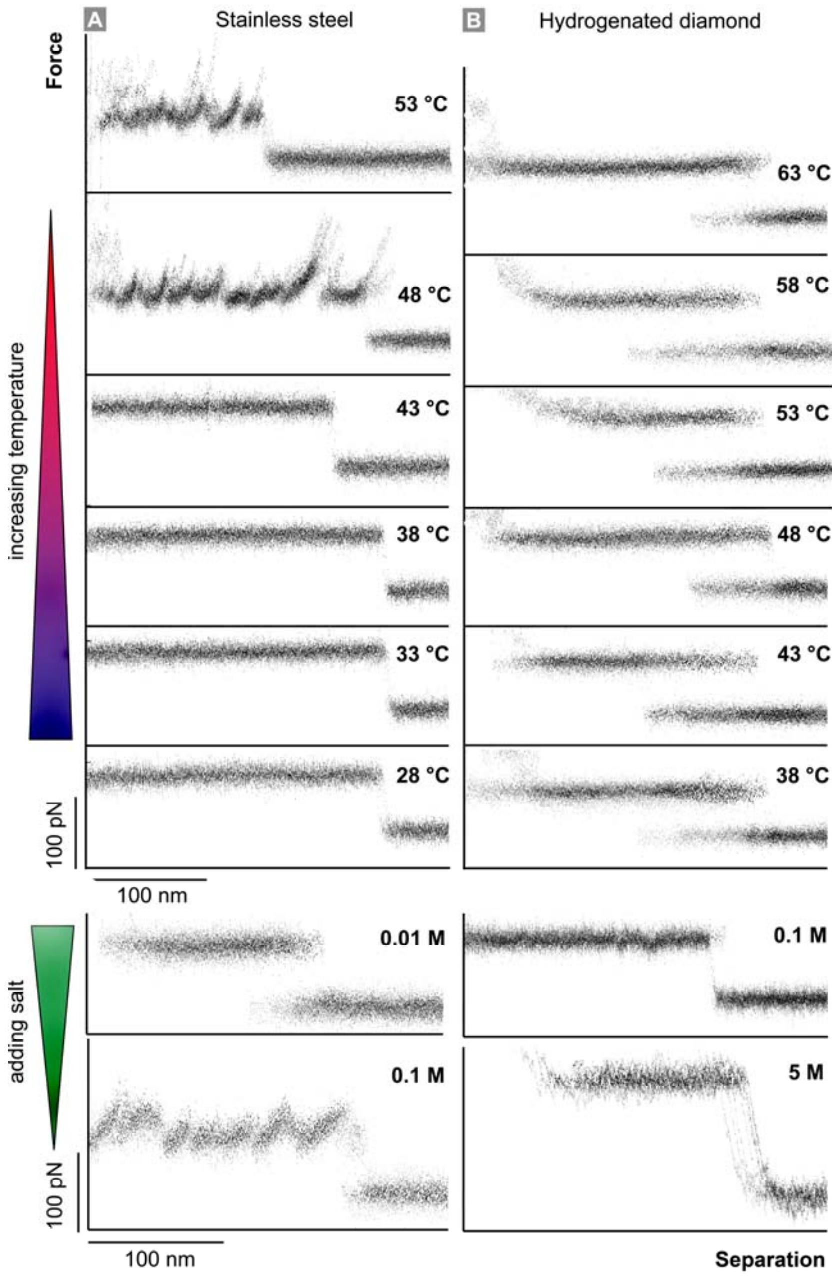

Figure 6.1.1: Force-extension traces of a single eADF-4 molecule in water at varying temperatures (top) and phosphate concentrations (bottom) desorbed from stainless steel (A) and hydrogenated diamond (B). The increased plateau height for the desorption at 5M salt concentration (B, bottom) stems from the larger desorption free energy at high ionic strength.

A detailed analysis of these peaks allows extracting both, distances to the transition state and transition energies and hence enables us to deduce the secondary structure of eADF-4 and its stability, as will be discussed in the following.

Before we have a closer look at the structure itself, we discuss the conditions for the structural transition. All the data in figure 6.1.1 (A) were recorded with one and the same AFM tip and covalently attached eADF-4 molecule, respectively. The only parameter that was changed was the solution temperature. We can therefore note the temperature around 48 °C as the transition temperature for structure formation on hydrophilic stainless steel. Figure 6.1.1 (B) depicts the same experiments on hydrophobic, hydrogenated diamond. Even up to 63°C no conformational transition is observed. So the structure is not preformed in solution, but is truly induced by close contact with the substrate material, the polar character (and thus high interfacial energy) of which is most probably the reason for the structural rearrangement of the spider silk molecule. The surface energy was determined from contact angle measurements to be for steel 38.0±1.8 mJm^{-2} and 18.8±1.3 mJm^{-2} for hydrogenated diamond (compare to section 4.1). As can be seen from the bottom part of figure 6.1.1, not only temperature, but also a higher ionic strength of phosphate of about 100 mM is capable to facilitate the transition in line with previous bulk experiments [279], but again only on the hydrophilic metal substrate.

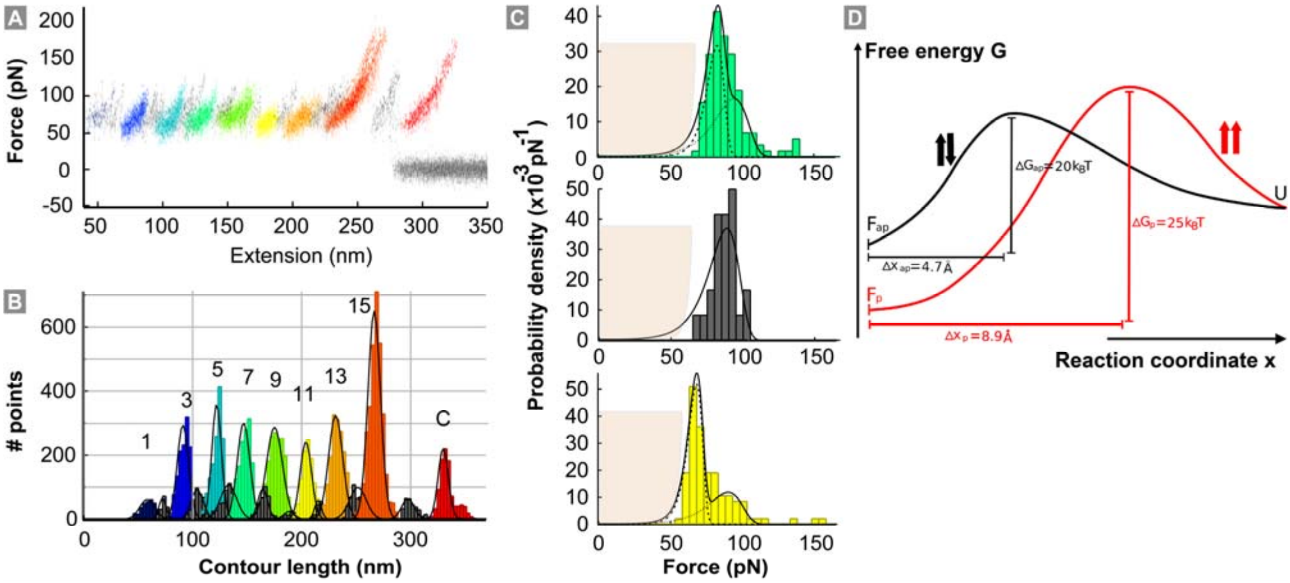

Figure 6.1.2: Analysis of the surface induced eADF-4 structure at elevated temperature. (A) Superposition of 20 force-extension curves of eADF-4 with odd peaks being marked in color. The traces were recorded in salt solution on steel (316L) at room temperature. (B) Averaged barrier position histogram obtained by transformation of each of the 15 unfolding peaks with a persistence length of 5.1 Å into contour length space and averaging the 20 resulting barrier position histograms for each peak. (C) Unfolding force distributions and normalized unfolding probability density for three sequential unfolding barriers (same color coding). The shaded area in the lower force regime illustrates the resolution limit of the instrumentation. The best fit to the data (solid black) reveals two discrete barrier binding potentials: a low force unbinding ~ 75 pN (dashed) and high force unbinding ~ 90 pN (dotted). (D) Energy landscape of eADF-4 unfolding.

What are the characteristic features underlying the surface induced structure of eADF-4? Following previously described methods [151] we transformed the 20 force-extension traces from figure 6.1.2 (A) into contour length space and obtained area-normalized histograms that directly represent particular locations along the polymer contour which constitute an energy barrier for unfolding (figure 6.1.2 (B)). By using a

Gaussian fit for each individual peak position, the locations of the energy barriers were determined. The histogram shows 16 equidistant unfolding barriers corresponding to the 16 repeats of eADF-4 plus one terminal barrier originating from the detachment of the C-terminus from the surface. On the basis of the recombinant spider silk protein sequence and the measured contour length positions, we can identify the amino acid sequences which form the bonds. This suggests that the poly(Ala) sequences of eADF-4 form the core structural elements which constitute the intramolecular connections between different repeats, in accord with previous findings [280]. There is an obvious asymmetry between the odd and even barriers, when sequentially numbered starting at the N-terminal end. The barriers with even numbers are probed less frequently (~ 40%) than those with odd numbers. This points to a pairwise coupling of two neighboring poly(Ala) patches into 8 associated doublets at the surface.

Further insight into the structural arrangement is gained by the investigation of the force distributions of individual rupture peaks and comparison to MD-simulations. For a detailed analysis of force distributions, well-defined loading rate conditions through a constant spacer length are essential [281]. Therefore, all 16 rupture peaks have to be analyzed separately. To determine the dissociation rate constants and the potential widths of bond breaking we employ the probability density function for the rupture forces derived by Evans and Ritchie [282] as a fit function to our data that uses the dissociation rate constant and the potential width as fit parameters [148,281,283]. The potential width is the distance between the folded state and the transition barrier along the unfolding pathway. Figure 6.1.2 (C) displays three out of 16 consecutive force histograms together with their probability functions fitted to the data based on the assumption of a one-barrier binding potential. These histograms again differ from odd to even unfolding events. The former have to be fitted with two separate transition probabilities instead of only one in case of even barrier numbers. The derived potential widths for the eight prevalent unbinding events (odd numbers) and the first four rare events (even numbers) are summarized in table 6.2.1. We find a short potential width of 4.7 Å for the high force unfolding and a longer width of 8.9 Å for the lower range forces. The derived values are well reproduced except for the last two which are influenced by the C-terminal surface anchor. Our study of the conformational transition caused by increased salt concentration on steel yields similar values and suggests an equal folding mechanism (see section 6.3).

Without further assumptions, the data presented so far can be explained most likely by the following surface induced structure of eADF-4. The protein is likely to orient with functional groups of high polarity, i.e. the backbone amide groups in poly(Ala), towards the hydrophilic metal surface, which is oxidized to a great extent under the experimental conditions. Thus, in contrast to what can be expected for a hydrophobic surface like diamond, steel conditions the poly(Ala) repeats for β-sheet formation perpendicular to the surface plane. The alternation between frequent and rare peaks is likely to be caused by a two-layer β-sheet arrangement, consisting of β-strand-coil-β-strand motifs connected by inter-strand hydrogen bonding, that are stacked against each other via side chain interactions parallel to the surface plane (figure 6.2.1 (A)).

6.2 MD simulations of forced eADF-4 unfolding – parallel vs. antiparallel arrangement

Gräter and Xiao tested this scenario by force-probe MD simulations. For details we refer to ref. [M12]. While both the structural details and interaction forces between proteins and heterogeneously oxidized metal surfaces are largely unknown, previous studies of amino acids on noble metals have found polar interactions to prevail. We here assumed steel to mainly serve as a template, inducing order in the poly(Ala) segments similar to the role of shear flow in silk fibrillogenesis. We thus approximated the experimental system with a surface made of Lennard-Jones spheres onto which $(Ala)_8$ peptides were assembled as described above and shown in figure 6.2.1 (A). We indeed find a single layer of β-strands adhered to the surface to be structurally unstable and to exhibit rupture forces undistinguishable from the desorption plateau of the non-structured eADF-4 sequences. Hence, at least a double layer is required to explain the measured force profiles, confirming our structural predictions. Various relative orientations in a double layer can be envisioned, which can be grouped into anti-parallel, parallel, and mixed arrangements (figure 6.2.1 (A)).

From force-probe MD simulations, independent from the detailed arrangement, we find strands in the upper layer to detach from the surface-adhered crystalline structure with forces of 300-400 pN. This step (odd numbered peaks) thus requires forces significantly higher than the desorption forces of non-structured eADF4 sequences ranging from 50 to 200 pN. The increased forces arise from the rupture of strong hydrogen bonding to the adjacent strand (figure 6.2.1 (B)). Instead, the subsequent rupture of the lower strand, not stabilized by inter-strand hydrogen bonds anymore but only adsorbed to the surface, does not give rise to a force peak, in agreement with a lowered frequency of even-numbered peaks in the contour length histogram (figure 6.1.2 (B)). Interestingly, strands in anti-parallel arrangements show higher forces (405±24 pN) and smaller transition distances (1.5±0.2 A) than those in parallel arrangements (286±27 pN and 2.5±0.2 Å), as previously found for the structurally related silk crystalline units [278]. These differences qualitatively agree with the two discrete unfolding barriers observed for odd numbered peaks (figure 6.1.2 (C)) and table 6.2.1. This suggests the experiments to probe a ~2:1 mixture of parallel and anti-parallel β-sheets in the steel-induced assemblies. We note that the experimental distances to the transition state obtained at 48°C are wider than those from simulations, carried out at room temperature, by a factor of ~3 which we attribute to the reported temperature softening of the protein [148]. Alternatively but less probably, a strand-turn-strand motif can be surface-assembled such that the pulling force acts onto the strand in the lower layer first, resulting in a concurrent detachment of the whole motif and therefore causing higher forces,

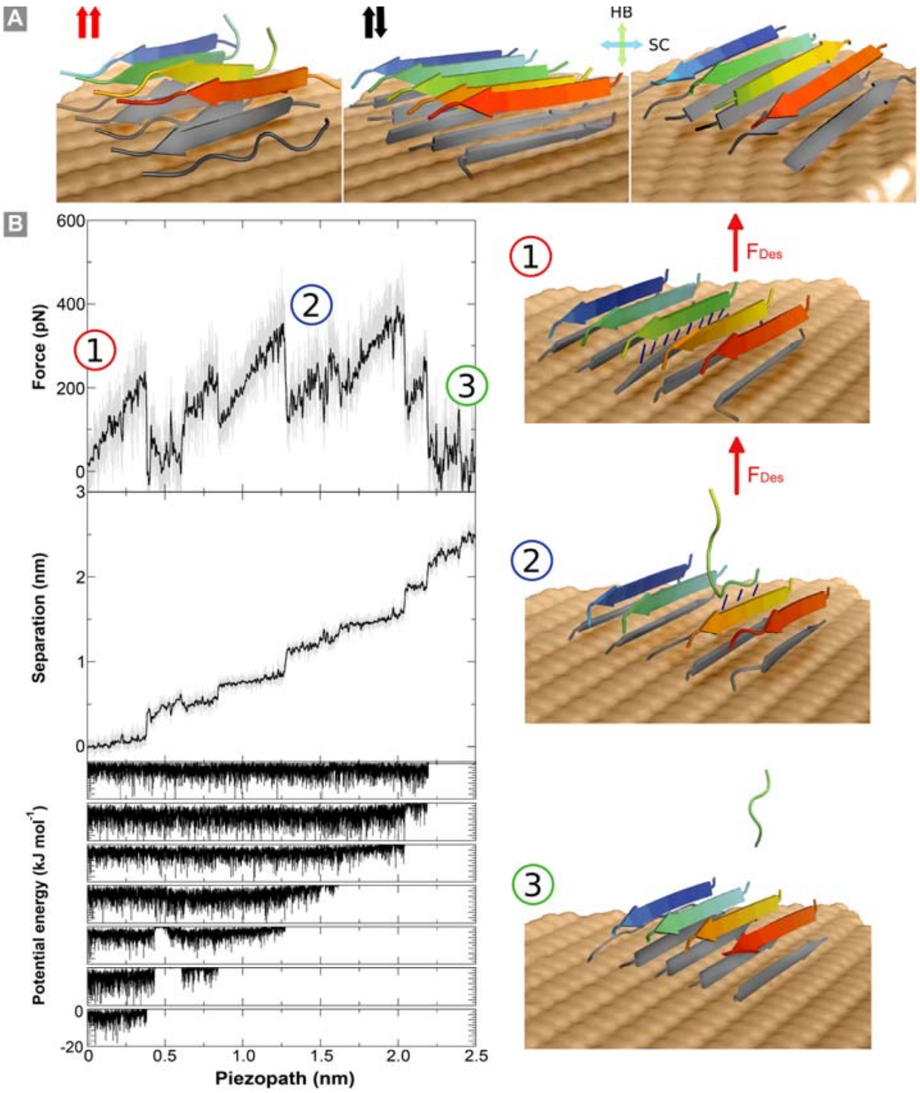

Figure 6.2.1: Force-probe MD simulations of the eADF-4 desorption from a surface. (A) Parallel, antiparallel and mixed arrangments of the β–strands. (B) Simulated force curve (top), vertical position of a β-strand, which is pulled at constant velocity (middle) and the H-bond potential energy of the same strand. The corresponding simulation snapshots of the positions 1-3 are shown in the right panel.

as observed for the rare peaks in figure 6.1.2 (B) and in corresponding MD simulations (498±55 pN). Remarkably, when detaching a β-strand-coil-β-strand motif from within the two-layer β-sheet system in this way, we observe the structure to self-heal by sealing the introduced flaw on the nanosecond time scale of the simulations. Finally, the plateau of constant force underlying the unfolding pattern stems from the desorption of the Gly-rich chain segments between the poly(Ala) patches, which behave like a non-structured flexible polymer with high in-plane mobility.

Taken together, our structural model of a single eADF4 molecule derived from force spectroscopy is in line with the MD simulations. It also shows remarkable similarities with typical protein structures within amyloid aggregates [284], and is nicely complemented by previous studies on the structure of eADF-4 assembled into nanofibrils on the timescale of hours and into microspheres within seconds [285]. These studies propose a similar cross β-structure for the amyloidogenic proteins in their fibrilar assemblies, in which the peptides form β-strand-turn-β-strand motifs via side chain interactions and are connected by hydrogen bonds along the fibril axis [286]. Our combined experimental and theoretical data suggest parallel β-sheets to outnumber anti-parallel counterparts in the surface-induced assembly. In our predicted structure, the non-structured Gly-rich segments thus have to cover a distance of ~5 nm between the C-terminus of the nth strand and the N-terminus of the (n+1)th strand. This distance of 5nm happens to be in the range of end-to-end length for this 27-residue segment (assuming a freely-jointed chain with a persistence length of 0.5 nm), rendering our structural model a likely candidate. Additional support of our model is provided by the observed general preference of parallel β-sheets of amyloidogenic peptides [284] and the parallel/anti-parallel mixture in silk fibers determined by Asakura et al [287].

What can be learned about the process of structure formation itself? The frequency of occurrence of the short and wide potential widths gives us some hints. We primarily observe a repeated assembly of poly(Ala) patches into first the lower and then the upper layer, starting from the C-terminal repeat (odd numbers in the energy barrier histogram), while the reverse association with a β-strand assembled below its C-terminal neighbor (even numbers in the energy barrier histogram) occurs only rarely. Our experiments point to an assembly time scale below the dwell time of the molecule at the surface of 1s. We also quantified the unfolding rates under zero force for the two parallel and anti-parallel β-sheet assemblies from the unfolding probability density distributions (figure 6.1.2 (C) and table 6.2.1). The parallel structure exhibits a very low mean transition rate of $1.5 \cdot 10^{-4}$ s^{-1}, which compares for example to that of the strong fold of the muscle protein titin, ubiquitin or the extracellular matrix protein tenascin [111,288,289]. In contrast, the mean transition rate of the anti-parallel β-sheet formed by eADF4 ($3.3 \cdot 10^{-2}$ s^{-1}) is two orders of magnitude higher and is similar to those of calmodulin and F-actin cross-linker filamin fibronectin [148,156]. From the transition rates we can calculate the transition energy by applying the Arrhenius equation and assuming an Arrhenius pre-factor of 10^{7} s^{-1} (see section 1.7). The values are depicted in figure 6.1.4 (C) in a scheme of the energy landscape.

This result might seem contradictory at first sight: the parallel structure which breaks first under load (low-force events in the unfolding force histograms) is stronger and hence more stable at zero force compared to the stiffer and mechanically more resistant antiparallel analogue. This can be understood if the differences in potential width are considered. As previously shown, the distance to the transition state has a high impact on the unfolding lifetimes of a bond under mechanical load, rendering the structure with the wider potential more susceptible to force-induced destabilization [143]. This might be vital to the outstanding mechanical performance of silk, in which the β-sheet structures constitute crystalline-like particles within the silk fiber and provide the thread's strength in the first place [266]. The structural elements that rupture first in the force bearing protein are more stable at zero load and will therefore rapidly reform the moment the molecule relaxes. The observed stress response behavior together with the special structural design acts as a reversible toughening mechanism increasing the energy needed to break the structure [290].

For the breaking of H-bonds in the eADF-4 fold the energy barriers of 20-25 k_BT just reflect the theoretically predicted universally valid critical number of 4-5 H-bonds that can break concurrently under any assembly geometry [291]. This indicates that only half of the 8 alanins per strand contribute to the H bond network strength. In case of eADF-4, the intrinsic strength limit of the H-bond assemblies is overcome by a structural hierarchy that alternately consists of discrete assembled units with confined H-bond content and entropic domains.

Table 6.2.1: Potential width and unfolding rate constants at zero force (water, 48 °C) for even and odd unbinding events (numbered sequentially starting at the N-terminus). The indices *p* means parallel and *a* means antiparallel arrangement.

# event	1	2	3	4	5	6	7	8	9	11	13	15	17
Δx_p (A)	8.5	-	8.6	-	8.7	-	9.0	-	8.3	9.9	9.3	3.0	4.6
k_p^{off} ($10^{-4}s^{-1}$)	1.3	-	1.5	-	1.4	-	1.4	-	1.5	1.6	1.5	$1\cdot10^3$	$2\cdot10^2$
Δx_a (A)	4.7	4.0	5.1	4.8	4.9	4.9	4.5	4.9	4.5	4.6	4.8	1.4	1.7
k_a^{off} ($10^{-2}s^{-1}$)	3.0	3.0	3.5	3.6	3.0	3.6	3.0	3.9	3.2	3.5	3.0	55	55

6.3 Surface induced folding of eADF-4 facilitated by increased ion concentration

The structure formed in aqueous PBS solution with a phosphate concentration of about 100 mM at room temperature could only be observed on the metal surface. On the other hand, on the low energetic, hydrogenated diamond the conformational transition did not appear. The force curves look very similar to those obtained on metal at high temperatures in water (figure 6.3.1 (A)). The force peaks could be identified and distinguished from the plateau level thermal noise which is due to the increased desorption force and hence an increased plateau level for the protein in salt solution. The energy barrier histogram deduced from 20 curves by transformation according to the WLC model into contour length space revealed striking similarities of the protein's structure formed in the presence of ions and the structure formed at high temperature (figure 6.3.1 (B)). Not only the positions of these barriers are the same but also the frequency of their appearance. Fitting probability density functions to the force histograms shows the same difference between odd and even barrier numbers: the first must be fitted with two separate functions while the latter can be modeled with a single function for the unbinding process (figure 6.3.1 (C)). Finally, within the uncertainties of the measurement, the values for the potential width (Δx) and the rate constants for unfolding k derived from these fits are very similar to those presented in table 6.2.1.

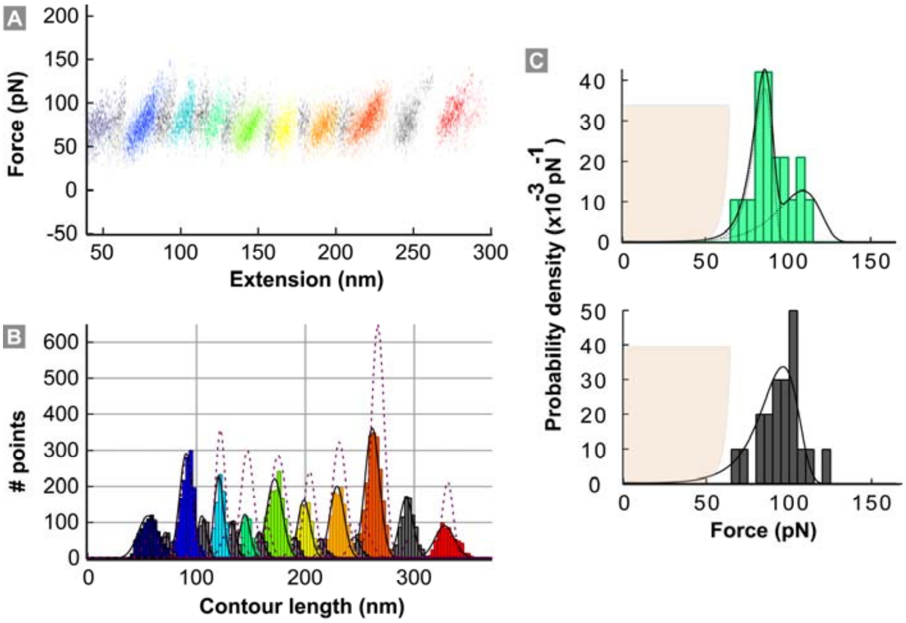

Figure 6.2.1: Analysis of the surface induced eADF-4 structure at increased ionic strength. (A) Superposition of 20 typical force-separation traces of eADF-4 recorded at room temperature in aqueous solution containing phosphate ions (100 mM). Odd peaks are marked in color. (B) Averaged barrier position histogram obtained by transformation of each of the 17 unfolding events with a persistence length of 5.1 Å and averaging each peak of the 20 resulting barrier position histograms. For comparison, the dotted lines mark the energy barriers induced by increasing temperature. (C) Unfolding force distributions and normalized unfolding probability density for two sequential rupture events (same color coding as A and B). The shaded area in the lower force regime illustrates the experimental cut-off function. Black lines indicate the probability density functions fitted to the data.

We obtain $k_p = 3.2\ 10^{-4}$ and $\Delta x = 8.0$ Å for the low force events which have been identified with the unfolding of parallel strands and $k_a = 2.8\ 10^{-2}$ and $\Delta x = 4.0$ Å for the more rare high force events due to disruption of antiparallel strands.

Taken together we conclude that eADF-4 adopts the same secondary structure on the metal substrate regardless of the conditions of structural transition investigates in this study. This agrees well with previous observations of equal secondary structures within eADF-4 spider silk assemblies formed under similar conditions. The reported difference in the assembly geometry (microspheres and nanofibrils) and the respective time-scale of formation has to be related to the high concentration of proteins compared to our single molecule study and possibly to the presence of oligomeric precursor structures.

6.4 Toughness Estimation of silk fibers from molecular parameters

These findings raise the interesting question whether the final fiber properties are mirrored at the molecular level by a single protein. In the following we will give at least a rough estimate. The toughness of a spider silk fiber from *Araneus* which outperforms that of any other engineered material, is 160 MJ m^{-3} [280] and corresponds to its energy to breakage. The number of molecular strands per fiber volume can be estimated according to ref. [292] to be of the order of 10^{26} strands per m^{3}. Based on the energy to break the peptide bonds of a random coil like protein of about 10 kJ mol^{-1} the calculated toughness is one order of magnitude smaller than the measured values.

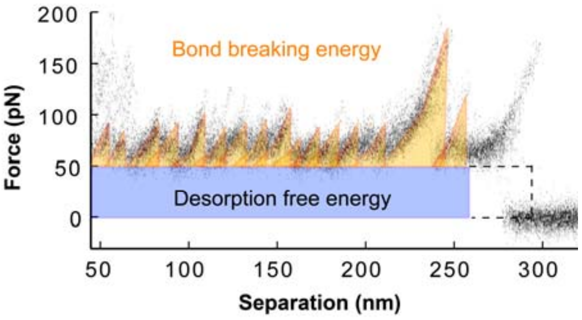

Figure 6.4.1: Desorption free energy and bond breaking energy of eADF-4 (C16) on 316L at 48 °C. The area under the superposition of 20 typical force-separation traces of eADF-4 is divided into the free energy contribution due to the equilibrium desorption (blue) at negligible molecular friction and thus energy dissipation (observed under all conditions) and the energy that is needed to break the bonds of the secondary structure (orange) formed at elevated temperature on steel.

However, if we in addition take into account the toughening effect that comes from the proteins secondary structure analyzed here by integrating the area under the force-separation traces, and subtracting the conserved free energy of desorption indicated by the force plateau (figure 6.4.1), we end up with an upper bound for the average toughness of 237 MJm^{-3}, assuming that 40% of the silk fiber adopt β-sheet conformation [280].

The dissipated bond breaking energy was determined by integrating the force-separation curves from 50 nm to 270 nm and subtracting the desorption free energy (area under the force plateau at 50 pN). This was done for 20 curves and the resulting energy values were averaged to provide a value of $1.7 \cdot 10^{-17}$ J for a single molecule. Assuming a density of 10^{26} strands per m^{3} [292] we obtain an energy to breakage (toughness) of 589 MJ m^{-3}. However, in a silk thread only about 40 % of the proteins are β-sheets [229,280]. If all molecules in the fiber are in their fully folded state this yields a maximal toughness of 237 MJ m^{-3} which is in remarkable agreement with the values of Gosline and co-workers [280]. This value is in fairly good agreement with the values measured for the fiber and reveals a distinctive structure-function relationship. Moreover, this conformance underlines the importance of the individual molecule’s ability of mechanistic energy absorption for the supreme material properties known from silks.

6.5 Concluding remarks

In conclusion, we were able to deduce the amyloid-like secondary structure of recombinant spider silk eADF-4 and its stability. Interestingly, the parallel orientation of two-stranded β-sheets stacked against each other along the metal surface is the secondary structure that is weaker under force but more stable at zero load and forms faster comparing to its anti-parallel counterpart, in line with their preferred formation on steel and in the related amyloidogenic fibers. We could demonstrate that the self-assembly of single protein molecules into these highly ordered structures on a surface depends on the substrate material and can be enhanced by elevated temperatures and increased ionic strengths, the role of which has been discussed in detail in chapter 5.

Chapter 7

Surface-Differential Cosolute Binding onto Polymers

Cosolutes are present in the crowded environment of all biological systems and modify, or even determine, the interactions between macromolecules such as proteins, lipids and DNA. At the same time, the interactions of cosolutes with macromolecules themselves are modified by the environment, in particular by surfaces like that of the cell membrane, or the surface of histones or microtubules. We use a joint experimental and theoretical approach based on the single molecule sensor and equilibrium thermodynamics to quantify the binding of cosolutes onto a macromolecule in solution as well as in its surface adsorbed state. We thus translate ligand binding equilibria into measurable forces. With this approach, values for the number of adsorbed cosolutes per length, their association constants, and the change in Gibbs free energy are obtained. This is demonstrated using the example of glucose interaction with PAAm in contact with surgical stainless steel and oxidized diamond. We find that cosolute binding onto macromolecules is very sensitive to the nano-environment and depends in a surface specific manner on whether the polymer is surface adsorbed or not.

Cosolutes can cause a protein to fold into its biologically functional native form, to associate, to adhere, or to desorb from an interface[293]. Some cosolutes protect proteins from denaturing and enable the adaptation of organisms to adverse environmental conditions and thus ensure their survivability[102]. Many macromolecule–cosolute interactions take place in the vicinity of a surface like the cell membrane or a histone. Examples are transmembrane solute transporters such as the glucose uniporter GLUT[294,295] or the DNA organization around histones[296]. The complexity of these four component systems (polymer-solvent-cosolute-surface) makes quantitative experimental approaches difficult, and leaves many important questions unanswered: How many molecules bind to a protein in the vicinity of the membrane and how many when it is not attached to the membrane? How strong are cosolutes ligated? What are the factors that determine the adsorption onto, or the release from, the macromolecule?

Specific ligand adsorption to individual binding sites can be studied using classical techniques such as fluorescence[297,298] or radioactive labelling[299], whereas non-specific low-affinity interactions as in glucose binding, proceeding equally along the whole polymer contour, a convincing strategy to count the number of associated ligands is only available for ternary systems (polymer-solvent-cosolute). In the latter case, the effect that adding salts or non-ionic cosolutes (e.g. urea, polyols and sugars) has on protein stability and preferential adsorption has been studied extensively by experimental techniques such as calorimetry[300], densiometry[301] or equilibrium sedimentation[302], as well as simulation methods[303,304]. However, little is known about the interactions in a four component system additionally comprising an extended surface.

Single molecule methods such as optical- or magnetic tweezers and AFM allow for the detection of forces and displacements in real-time at a single molecule level[305]. They do, however, usually necessitate a mechanical conversion of the binding event into a measurable extension difference, as is the case with protein binding induced compaction of DNA[306,307] or a binding mode specific shift of the DNA stretching transition[308]. Most cosolutes such as sugars, however, do not cause any measurable contraction or looping of the targeted polymers.

Here, we solve this problem by translating cosolute binding equilibria into measurable forces. To this end, we apply a single molecule sensor to extract information on cosolute binding to a polymer adsorbed onto a surface compared to an extended polymer conformation in solution. The difference in numbers of adsorbed cosolutes is directly transformed into a measurable force signal. By adapting the classical Gibbs adsorption formalism to the case of equilibrium desorption of a polymer from a surface, we obtain the fraction of binding sites occupied by the ligand in the vicinity of a surface and in solution, as well as the corresponding association constants. Our results allow us to identify factors that change adsorption affinities and thus to control adsorption in a surface-specific manner.

7.1 Surface differential binding of glucose onto PAAm at different temperatures

In the following we demonstrate that the suggested method is indeed capable of quantifying the binding of cosolutes to a polymer in both states: (i) adsorbed at the substrate surface and (ii) stretched in solution (figure 7.1.1).

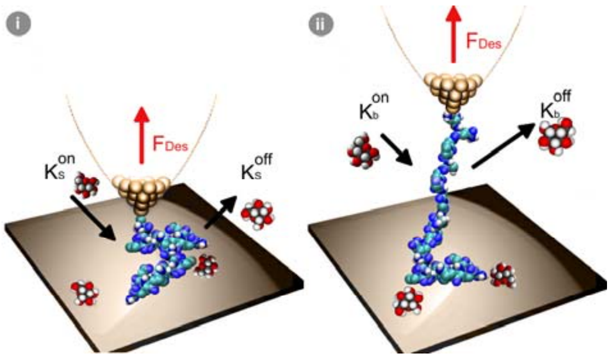

Figure 7.1.1: Scheme of glucose binding to a polymer in the two possible configurations. The on- and off-rates of glucose onto a polymer (i) adsorbed to a substrate (K_S) and (ii) in solution (K_b) are depicted. The differences in the association constants $K=K^{on}/K^{off}$ and the length of a glucose binding site can be determined from the measured desorption forces as a function of the cosolute activity (see section 1.8 for details).

As a molecular sensor we use a single PAAm molecule attached to an AFM cantilever tip. We measure in solutions of D-glucose at different concentrations ranging from 0 to 1 M. Moreover, the temperature was varied to determine its influence on the binding thermodynamics of glucose. In this study, we employ oxidized diamond and surgical stainless steel (316L) as substrate materials.

A precise determination of the binding parameters by means of the Gibbs adsorption isotherm under non-ideal solution conditions necessitates the force as a function of the glucose activity instead of concentration[309].

We therefore transformed the values for mole-fraction x of glucose into activities a according to $a = \gamma \cdot x$ by using the activity coefficients γ provided by refs. [310] and [311]. For moderate concentrations of weakly interacting cosolutes such as most osmolytes, the properties of the liquid are close to those of an ideal solution, and the activity coefficient is constant over a wide concentration range and close to 1. Therefore, the error that emerges when using concentrations instead of activities is small. However, there might be systems e.g. ionic liquids in which the use of activities is indispensible.

The plateau forces obtained on diamond increased with increasing glucose concentration (figure 7.1.2 (A)). Fitting of eq. (1.37) to the data obtained at 31 °C and 46 °C provides important quantities for each of the two states of the polymer on and off the substrate surface: the length of a glucose binding site along the PAAm carrier molecule and the corresponding association constants are summarized in table 7.3.1. Key to our fitting strategy leading to the curves in figure 7.1.2 and 7.2.1 is that we employ identical fit parameters in the bulk state, i.e. we fit our data simultaneously. This makes the fit parameters quite unique. K_S is about 8% higher than K_B at 31 °C and even more then 20% higher at 46 °C, meaning that more glucose molecules are associated to the polymer in the surface adsorbed state. This is unexpected, because from a geometric point of view there is less polymer accessibility for glucose at the substrate surface. These additional ligands are then released upon stretching into solution leading to an increased desorption force. With increased temperature, the equilibrium association constant increases. At the same time the length of a binding site, e.g. the effective distance between two neighboring glucose molecules increases as well. In effect, less glucose binds to PAAm at higher temperature in both states.

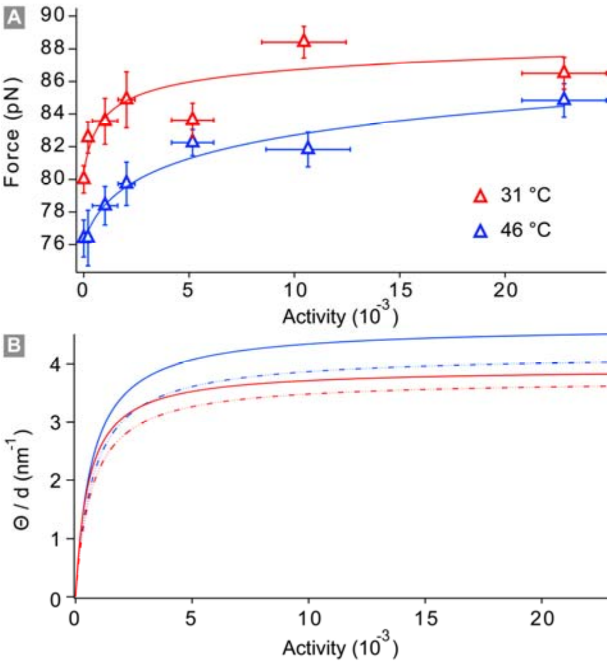

Figure 7.1.2: Glucose binding to adsorbed and solvated PAAm at different temperatures. (A) Desorption force of PAAm on O-terminated diamond in aqueous glucose solution at different concentrations at 31 °C (blue) and 46 °C (red). The solid lines are fits according to Eq. (7.4), the fit for 31°C is a simultaneous fit together with the data for steel (figure 7.2.1). (B) Resulting number of binding glucose molecules at the polymer surface adsorbed at the solid/liquid interface (solid lines) and stretched in bulk solution (dashed dotted line).

7.2 Effect of substrate material on cosolute binding affinity

In order to demonstrate that we are not only sensitive to the components of the ternary system comprising polymer, solvent and cosolute but also to the properties of the surface, we replaced the diamond substrate by surgical stainless steel while keeping all other parameters constant. We observe a qualitative change in the desorption force exhibiting a rather complex, non-monotonic dependence on glucose activity (figure 7.2.1 (A)).

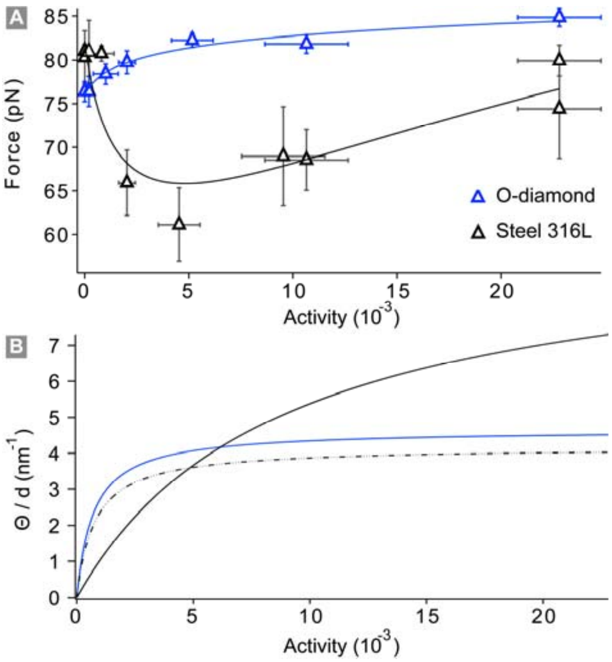

Figure 7.2.1: Surface differential glucose binding to PAAm on steel and diamond. (A) Desorption forces of PAAm at 31 °C with varying glucose concentration on surgical stainless steel (black), and from O-terminated diamond at 31°C is shown in blue. (B) The number of associated glucose molecules at the polymer in the vicinity of the surface (solid black line) exceeds that in solution (dashed dotted line) at a glucose concentration of about 0.2 M. For comparison, the number of binding glucose is also depicted for the polymer adsorbed at the O-terminated surface (blue).

Using our adsorption analysis, the force curves can be rationalized by a cross-over of different cosolute binding affinities. First, up to a concentration of 0.2 M ($a \approx 5 \cdot 10^{-3}$) more glucose binds to the solvated state rather than the adsorbed state of the macromolecule. That is to say, the number of associated glucose molecules increases upon the forced desorption of the polymer by an additional binding of the cosolutes in solution. However, at higher concentrations more glucose binds to the polymer adsorbed at the surface compared to its stretched conformation. Consequently, glucose molecules have to be released into solution and we observe a chain depletion during polymer desorption from the metal – similar to the O-terminated diamond (figure 7.1.2 (B)). The number of glucose associated to PAAm on the metal surface is decreased compared to diamond at glucose activities below 0.05. On the other hand, at higher glucose concentrations and activities, respectively the polymer ligates much more glucose when it is adsorbed on the steel substrate than on the diamond (figure 7.2.1 (B)).

The data presented here shows that at physiological concentrations, the adsorption behavior of glucose onto PAAm near a solid surface differs significantly from the one in solution. From this we can conclude that the presence of surfaces does indeed considerably influence cosolute adsorption behaviour. There is even a qualitatively different adsorption behavior of glucose onto PAAm for the two investigated surfaces. This is likely owing to a different affinity for glucose of the substrate material itself. At low glucose concentration, the sugar is repelled from the steel surface and hence shows a lower tendency to bind to the polymer when it is adsorbed on the metal, compared to the solvated state. With increasing amount of glucose present at the interface, the number of surface adsorbed glucose rises until a dense layer of glucose molecules is formed. From this point, the adsorption behavior is similar to that observed on oxidized diamond, with more glucose binding to the polymer at the interface compared to the solvated conformation.

Aside from their value as a model system, the results for the different materials used in this study are of direct relevance for a wealth of technological applications. Recent progress in the field of medical research gave rise to the idea of using diamond sensors for the diagnosis of metabolic diseases, such as the detection of chloride concentration in blood or sweat in the case of cystic fibrosis, or their use as implantable glucose sensors for the treatment of diabetes mellitus[240]. The working principle is that of a field effect transistor modified with DNA, enzymes or polymers which are immobilized on the substrate surface[216,239]. The presence of solutes is detected by a change in the drain-source-current upon binding to the macromolecule. Similarly, PAAm hydrogels are currently under investigation as glucose binding biomedical devices [312-314]. Our analysis reveals that the substrate material for the polymers used in the bioelectronics devices has a crucial effect on the binding affinity of small molecules, which in turn has to be taken into account for their rational design.

7.3 Comparison to standard methods for binding studies

Our differential measurement yields the number of cosolutes per unit length that adsorb (or desorb) from the polymer surface once it is transferred from an interface into solution. We can also determine absolute values for the number of bound cosolutes, the binding constant and the Gibbs free energy in both the adsorbed and the dissolved states. A further advantage of this thermodynamic method is that the average distance of bound cosolutes follows directly from thermodynamics and its fit to the experimental data.

Table 7.3.1: Binding parameter of D-glucose at PAAm on surgical stainless steel (316L) and oxidized diamond (O-diamond) at different temperatures.

	Steel 316L	O-diamond	O-diamond
Temperature	31 °C	31 °C	46 °C
K_b	1300	1300	1400
d_b [Å]	2.40	2.40	2.68
ΔG_b [kJ mol^{-1}]	18.13	18.13	18.32
K_S	114	1404	1789
d_S [Å]	0.99	2.15	2.55
ΔG_S [kJ mol^{-1}]	11.98	18.33	18.94

The accuracy of the obtained values depends on a couple of parameters. Firstly, the largest error for determining the desorption force stems from the determination of the spring constant of the cantilever[228]. When one and the same cantilever tip is used for all the measurements (as was done here), this uncertainty only causes a vertical shift of all data points and does not influence the values of the fit. Secondly, the physical model underlying the fit also affects accuracy. This is the validity of the Langmuir isotherm, namely negligible cosolute interactions, identical active sites of the polymer with equal free energy of adsorption and no more than a monolayer of associated cosolutes. In principle, the Langmuir model can be generalized to account for additional effects, but the model presented here describes the data well. Finally, the fitting procedure itself limits the accuracy because there are four fit parameters (c.f. eq. (1.37)) for the differential measurement, which are only determined to an order of magnitude for a single force versus activity plot. However, this precision increases substantially when data obtained with one and the same polymer but different surfaces are fitted simultaneously. For the example presented here with two surfaces, the parameters are already determined to better than ± 30% variation (see section D8).

Alternative experimental procedures to measure polymer-ligand interactions in thermodynamic equilibrium in close proximity of a substrate surface are hindered by either spatial or temporal resolution. Very specific binding could possibly be detected by fluorescence, but in this case one would have to work in a very dilute system (both for the macromolecules and the cosolutes), which is far from the crowded environment in a cell. Another common method employed to determine surface excess quantities makes use of radioactive tracers. Here the spacial resolution is mainly determined by the range of the (beta) emitter, which is far from molecular distances. Similar problems concerning the spatial resolution are faced using ellipsometry, x-ray or neutron scattering. For this reason, the single molecule approach presented in this communication might evolve to a powerful tool to quantify the interactions of small molecules with macromolecules in a quaternary system.

Even for ternary systems (solvent, polymer, cosolute) our method should be superior in many cases. The standard methods to date for the measurement of cosolute binding in bulk solution are isothermal titration calorimetry (ITC), densiometry, or sedimentation. Similar to our single molecule approach, ITC relies on the validity of the Langmuir isotherm and a fit function [315-317]. In addition, these methods require a minimum amount of polymer to provide reliable free energy changes, and association constants, and the precision of the data increases with molecular concentration. Thus, the availability of scarce and/ or expensive polymer samples constitutes a certain limitation to this method. Moreover, self-assembly and aggregation restrict the application of ITC to less hydrophobic molecules[300]. The AFM approach presented here constitutes a complementary technique capable of circumventing these restrictions.

A change of the measurement parameters is also possible. Once the shortening per bound cosolute is known (which was not necessary for the above calculations), the measurement of the detachment length of the polymer at constant force can similarly provide numbers of binding cosolutes. Note that during the equilibrium desorption the force-extension trace exhibits a plateau until the curve suddenly drops to the zero line the moment the polymer detaches from the surface (figure 2.1.2 (A)). The detachment length can thus be as easily determined as the desorption force in our single molecule approach (figure 2.1.2 (B)). This experiment can be done under exactly the same conditions as suggested by Zhang and Marko[163]. Instead of the desorption force we now measure the desorption length as a function of cosolute concentration and activity, respectively. Upon binding or release of compaction causing cosolutes during desorption, this length will vary and the line excess difference can be directly obtained by fitting the length variations as a function of cosolute activity, in line with the procedure described above. Accordingly, we are able to extract the exact number of bound cosolutes if the contraction per cosolute is known, or vice versa.

7.4 Concluding remarks

In conclusion, we have developed a new method based on single molecule sensors and equilibrium thermodynamics to determine the number of cosolutes binding to a solvated macromolecule and to the same molecule adsorbed at a solid substrate. When at least two different substrates are employed, this method provides reliable binding parameters such as the distances between neighbouring binding sites, free energies and association constants. This was exemplified for steel and oxidized diamond substrates, and can easily be extended to a wide range of interfaces ranging from solid-liquid, liquid/air or soft interfaces such as lipid bilayers, cell membranes or histone covered substrates. Thus, we expect that the combined experimental and theoretical approach is widely applicable for the study of cosolute interaction with macromolecules in bulk and in the vicinity of interfaces.

Future Prospects

An important field of future application of our single molecule sensors will certainly be protein conformational dynamics. In chapter 6 we studied surface induced protein folding and learned about the decisive role of solvated ions on the conformational transition and stability. Because amyloidogenic behavior seems to be a generic feature common to diverse peptides, the trigger of structure formation should be studied in more detail, for example by means of specific sequence mutations. This would give us new insights into the intramolecular patterns which favour this exceptional conformation.

We also stressed the critical effect of non-ionic cosolvents on interfacial adhesion in chapter 7. Cosolvent related effects, and ion-specific effects in particular, are also expected to manifest themselves, by changing transition rates, equilibrium constants, and in reactions accompanying major conformational changes of proteins [100]. These mechanisms have to be further analyzed to provide a profound understanding of biological processes such as enzyme catalysis or substrate binding. Knowledge of the energetics of protein stability in the vicinity of other macromolecules and interfaces will be the key to understand their structure-function relationship. On a long-term basis, it will also help to design nano-mechanical devices and molecular machines based on protein chemistry, which ultimately have to be connected to a surface in order to link them to the macroscopic environment.

The investigation of more surfaces with diverse characteristics, e.g. SAMs, lipid bilayers or the cell membrane in case of amyloidogenic peptides, in the presence of different kinds of kosmotropes and chaotropes will help to understand complex phenomena such as the Hofmeister effect in biology. Moreover one might extend research to liquid/liquid or liquid/gas interfaces and compare the results to MD-simulations.

Because of friction forming the basis of many technical processes, its investigation should be expanded to the molecular scale [318,319]. However, the friction contribution to the desorption force is hard to identify from experiments where the polymer is moved vertically away from the surface, since desorption forces and friction forces are mixed together. Friction is more directly studied by lateral pulling and comparison to respective MD-simulations [141,320].

The influence of the polymer composition on the adsorption/desorption behavior on the other hand could be probed in more detail by the use of multiblock copolymers that alternately comprise hydrophobic and hydrophilic blocks. Depending on the block length one should be able to identify the influence of a particular chemical species on the hydrophobic attraction by a characteristic plateau pattern.

Similarly, once the occurrence of the additional patterns on top of the desorption plateaus of ligand/carrier conjugates (see Appendix C) is understood and how these are related to the number of conjugated small molecules, we can then investigate the interactions of these small molecules as well. In this way, drugs, markers or transcription factors will soon become the prime target for single molecule studies in pharmaceutical and medical research.

Appendix A

Inherent Limitations to AFM Force Resolution

The frequency dependent oscillation amplitude A(ν) of a cantilever in liquid is best described by a damped harmonic oscillator:

$$A(\nu) = A^0 \frac{\nu_0^2}{\sqrt{(\nu_0^2 - \nu^2)^2 + \frac{\nu_0^2 \nu^2}{Q}}} \qquad (A.1)$$

where A^0 is the amplitude at zero frequency, ν_0 is the resonance frequency and Q is the quality factor. The resulting mean square displacement $\langle \Delta z^2 \rangle$ of the cantilever (Brownian motion) due to thermal excitation is inversely proportional to the cantilevers spring constant k and direct proportional to the thermal energy $k_B T$. This is expressed by the equipartition theorem [321]:

$$k\langle \Delta z^2 \rangle = \chi \cdot k_B T \qquad (A.2)$$

With χ being a correction factor that accounts for the cantilever geometry; for rectangular cantilevers $\chi \approx 0.82$, and for triangular cantilevers $\chi \approx 0.76$ [322,323]. But χ also depends on the position and the size of the laser spot [323,324]. Typical values of the standard deviation of the mean square displacement for AFM cantilevers also used in this study (k ≈ 20 pN/nm) are $\sqrt{\langle \Delta z^2 \rangle} \approx 0.4nm$ and hence for the force noise $\sqrt{\langle F^2 \rangle} \approx 8pN$.

Viani et al. showed that the minimal detectable force for a frequency bandwidth B and a damping coefficient γ is given by:

$$F_{\min} = \sqrt{4k_B T \gamma B} \qquad (A.3)$$

For constant temperature an increase in force resolution can only be achieved by reducing the damping γ. One possibility to accomplish that is the use of smaller cantilevers and the optimization of the lever geometry [325]. However for a complete discussion of the resolution limits the detector noise (D_N) has to be taken into account as well. In case of a periodical force signal F(ν) we get for the signal-to-noise ratio [325,326]:

$$\frac{S}{N} = \frac{F(\nu)G(\nu)}{\sqrt{4k_B T \gamma B G^2(\nu) + (k \cdot D_N)}} \qquad (A.4)$$

Obviously, the signal-to-noise ratio becomes worse if stiffer cantilevers are used. That is the reason why longer and softer cantilevers are preferred in SMFS (see Materials and Methods section).

Appendix B

Direct Comparison of Different Polymers

The use of long flexible molecules averages out all subtle differences in the adsorption free energy that might be related to the differences between the monomer units or the amino acid sequence. The effect of different amino acids on the desorption force observed in MD-simulations (see figure 1.9.2) could not be resolved in our SMFS measurements. One can try to detect the influence of polymer composition and the role of the particular type of amino acid on the hydrophobic attraction in terms of adsorption free energies by using homopolymers as molecular probes the monomer units of which differ in charge, polarity, and the overall degree of hydrophobicity.

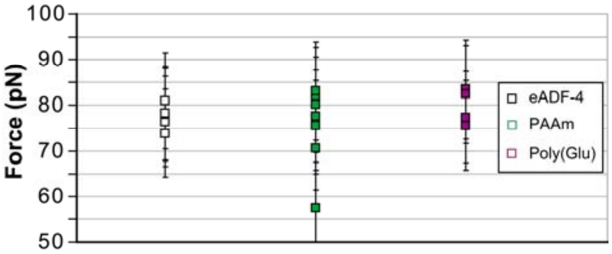

Figure B.1: SMFS with different sensor molecules to evaluate the effect of polymer composition on the desorption forces.

However, the use of different polymers attached to different cantilevers suffer from the uncertainty of cantilever calibration masking small changes related to polymer-substrate interactions. As one can see from figure B.1, the differences between positively charged PAAm, negatively charged poly(glutamic acid) and the mildly hydrophobic eADF-4 are not resolved even if several experiments are carried out and averaged. One has to perform much more experiments in order to improve statistics, so that the differences become visible. A better solution to this problem comprises polymer architecture. If block co-polymers are designed that contain multiple blocks of different characteristics, we could trace the effect of polymer composition within one curve recorded with one and the same molecule in only a single experiment. In this way we would be independent from the absolute error caused by spring constant determination.

Appendix C

Enhanced Molecular Sensor for Force Spectroscopy with Small Molecules

Single molecule force spectroscopy under equilibrium conditions could only be performed with long, flexible polymers so far and was not applicable to small molecules such as drugs or markers. In medical technology the adhesion of small bioactive agents gains increasing importance and quantifying tools have been scarce as described in the introduction. In the following we will present our results of extended molecular sensors, which use PAAm as carrier molecule for the covalent attachment of small molecules. The adhesion of these small molecules will be probed by a characteristic change of the desorption plateau.

The conjugation of smaller molecules (see Materials and Methods section) such as anti-freeze protein (AFP) type I to PAAm as carrier molecule exhibited always the same features in the force separation curves: a second plateau on top of the PAAm plateau.

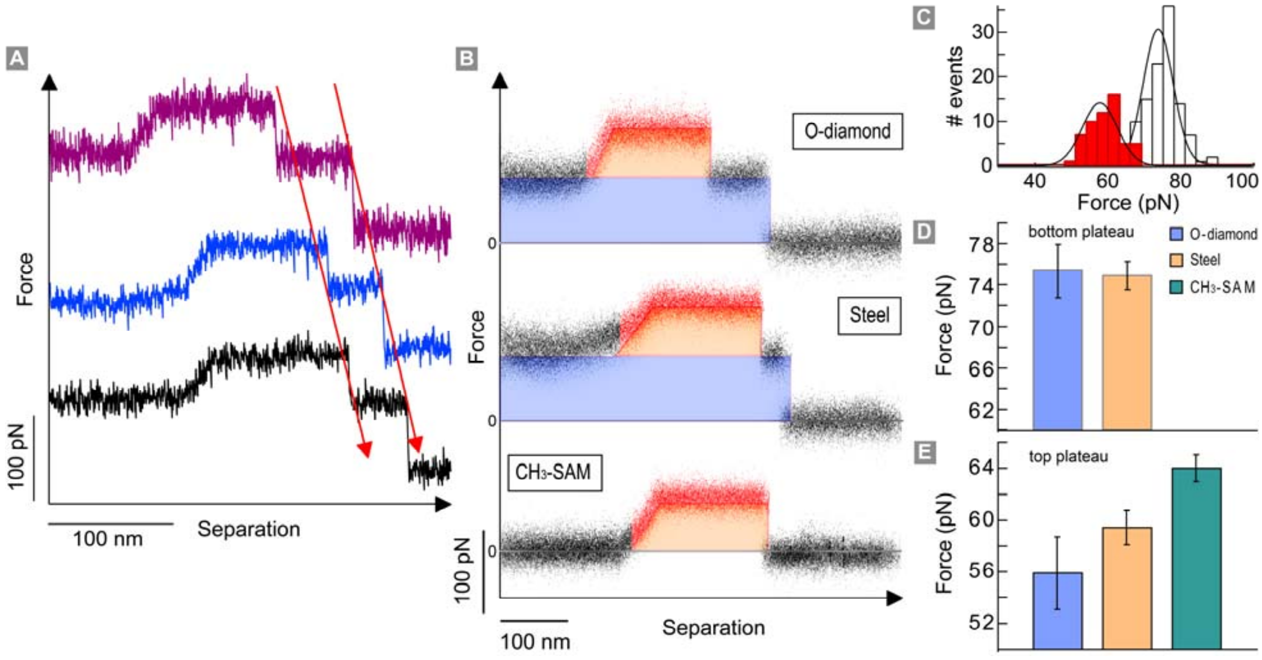

Figure C.1: SMFS on PAAm-AFP conjugates on different substrate materials. (A) The top structure of the force-separation curves related to the amount of AFP bound to the PAAm carrier molecule exhibits a constant position relative to the free end of PAAm. (B) Superposition of 20 force-separation traces on different substrates. The pattern is seen in every curve that also shows the PAAm carrier. (C) The force distribution shows significant smaller desorption forces. (D) The force values on three different substrate materials for PAAm is different from that of the plateaus related to AFP (E).

The location of this second plateau had a constant position relative to the detachment length and hence to the free end of the PAAm molecule (figure C.1 (A)). This observation of the additional plateau not being randomly distributed along the carrier plateau but instead having a constant position along its contour indicates that former explanations of similar features like that of differential adsorption onto the tip surface do not apply here. In the latter case one would expect a more randomly distributed position as well as lengths of the second plateau.

Differential adsorption can not be made responsible for the occurrence of the additional plateaus for another reason, as we will discuss in the following. In the experiments by Sonnenberg et al. the reported differential adsorption was verified using a cantilever that picked up a molecule covalently attached to the substrate surface and not to the cantilever tip. When the cantilever was retracted the polymer desorbed not only from the substrate but also from the cantilever tip surface where it had also been partially adsorbed. The resulting force-separation traces revealed a second plateau at the end of the first one due to the higher adsorption free energy of those parts of the molecule being adsorbed onto the tip. However, in our case the sensor molecule is covalently bound to the tip, thus a stronger adsorption of the sensor molecule to the tip compared to the adsorption to the substrate would result only in a shortening of the detachment length, but would not produce a different force signal. Whereas a weaker adsorption to the tip surface would produce a lower plateau level right at the beginning of the force-separation trace, because the weakly adsorbed part will be desorbed first. So, even if our traces have comparable appearance to those in ref. [327], their origin can not be the same.

Moreover, the comparison of the primary plateau of PAAm and the secondary plateau on different substrate materials (figure C.1 (B)) reveals a remarkably different behavior. The different desorption forces are determined from force distributions (figure C.1 (C)) which are shifted for both kinds of plateaus. The mean force values obtained on oxidized diamond, stainless steel and a hydrophobic SAM are depicted for the PAAm carrier in figure C.1 (D) and for the AFP related plateaus in figure C.1 (E). All measurements were performed with one and the same sensor molecule. The most interesting difference is seen on the CH_3-SAM where the PAAm force plateau is not observed any more, but the shorter plateau related to the conjugated AFP is still clearly visible.

To further investigate the relation between the structure of the force plateaus and the amount of conjugated AFP molecules we reduced the concentration of AFP during the chemical synthesis of the PAAm/AFP construct to about 10 %, which resulted in a significant shortening of the secondary plateau to about 40% of its original length (figure C.2).

We also coupled fluorescent dyes, here PromoFluor 555 (PF-555), to the PAAm molecule and performed SMFS measurements on diamond substrates with different termination (figure C.3). Again the force-separation curves showed secondary plateaus on top of the PAAm plateau.

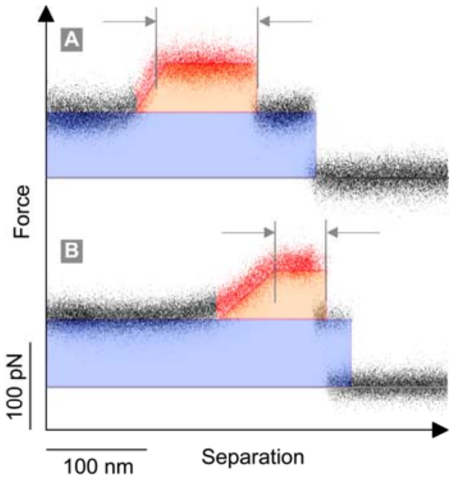

Figure C.2: Variation of AFP concentration during conjugation. The concentration of the AFP molecules in the coupling reaction with PAAm resulting in the force curve appearance in (A) was reduced to 10% in (B). The figure shows the superposition of 20 subsequent force curves in each case.

This time we observed two different locations where the coupling of small dye molecules led to an increase of the desorption force. Again the variation of the desorption forces and the free energies were different for the PAAm plateau (figure C.3 (B)) and the structures on top (figure C.3 (C)).

This kind of plateau structure has also been observed in experiments with only PAAm without conjugates in aqueous electrolyte solution at high salt concentration. One explanation could be that surfactant molecules in solution were bound to the PAAm molecule in the course of the measurement and formed a stable linkage.

The increase of the desorption force of roughly 80% in line with previous experiments on multiple polymer desorption hints at a second possible explanation. The attachment of a hydrophobic molecule such as AFP or a fluorophore to the polymer chain might result in looping and the formation of a stable connection between those monomers that have reacted with a conjugate due to the hydrophobic attraction in case of AFP or PF-555 or due to electrostatic forces in case of high ion concentration. This would lead to desorption of multiple polymer strands in parallel upon cantilever retraction. However the different behavior on the various substrate materials still remains unexplained and strongly demands further experiments to clarify the origin of the plateau structures.

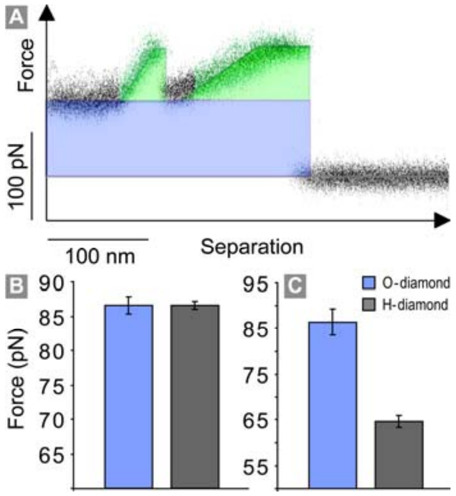

Figure C.3: SMFS with fluorescent dye molecules bound to a PAAm carrier molecule. (A) The conjugation of PF-555-fluorophores resulted in additional plateau structures on top of the PAAm desorption plateau. 20 consecutive force curves with the same sensor molecule are shown. (B) Desorption forces of PAAm on oxidized and hydrogenated diamond differ from that of the fluorophores (C) with regard to the sensitivity on material properties.

Appendix D

Materials and Methods

D.1 Substrate preparation

Hydrogenated and oxidized polycrystalline diamond

Modified diamond samples used in this study were provided by courtesy of Simon Q. Lud, Moritz Hauf and José A. Garrido from the Walter-Schottky Institute (WSI) of the TUM. Hydrogenation of polished polycrystalline diamond surfaces (ElementSix Advancing Diamond Ltd., UK) was conducted as described elsewhere.[218] The samples were heated in a vacuum chamber to a temperature of 700 °C at a pressure of $5 \cdot 10^{-7}$ mbar. The hot sample surface was exposed to hydrogen radicals generated by two 2000 °C hot tungsten filaments for 30 minutes at a constant pressure of 1.5 mbar, and cooled in hydrogen atmosphere. The H-terminated diamond surfaces were hydrophobic with contact angles between 80° and 90°. The specimens were wiped clean followed by ultrasonic cleaning in acetone, 2-propanol and water before measurements.

Oxidation was conducted by exposure to oxygen plasma at a base pressure of 1.5 mbar for 300 s (coil power 300 W) and resulted in hydrophilic surfaces (C-O). Patterned surfaces with alternating hydrogen and oxygen terminated surface regions were processed by spin-coating of a positive photoresist (Microposit S1818, Rohm & Haas GmbH, Germany) onto a H-terminated diamond surface (9000 rpm, 30s). The samples were heated for 10 min at 90 °C in an oven and exposed to UV light (365 nm) for 6 s through a patterned photomask in close contact with the sample surface to reduce diffraction. A maskaligner (MJB 3, Karl Süss GmBH, Germany) allowed a precise positioning of the mask relative to the specimen. After removal of the illuminated areas (Microposit Dev 351, dilution 1:5, Rohm & Haas GmbH) the samples were rinsed with ddH_2O and were O-terminated as described above. Finally, residues of the photomask were removed with acetone in an ultrasonic bath.

Figure D.1.1: Hydrogenated polycrystalline diamond coated with checkerboard-like photoresist. After removal of the illuminated areas (bright spots) these spots were oxidized.

Surgical stainless steel (316L)

Circular flat blanks were jet cut from a metal sheet of stainless steel 316L of 1mm thickness (Max Cochius GmbH) and dressed to a size of 10 mm diameter (figure D.1.2). To achieve a reduced roughness in the nanometer regime, we ground the samples with a wet silicon carbide grinding wheel for

2 minutes at 300 rpm with a constant force of 2 N, and polished them in several steps at 150 rpm for 2 minutes with a final polish grain size of 40 nm. In-between the grinding steps the samples were cleaned in an ultrasonic bath for 5 minutes in de-ionized water to avoid particle transfer from one polish to the other. Specimens with rough surfaces were obtained by a sandblasting treatment according to the manufacturing process of the PEARL-surface of the YUKON^{DES} stent (Translumina GmbH, Hechingen, Germany).

Figure D.1.2: Polished and sandblasted surgical stainless steel blanks.

Poly(tetrafluorethylene) (PTFE)

Samples of 1.5 mm thickness were purchased from GM GmbH, Munich, Germany and cut into squares of 5 mm edge size.

Self assembled monolayers (SAM)

Glass slides were cleaned for 15 minutes in an ultrasonic bath in 2 % Hellmanex solution (Hellma GmbH & Co. KG, Mühlheim, Germany) and ultrapure water (Molecular Biology Reagent, Sigma Aldrich, Schnelldorf, Germany). After drying in air, the glass slides were sputter coated (Edwards GmbH, Kirchheim, Germany) with a 10 nm layer of chrome and nickel as adhesion promoter, followed by a 100 nm gold layer. The gold slides were cleaned in a solution of water, 32 % ammonia, 35 % hydrogen peroxide (v:v:v 5:1:1) at 70 °C for 15 minutes, rinsed with ultrapure water, and dried under a gentle stream of nitrogen. SAMs of defined hydrophobicity were obtained by immersing the gold coated slides for 12 hours in 2 mM mixtures of varying ratio of 11-mercapto-1-undecanol (97%, Sigma Aldrich, Germany) and 1-dodecanethiol (98+%, Sigma Aldrich, Germany) in chloroform (99+%, Neolab, Heidelberg, Germany). The SAMs were rinsed with chloroform and then with ultrapure water. The slides were dried under a gentle stream of nitrogen, and directly used for measurement.

The samples (except SAMs) were stored in a cleaned glass petri dish in a desiccator under vacuum unless transferred into salt solution for SMFS experiments for some hours. Before and after measurements in liquid the samples were cleaned in an ultrasonic bath as described above, dried under a gentle stream of nitrogen and put back into vacuum. To confirm the degradation process the samples were also cleaned mechanically by rubbing forcefully over the surface several times with a fuzz-free acetone-soaked wipe wrapping a spatula.

D.3 Homopolymers for SMFS

Poly(allylamine) hydrochloride (PAAm) (molecular weight 65 kDa and 17 kDa, 20 % w/v aqueous solution), poly-L-(glutamic acid) (50 – 100 kDa) and poly(lysine) (15-150 kDa) were purchased from Sigma-Aldrich, Germany.

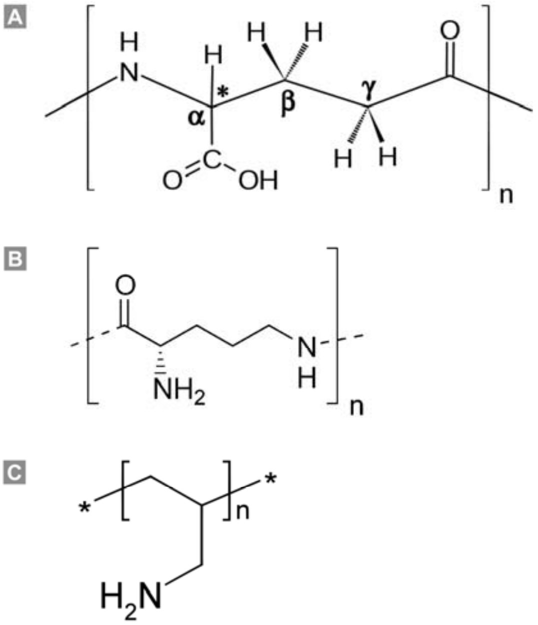

Figure D.3.1: Structural formulae of homopolymers. (A) Poly(glutamic acid, (B) Poly(lysine); (C) Poly(allylamine).

D.2 Production of recombinant proteins eADF-3 and eADF-4.

Protein samples of eADF-3 and eADf-4 were kindly provided by Ute Slotta and Thomas Scheibel from the University of Bayreuth. Gene constructs for eADF-4 (C16) and eADF-3 ((QAQ)$_8$NR3) were cloned as described previously[177,229]. (QAQ)$_8$NR3 comprises the A- and Q-motifs derived from ADF-3 (Araneus diadematus fibroin) and C$_{16}$ the C-motif derived from ADF-4:

A-motif:
GPYGPGASAAAAAAGGYGPGSGQQ

Q-motif:

GPGQQGPGQQGPGQQGPGQQ

C-motif:
GSSAAAAAAAASGPGGQGPENQGPSGP GQGPGGP

All sequences are derived from the repetitive core domain of the respective spider silk protein. The motifs are synthetically adapted to the codon usage of Escherichia coli. Each construct was finally cloned into the expression vector pET21a (Novagen).

E. coli BLR(DE3) (Novagen) cells were transformed with the resulting plasmids and grown in LB medium with 100 µg/ml ampicillin at 37 °C until OD$_{600}$ of 0.5 was reached[328]. Cells were shifted to 30 °C in case of eADF-3 and 25 °C in case of eADF-4 before induction with 1 mM isopropyl β-D-galactopyranoside (IPTG) for 3 h. E. coli cells were harvested after induction for 3-4 hours, and the cell pellets were resuspended in 20 mM HEPES, 100 mM NaCl, pH 7.5 (5 mL per g of cells). Upon addition of 0.2 mg Lysozyme (Sigma-Aldrich) per mL, the resuspension was incubated at 4 °C for 30 min until becoming viscous. Protease inhibitor (Serva) was added before the cells were ultrasonicated using an HD/UW2200/KE76 ultrasonicator (Bandelin). Contaminating DNA was digested upon addition of 10 µg/mL DNase and 3 mM MgCl$_2$ and (protease-free DNAse was obtained from Roche) and incubation at 4 °C for 30 min.

Upon sedimentation at 50000 x g and 4 °C for 30 min, remaining soluble proteins were incubated at 80 °C for 20 min. A further centrifugation step was performed and eADF-4 or eADF-3 were found in the supernatant. Upon addition of 20 % ammonium sulphate the recombinant spider silk proteins precipitated. The eADF-3 pellets were rinsed with the ammonium sulphate, whereas eADF-4 pellets were washed with 8 M urea. Both proteins were resuspended in 6 M guanidinium thiocyanante and dialysed against 10 mM ammonium hydrogencarbonate at 4 °C. Finally, proteins were lyophilised and stored at -20 °C until usage.

D.4 Covalent coupling of type I antifreeze protein (AFP) and PF-555 to PAAm

Conjugated PAAm/AFP samples were supplied by Nolan B. Holland from Cleveland State University. Synthesis and purification of type I antifreeze protein (AFP) is described elsewhere [329]. All carboxyl groups except the C-terminal end of AFP were removed. Water soluble 1-ethyl-3-(3-dimethylaminopropyl) carbodiimide hydrochloride (EDC) was used to form an active ester functional group with the carboxyl group using the water-soluble compound N-Hydroxysuccinimide (NHS) (Invitrogen). NHS esters are hydrophilic active groups that react rapidly with amines on the target molecule [330], here PAAm. Similarly, fluorescent dyes, PromoFluor-555 NHS ester (PF-555, PromoCell) were covalently reacted with PAA for single molecule force spectroscopy in DMSO.

D.5 Native PAGE gel electrophoresis

To confirm the reaction of AFP and PF-555 with PAAm, we performed an inverted gel electrophoresis and used different poly(Lys) samples of known molecular weight range as marker. The samples were kept close to 0 °C prior to adding the sample buffer. The sample buffer composed of 0.5 ml acetate-KOH (0.25M, pH 6.8) and 1.45 ml glycerol (50%) also contained a small amount of methyl green to visualize the sample during the run. The gels were cast according to table D.5.1. Prior to adding APS and TEMED, the gel solutions were degassed in an ultrasonic bath for 5 minutes. The gels were allowed to polymerize for at least one hour. We rinsed the surface of the gel with water before pouring the stacking gel. After insertion of a 10 well comb we let the stacking gel polymerize again for one hour. The wells were filled with 15 µl of sample volume. A good sample concentration was 0.3 µg/ml, i.e. up to 5µg per well (figure D.5.1). Due to the positive charges of the PAAm and poly(Lys) samples at acidic pH (most of the amine groups will be protonated) we reversed the polarity of the leads to the gel chamber. We determined 50 mA; 21V to collect the sample and 100 mA; 32 V for 8 hours as the best running conditions for this kind of reversed native PAGE. Afterwards the gels were stained with Coomasie Blue stain (Bio-Rad), washed with water several times and stored in destaining solution (Bio-Rad) in presence of a sponge.

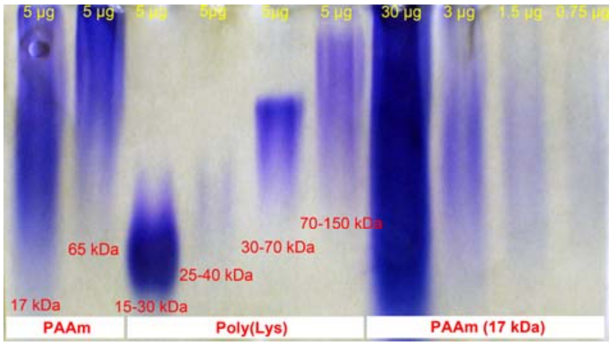

Figure D.5.1: Coomassie blue staining of PAAm (65 kDa and 17 kDa) and poly(Lys) separated by using inverted native PAGE.

After the reaction with AFP or PF-555 the PAAm sample did not run any more under the same conditions, which indicated the successful coupling of the small molecules to

Table D.5.1: Gel Composition for reversed native PAGE.

	Total volume (ml)	Composition	Volume fraction (ml)
Separation gel (10%) 4 ml per gel	25.8	Acetate-KOH (1.5M, pH 4.3) Glycerol 50 % Acrylamide/Methylene-bis-Acrylamide 30 % Water Tetramethylethylenediamine (TEMED) Ammonium persulfate (APS) 10%	6.7 6.0 8.8 4.2 0.012 0.09
Stacking gel (5%) 1 ml per gel	15.1	Acetate-KOH (0.25M, pH 6.8) Acrylamide/Methylene-bis-Acrylamide 30 % Water Tetramethylethylenediamine (TEMED) Ammonium persulfate (APS) 10%	4.0 2.5 8.6 0.001 0.01

the PAAm polymer by the loss of positive charge. Note that the PAAm samples (17 kDa and 65 kDa) were both highly disperse with molecular weights much bigger than the expected range according to the manufacturer data.

D.6 Cantilever tip preparation

Silicon nitride cantilevers (MLCT-AUHW, Veeco) were cleaned and activated by oxygen plasma treatment (Diener electronic). For this purpose, the cantilevers were placed in an evacuated reaction chamber at 0.05 mbar for half an hour. Oxygen was added up to a constant pressure of 0.1 mbar. The process was controlled by two parameters: the electric power at 40 kHz and plasma exposure time. Plasma treatment was performed in two steps. First the cantilevers were exposed to plasma for 5 minutes at 600 W, followed by treatment for 20 minutes at 420 W. The activated cantilevers were transferred immediately to a solution of 50 µl Vectabond reagent (Axxora) in 2 ml dry acetone (< 50 ppm H2O, Acros organics) for 10 minutes. The cantilevers were rinsed afterwards with Aceton and ultrapure water (Molecular biology reagent, Sigma Aldrich) and stored for 1.5 h in an aqueous solution (50 mM) of di-sodium tetraborate (> 99.5 %, Merck) at pH 8.5. After rinsing with dry chlorophorm (> 99.9 %, Biotech grade, Sigma-Aldrich), the cantilever tips were placed for 45 minutes in a solution (25 mM) of poly(ethylene glycoles), (monofunctional α-methoxy-ω-NHS PEG and heterobifunctional α,ω-di-NHS PEG, 2 kDa, Rapp Polymere GmbH), dissolved in dry chlorophorm with 5 % triethylamine (Thermo Fisher Scientific), subsequently rinsed with chlorophorm and dimethyl sulfoxide (DMSO, > 99.5 %, Sigma Aldrich), and placed in polymer solution (0.1 % w/v PAAm; or 2 mg/ml protein solution) in DMSO over night. The PEG not only prevents the free end of the PAAm molecule from being adsorbed at the tip surface but also reduces the undesired, unspecific adhesion between tip and substrate significantly[130]. After approximately 14 hours the cantilever were rinsed with DMSO, 10 mM aqueous Tris/HCl solution (pH 8.0) (> 99.9 %, neoLab) and ultrapure water directly before force spectroscopy measurements. All measurements were performed with a MFP-3D (Asylum research, Santa Barbara, CA) equipped with Bioheater stage. Glucose (monohydrate, > 99.5 %, *BioUltra*) was purchased from neoLab and dissolved in ultrapure water.

Alternatively, the reaction with PEG (PEGylation) and the following coupling of the polymer can also be done in aqueous buffer solutions at pH between 8 and 9. We successfully attached individual polymers to the AFM tip by immersing the cantilever in an aqueous solution of PEG (25 mM) in sodium borate buffer (50mM) at pH 8.5 for 35 minutes, followed by rinsing the cantilever in unltrapure water and transfer into polymer solution in sodium borate buffer. The use of aqueous solution promotes hydrolysis of the active ester and needs sorrow time management and fast handling which is difficult to control properly and resulted in a moderate extent of functionalized cantilevers.

A third approach for amino termination for subsequent PEGylation developed by Hinterdorfer and co-workers uses a saturated solution of ethanolamine hydrochloride (Sigma-Aldrich) in DMSO in which the cantilevers are stored slightly above room temperature over night. This ensures the formation of only a monolayer of amino terminated molecules on the tip surface and avoids possible polymerization of silanes. However, in our experiments the high viscosity of the solution and precipitation often caused permanent bending of the cantilevers which made them useless for our SMFS experiments

D.7 Cantilever calibration and error analysis in SMFS

We averaged the inverted optical lever sensitivity (invOLS) of the first five as well as the last five force-separation traces, and used it for the whole experiment until either the solution or the cantilever changed. The spring constant of each cantilever was determined prior to each experiment. We measured the spring constant by integrating over the power spectral density of the MFP-3D (which is already corrected for the χ-factor) from 75 Hz to the local minimum between the first and the second resonance peak, and by applying the equipartition theorem.[S3]

For each SMFS experiment in this study, 500 to 1000 approach-retract cycles were recorded and analyzed as described in the main text. The corresponding standard deviations were calculated according to the theory of small samples. The resulting uncertainties given in the tables and figures thus only account for the relative error of the measurements when one and the same cantilever was used. For comparison of different cantilevers and different probe molecules, respectively (e.g. eADF-4 and PAAm), an absolute error of 13% has to be considered instead, as the main uncertainty of the absolute force values stems from cantilever calibration.

D.8 Error estimate of cosolute binding parameters

To determine the uncertainty of a single fit parameter, we varied this parameter in discrete steps and kept it constant during the fitting procedure while all other parameters had to adjust for this change. As long as the resulting fit still represented the experimental data within the force error bars, the change of the fit parameter, namely the association rate constants and the distances between binding sites, was still within its uncertainty. When the changes could not be compensated for any more these values were considered inappropriate and the variations were beyond the parameter's uncertainty.

D.9 Contact angle measurements

Static contact angles of water, glycerol and diiodomethane were obtained at room temperature by dispensing 1.5 µl of liquid on the sample surfaces. Pictures were taken immediately after droplet formation and subsequently analyzed by the Java-based freeware ImageJ with drop analysis plugin[331]. [24] Both contact angles of a droplet were determined at least five times at different positions of each sample. All specimens were cleaned by sonification in acetone and 2-propanol before each measurement.

D.10 Scanning Electron Microscopy (SEM)

Images of specimens made of surgical stainless steel were acquired by the analysis of the reflected secondary electron beam in a Hitachi S 3500-N scanning electron microscope (SEM) equipped with energy-dispersive X-ray (EDX) analyzing unit. The SEM was operated at an acceleration voltage of 15 keV. Sputter coating of the samples with gold was not necessary due to the good conductivity of the metal surface. Photographs were taken at representative areas of the polished and microporous steel surfaces to document the roughening effect of the surface treatment.

D.11 Atomic Force Microscopy (AFM)

For atomic force microscopy (AFM) we used a Molecular Force Probe 3D (MFP-3D, Asylum Research, Santa Barbara, CA) and triangular silicon nitride cantilevers with a nominal spring constant of ~ 2 N/m and a resonance frequency of ~ 70 kHz (AC240TS, Olympus, Japan). The sample surfaces were imaged by AFM in intermittent contact mode (AC mode) at ambient temperatures in air. The imaging set point was chosen so that the forces acting on the cantilever during imaging were repulsive (beyond the attractive regime). In the case of polished polycrystalline diamond, images were taken in contact mode at a scan rate of 0.6 Hz with appropriate cantilevers (OMCL-RC800PSA, Olympus, Japan). Image resolution was set to 512 x 512 data points. The roughness of the different materials was calculated from 50 µm x 50 µm sized surface sections, and values for the root mean square (RMS) roughness (R_q) were derived from the AFM height image data.

D.12 Kelvin Probe force microscopy (KPFM)

To confirm the appropriate termination of the diamond surfaces with oxygen and hydrogen atoms, respectively, we performed KPFM using a MFP-3D and platinum coated silicon nitride tips (AC240TM, Olympus, Japan) with a typical spring constant of ~ 2 N/m and a resonance frequency in air of ~ 72 kHz. The acquired potential image represents a combination of three different contributions: any permanent voltage between probe tip and substrate surface, trapped charge and the work function difference [332]. That's why this technique is generally considered a semi-quantitative method, but if the resistivity of all participating components remains constant the measured potential difference can be related to the surface properties [333]. To testify the chemical homogeneity of the different terminations on diamond we grounded the conductive H-terminated area of the specimen and measured with one and the same tip on a patterned sample consisting of C-H and C-O termination.

Surface potential imaging was conducted under ambient conditions and utilized lift mode scanning with two scans per line [333]. The first scan was performed in intermittent contact mode with zero bias voltage applied to the cantilever to obtain a topography image of the surface; the second scan followed the topographic scan at a lift height of 30 nm with an AC drive voltage of 1 V applied to the tip. In the event of a contact potential difference of the probe tip with respect to the sample surface, the probe will oscillate in this field driven by the AC voltage due to electrostatic force. The oscillation is balanced to zero by applying an additional DC voltage on the cantilever and adjusting it to the contact potential difference such that the space between tip and surface becomes field-free. However, the obtained potential image represents a combination of three different contributions: any permanent voltage between probe tip and sample surface, trapped charge, and the work function difference. For this reason, this method is generally considered to be a semi-quantitative technique [243]. If the resistivity of all of the participating components remains constant, the recorded potential profile can be attributed to the surface properties [334,335].

Bibliography

1. Ashbaugh, H.S. and Pratt, L.R. (2006) Colloquium: Scaled particle theory and the length scales of hydrophobicity. *Reviews of Modern Physics* 78: 159-178.
2. Yaminsky, V.V. and Vogler, E.A. (2001) Hydrophobic hydration. *Current Opinion in Colloid & Interface Science* 6: 342-349.
3. Tilden, W.A. ed., *Introduction to the study of chemical philosophy: the principles of theoretical and systematic chemistry*, 10th ed. (Longmans, Green, and Company, New York, 1901).
4. Gristina, A.G. (1987) Biomaterial-centered infection: Microbial adhesion versus tissue integration. *Science* 237: 1588-1595.
5. Hench, L.L. (2002) Third-generation biomedical materials. *Science* 295: 1014-1017.
6. Thakar, R.G. *et al.* (2008) Contractility-dependent modulation of cell proliferation and adhesion by microscale topographical cues. *Small* 4: 1416-1424.
7. Khang, D. *et al.* (2008) The role of nanometer and sub-micron surface features on vascular and bone cell adhesion on titanium. *Biomaterials* 29: 970-983.
8. Stickler, D.J. (2008) Bacterial biofilms in patients with indwelling urinary catheters. *Nature Clinical Practice Urology* 5: 598-608.
9. Hall-Stoodley, L., Costerton, J.W., and Stoodley, P. (2004) Bacterial biofilms: From the natural environment to infectious diseases. *Nature Reviews Microbiology* 2: 95-108.
10. Götz, F. (2002) Staphylococcus anf biofilms. *Molecular Microbiology* 43: 1367-1378.
11. Costerton, J.W. *et al.* (1987) Bacterial Biofilms in Nature and Disease. *Annual Review of Microbiology* 41: 435-464.
12. Matl, F.D. *et al.* (2008) New anti-infective coatings of medical implants. *Antimicrobial Agents and Chemotherapy* 52: 1957-1963.
13. Lowe, H.C. and Khachigian, L.M. (2002) Coating stents with antirestenotic drugs: The blunderbuss or the magic bullet? *Circulation* 105: E29-E29.
14. Bechert, T., Steinrücke, P., and Guggenbichler, J.P. (2000) A new method for screening anti-infective biomaterials. *Nature Medicine* 6: 1053-1056.
15. Lu, X. *et al.* (2007) Spectroscopic analysis of titanium surface functional groups under various surface modification and their behaviors *in vitro* and *in vivo*. *Journal of Biomedical Materials Research* 84A: 523-534.
16. Sun, T. *et al.* (2005) No platelets can adhere-Largely improved blood compatibility on nanostructured superhydrophobic surfaces. *Small* 1: 959-963.
17. Benhabbour, S.R., Sheardown, H., and Adronov, A. (2008) Cell adhesion and proliferation on hydrophilic dendritically modified surfaces. *Biomaterials* 29: 4177-4186.
18. Moreira, L.A. *et al.* (2007) Effect of the ion-protein dispersion interactions on the protein-surface and protein-protein interactions. *Journal of the Brazilian Chemical Society* 18: 223-230.
19. Blokzijl, W. and Engberts, J. (1993) Hydrophobic Effects - Opinions and Facts. *Angewandte Chemie-International Edition* 32: 1545-1579.
20. Murphy, K.P., Privalov, P.L., and Gill, S.J. (1990) Common Features of Protein Unfolding and Dissolution of Hydrophobic Compounds. *Science* 247: 559-561.

21. Butler, J.A.V. (1937) The energy and entropy of hydration of organic compounds. *Transactions of the Faraday Society* 33: 0229-0236.
22. Frank, H.S. and Evans, M.W. (1945) Free Volume and Entropy in Condensed Systems .3. Entropy in Binary Liquid Mixtures - Partial Molal Entropy in Dilute Solutions - Structure and Thermodynamics in Aqueous Electrolytes. *Journal of Chemical Physics* 13: 507-532.
23. Klotz, I.M. (1958) Protein Hydration and Behavior. *Science* 128: 815-822.
24. Kauzmann, W. (1959) Some Factors in the Interpretation of Protein Denaturation. *Advances in Protein Chemistry* 14: 1-63.
25. Nemethy, G. and Scheraga, H.A. (1962) Structure of Water and Hydrophobic Bonding in Proteins .1. A Model for Thermodynamic Properties of Liquid Water. *Journal of Chemical Physics* 36: 3382-&.
26. Nemethy, G. and Scheraga, H.A. (1962) Structure of Water and Hydrophobic Bonding in Proteins .2. Model for Thermodynamic Properties of Aqueous Solutions of Hydrocarbons. *Journal of Chemical Physics* 36: 3401-&.
27. Nemethy, G. and Scheraga, H.A. (1962) Structure of Water and Hydrophobic Bonding in Proteins .3. Thermodynamic Properties of Hydrophobic Bonds in Proteins. *Journal of Physical Chemistry* 66: 1773-&.
28. Tanford, C. (1962) Contribution of Hydrophobic Interactions to Stability of Globular Conformation of Proteins. *Journal of the American Chemical Society* 84: 4240-&.
29. Buff, F.P. and Kirkwood, J.G. (1951) Solutions of Nonelectrolytes. *Annual Review of Physical Chemistry* 2: 51-66.
30. Meyer, E.E., Rosenberg, K.J., and Israelachvili, J. (2006) Recent progress in understanding hydrophobic interactions. *Proceedings of the National Academy of Sciences of the United States of America* 103: 15739-15746.
31. Chandler, D. (2005) Interfaces and the driving force of hydrophobic assembly. *Nature* 437: 640-647.
32. Tanford, C. (1997) How protein chemists learned about the hydrophobic factor. *Protein Science* 6: 1358-1366.
33. Huang, D.M. and Chandler, D. (2000) Temperature and length scale dependence of hydrophobic effects and their possible implications for protein folding. *Proceedings of the National Academy of Sciences of the United States of America* 97: 8324-8327.
34. Lum, K., Chandler, D., and Weeks, J.D. (1999) Hydrophobicity at small and large length scales. *Journal of Physical Chemistry B* 103: 4570-4577.
35. Stillinger, F.H. (1973) Structure in Aqueous Solutions of Nonpolar Solutes from the Standpoint of Scaled-Particle Theory. *Journal of Solution Chemistry* 2: 141-158.
36. Krishnan, A. *et al.* (2005) An evaluation of methods for contact angle measurement. *Colloids and Surfaces B-Biointerfaces* 43: 95-98.
37. Poynor, A. *et al.* (2006) How water meets a hydrophobic surface. *Physical Review Letters* 97.
38. Mezger, M. *et al.* (2006) High-resolution in situ x-ray study of the hydrophobic gap at the water-octadecyl-trichlorosilane interface. *Proceedings of the National Academy of Sciences of the United States of America* 103: 18401-18404.
39. Chandler, D. (2007) Physical chemistry - Oil on troubled waters. *Nature* 445: 831-832.

40. Maccarini, M. *et al.* (2007) Density depletion at solid-liquid interfaces: A neutron reflectivity study. *Langmuir* 23: 598-608.
41. Zhang, X.Y., Zhu, Y.X., and Granick, S. (2002) Hydrophobicity at a Janus interface. *Science* 295: 663-666.
42. Christenson, H.K. and Claesson, P.M. (2001) Direct measurements of the force between hydrophobic surfaces in water. *Advances in Colloid and Interface Science* 91: 391-436.
43. Carambassis, A., Jonker, L.C., Attard, P., and Rutland, M.W. (1998) Forces measured between hydrophobic surfaces due to a submicroscopic bridging bubble. *Physical Review Letters* 80: 5357-5360.
44. Podgornik, R. and Parsegian, V.A. (1991) An Electrostatic-Surface Stability Interpretation of the Hydrophobic Force Inferred to Occur between Mica Plates in Solutions of Soluble Surfactants. *Chemical Physics* 154: 477-483.
45. Sharp, K.A., Nicholls, A., Fine, R.F., and Honig, B. (1991) Reconciling the Magnitude of the Microscopic and Macroscopic Hydrophobic Effects. *Science* 252: 106-109.
46. Zhou, R.H., Huang, X.H., Margulis, C.J., and Berne, B.J. (2004) Hydrophobic collapse in multidomain protein folding. *Science* 305: 1605-1609.
47. ten Wolde, P.R. and Chandler, D. (2002) Drying-induced hydrophobic polymer collapse. *Proceedings of the National Academy of Sciences of the United States of America* 99: 6539-6543.
48. Avbelj, F. and Baldwin, R.L. (2009) Origin of the change in solvation enthalpy of the peptide group when neighboring peptide groups are added. *Proceedings of the National Academy of Sciences of the United States of America* 106: 3137-3141.
49. Horinek, D. *et al.* (2008) Peptide adsorption on a hydrophobic surface results from an interplay of solvation, surface, and intrapeptide forces. *Proceedings of the National Academy of Sciences of the United States of America* 105: 2842-2847.
50. Sotomayor, M. and Schulten, K. (2007) Single-molecule experiments in vitro and in silico. *Science* 316: 1144-1148.
51. Mountain, R.D. and Thirumalai, D. (1998) Hydration for a series of hydrocarbons. *Proceedings of the National Academy of Sciences of the United States of America* 95: 8436-8440.
52. Collins, K.D. and Washabaugh, M.W. (1985) The Hofmeister Effect and the Behavior of Water at Interfaces. *Quarterly Reviews of Biophysics* 18: 323-422.
53. Kunz, W., Lo Nostro, P., and Ninham, B.W. (2004) The present state of affairs with Hofmeister effects. *Current Opinion in Colloid & Interface Science* 9: 1-18.
54. Collins, K.D., Neilson, G.W., and Enderby, J.E. (2007) Ions in water: Characterizing the forces that control chemical processes and biological structure. *Biophysical Chemistry* 128: 95-104.
55. Collins, K.D. (2006) Ion hydration: Implications for cellular function, polyelectrolytes, and protein crystallization. *Biophysical Chemistry* 119: 271-281.
56. Zhang, Y.J. and Cremer, P.S. (2006) Interactions between macromolecules and ions: the Hofmeister series. *Current Opinion in Chemical Biology* 10: 658-663.
57. Bostrom, M. *et al.* (2005) Why forces between proteins follow different Hofmeister series for pH above and below pI. *Biophysical Chemistry* 117: 217-224.
58. Machado, F.F. *et al.* (2007) Solubility and density of egg white proteins: Effect of pH and saline concentration. *Lwt-Food Science and Technology* 40: 1304-1307.

59. Baldwin, R.L. (1986) Temperature-Dependence of the Hydrophobic Interaction in Protein Folding. *Proceedings of the National Academy of Sciences of the United States of America* 83: 8069-8072.
60. Bauduin, P. *et al.* (2006) Hofmeister specific-ion effects on enzyme activity and buffer pH: Horseradish peroxidase in citrate buffer. *Journal of Molecular Liquids* 123: 14-19.
61. Bostrom, M., Williams, D.R.M., and Ninham, B.W. (2002) Influence of Hofmeister effects on surface pH and binding of peptides to membranes. *Langmuir* 18: 8609-8615.
62. Tadeo, X., Pons, M., and Millet, O. (2007) Influence of the hofmeister anions on protein stability as studied by thermal denaturation and chemical shift perturbation. *Biochemistry* 46: 917-923.
63. Cacace, M.G., Landau, E.M., and Ramsden, J.J. (1997) The Hofmeister series: salt and solvent effects on interfacial phenomena. *Quarterly Reviews of Biophysics* 30: 241-277.
64. Debye, P. and Huckel, E. (1923) The theory of electrolytes I. The lowering of the freezing point and related occurrences. *Physikalische Zeitschrift* 24: 185-206.
65. Debye, P. and Huckel, E. (1923) The theory of the electrolyte II - The border law for electrical conductivity. *Physikalische Zeitschrift* 24: 305-325.
66. Collins, K.D. (2004) Ions from the Hofmeister series and osmolytes: effects on proteins in solution and in the crystallization process. *Methods* 34: 300-311.
67. Hofmeister, F. (1888) Von der Lehre der Wirkung der Salze. *Naunyn-Schmiedebergs Arch. Exp. Pathol. Pharmakol.* 24.
68. Mason, P.E. *et al.* (2005) Structure of aqueous glucose solutions as determined by neutron diffraction with isotopic substitution experiments and molecular dynamics calculations. *Journal of Physical Chemistry B* 109: 13104-13111.
69. Mason, P.E., Dempsey, C.E., Neilson, G.W., and Brady, J.W. (2005) Nanometer-scale ion aggregates in aqueous electrolyte solutions: Guanidinium sulfate and guanidinium thiocyanate. *Journal of Physical Chemistry B* 109: 24185-24196.
70. Xie, W.H., Shiu, W.Y., and Mackay, D. (1997) A review of the effect of salts on the solubility of organic compounds in seawater. *Marine Environmental Research* 44: 429-444.
71. Nandi, P.K. and Robinson, D.R. (1972) Effects of Salts on Free-Energies of Nonpolar Groups in Model Peptides. *Journal of the American Chemical Society* 94: 1308-&.
72. von Hippel, P.H. and Schleich, T.W. (1969) The effects of neutral salts on the structure and conformational stability of macromolecules in solution. *Biological Macromolecules* 2: 417-584.
73. Mcdevit, W.F. and Long, F.A. (1952) The Activity Coefficient of Benzene in Aqueous Salt Solutions. *Journal of the American Chemical Society* 74: 1773-1777.
74. Bowron, D.T. and Finney, J.L. (2002) Anion bridges drive salting out of a simple amphiphile from aqueous solution. *Physical Review Letters* 89: -.
75. Finney, J.L. and Bowron, D.T. (2004) Anion bridges and salting out. *Current Opinion in Colloid & Interface Science* 9: 59-63.
76. Sacco, A., De Cillis, F.M., and Holz, M. (1998) NMR studies on hydrophobic interactions in solution - Part 3 Salt effects on the self-association of ethanol in water at two different temperatures. *Journal of the Chemical Society-Faraday Transactions* 94: 2089-2092.

77. Urry, D.W. (1993) Molecular Machines - How Motion and Other Functions of Living Organisms Can Result from Reversible Chemical-Changes. *Angewandte Chemie-International Edition in English* 32: 819-841.
78. Bostrom, M., Williams, D.R.M., and Ninham, B.W. (2003) Special ion effects: Why the properties of lysozyme in salt solutions follow a Hofmeister series. *Biophysical Journal* 85: 686-694.
79. Vrbka, L. *et al.* (2006) Specific ion effects at protein surfaces: A molecular dynamics study of bovine pancreatic trypsin inhibitor and horseradish peroxidase in selected salt solutions. *Journal of Physical Chemistry B* 110: 7036-7043.
80. Bostrom, M., Kunz, W., and Ninham, B.W. (2005) Hofmeister effects in surface tension of aqueous electrolyte solution. *Langmuir* 21: 2619-2623.
81. Kunz, W., Belloni, L., Bernard, O., and Ninham, B.W. (2004) Osmotic coefficients and surface tensions of aqueous electrolyte solutions: Role of dispersion forces. *Journal of Physical Chemistry B* 108: 2398-2404.
82. Hribar, B., Southall, N.T., Vlachy, V., and Dill, K.A. (2002) How ions affect the structure of water. *Journal of the American Chemical Society* 124: 12302-12311.
83. Breslow, R. and Guo, T. (1990) Surface-Tension Measurements Show That Chaotropic Salting-in Denaturants Are Not Just Water-Structure Breakers. *Proceedings of the National Academy of Sciences of the United States of America* 87: 167-169.
84. Petersen, P.B. and Saykally, R.J. (2006) On the nature of ions at the liquid water surface. *Annual Review of Physical Chemistry* 57: 333-364.
85. Cappa, C.D. *et al.* (2006) Effects of cations on the hydrogen bond network of liquid water: New results from X-ray absorption spectroscopy of liquid microjets. *Journal of Physical Chemistry B* 110: 5301-5309.
86. Naslund, L.A. *et al.* (2005) X-ray absorption spectroscopy study of the hydrogen bond network in the bulk water of aqueous solutions. *Journal of Physical Chemistry A* 109: 5995-6002.
87. Omta, A.W., Kropman, M.F., Woutersen, S., and Bakker, H.J. (2003) Negligible effect of ions on the hydrogen-bond structure in liquid water. *Science* 301: 347-349.
88. Dill, K.A., Truskett, T.M., Vlachy, V., and Hribar-Lee, B. (2005) Modeling water, the hydrophobic effect, and ion solvation. *Annual Review of Biophysics and Biomolecular Structure* 34: 173-199.
89. Zhao, H. (2006) Are ionic liquids kosmotropic or chaotropic? An evaluation of available thermodynamic parameters for quantifying the ion kosmotropicity of ionic liquids. *Journal of Chemical Technology and Biotechnology* 81: 877-891.
90. Collins, K.D. (1997) Charge density-dependent strength of hydration and biological structure. *Biophysical Journal* 72: 65-76.
91. Jungwirth, P. and Tobias, D.J. (2002) Ions at the air/water interface. *Journal of Physical Chemistry B* 106: 6361-6373.
92. Vrbka, L. *et al.* (2004) Propensity of soft ions for the air/water interface. *Current Opinion in Colloid & Interface Science* 9: 67-73.
93. Lima, E.R.A. *et al.* (2008) Specific ion adsorption and surface forces in colloid science. *Journal of Physical Chemistry B* 112: 1580-1585.
94. Netz, R.R. (2004) Water and ions at interfaces. *Current Opinion in Colloid & Interface Science* 9: 192-197.

95. Chang, T.M. and Dang, L.X. (2006) Recent advances in molecular simulations of ion solvation at liquid interfaces. *Chemical Reviews* 106: 1305-1322.
96. Horinek, D. *et al.* (2008) Molecular hydrophobic attraction and ion-specific effects studied by molecular dynamics. *Langmuir* 24: 1271-1283.
97. Bostrom, M., Williams, D.R.M., and Ninham, B.W. (2001) Specific ion effects: Why DLVO theory fails for biology and colloid systems. *Physical Review Letters* 8716: -.
98. Vrbka, L. *et al.* (2006) Quantification and rationalization of the higher affinity of sodium over potassium to protein surfaces. *Proceedings of the National Academy of Sciences of the United States of America* 103: 15440-15444.
99. Baldwin, R.L. (1996) How Hofmeister ion interactions affect protein stability. *Biophysical Journal* 71: 2056-2063.
100. Der, A. *et al.* (2007) Interfacial water structure controls protein conformation. *Journal of Physical Chemistry B* 111: 5344-5350.
101. Bostrom, M., Williams, D.R.M., and Ninham, B.W. (2001) Surface tension of electrolytes: Specific ion effects explained by dispersion forces. *Langmuir* 17: 4475-4478.
102. Street, T.O., Bolen, D.W., and Rose, G.D. (2006) A molecular mechanism for osmolyte-induced protein stability. *Proceedings of the National Academy of Sciences of the United States of America* 103: 13997-14002.
103. Yancey, P.H. *et al.* (1982) Living with Water-Stress - Evolution of Osmolyte Systems. *Science* 217: 1214-1222.
104. Timasheff, S.N. (1993) The Control of Protein Stability and Association by Weak-Interactions with Water - How Do Solvents Affect These Processes. *Annual Review of Biophysics and Biomolecular Structure* 22: 67-97.
105. Binnig, G., Quate, C.F., and Gerber, C. (1986) Atomic Force Microscope. *Physical Review Letters* 56: 930-933.
106. Muller, D.J. *et al.* (2002) Observing structure, function and assembly of single proteins by AFM. *Progress in Biophysics & Molecular Biology* 79: 1-43.
107. Shao, Z.F. and Yang, J. (1995) Progress in High-Resolution Atomic-Force Microscopy in Biology. *Quarterly Reviews of Biophysics* 28: 195-251.
108. Ludwig, M. *et al.* (1999) AFM, a tool for single-molecule experiments. *Applied Physics a-Materials Science & Processing* 68: 173-176.
109. Janshoff, A., Neitzert, M., Oberdorfer, Y., and Fuchs, H. (2000) Force spectroscopy of molecular systems - Single molecule spectroscopy of polymers and biomolecules. *Angewandte Chemie-International Edition* 39: 3213-3237.
110. Haupt, B.J., Senden, T.J., and Sevick, E.M. (2002) AFM evidence of Rayleigh instability in single polymer chains. *Langmuir* 18: 2174-2182.
111. Rief, M. *et al.* (1997) Reversible unfolding of individual titin immunoglobulin domains by AFM. *Science* 276: 1109-1112.
112. Marszalek, P.E., Oberhauser, A.F., Pang, Y.P., and Fernandez, J.M. (1998) Polysaccharide elasticity governed by chair-boat transitions of the glucopyranose ring. *Nature* 396: 661-664.
113. Dammer, U. *et al.* (1996) Specific antigen/antibody interactions measured by force microscopy. *Biophysical Journal* 70: 2437-2441.
114. Kufer, S.K. *et al.* (2005) Covalent immobilization of recombinant fusion proteins with hAGT for single molecule force spectroscopy. *European Biophysics Journal with Biophysics Letters* 35: 72-78.

115. Sonnenberg, L. *et al.* (2007) Choose sides: Differential polymer adhesion. *Langmuir* 23: 6660-6666.

116. Goodman, D., Kizhakkedathu, J.N., and Brooks, D.E. (2004) Evaluation of an atomic force microscopy pull-off method for measuring molecular weight and polydispersity of polymer brushes: Effect of grafting density. *Langmuir* 20: 6238-6245.

117. Cui, S.X., Liu, C.J., and Zhang, X. (2003) Simple method to isolate single polymer chains for the direct measurement of the desorption force. *Nano Letters* 3: 245-248.

118. Dietz, H. and Rief, M. (2007) Detecting molecular fingerprints in single molecule force spectroscopy using pattern recognition. *Japanese Journal of Applied Physics Part 1-Regular Papers Brief Communications & Review Papers* 46: 5540-5542.

119. Florin, E.L., Moy, V.T., and Gaub, H.E. (1994) Adhesion Forces between Individual Ligand-Receptor Pairs. *Science* 264: 415-417.

120. Merkel, R. *et al.* (1999) Energy landscapes of receptor-ligand bonds explored with dynamic force spectroscopy. *Nature* 397: 50-53.

121. Xu, L.C. and Siedlecki, C.A. (2007) Effects of surface wettability and contact time on protein adhesion to biomaterial surfaces. *Biomaterials* 28: 3273-3283.

122. Hayashi, T. *et al.* (2006) Mechanism underlying specificity of proteins targeting inorganic materials. *Nano Letters* 6: 515-519.

123. Conti, M. *et al.* (2002) Force spectroscopy study of the adhesion of plasma proteins to the surface of a dialysis membrane: Role of the nanoscale surface hydrophobicity and topography. *Journal of Biomedical Materials Research* 61: 370-379.

124. Kidoaki, S. and Matsuda, T. (1999) Adhesion forces of the blood plasma proteins on self-assembled monolayer surfaces of alkanethiolates with different functional groups measured by an atomic force microscope. *Langmuir* 15: 7639-7646.

125. Akari, S., Horn, D., Keller, H., and Schrepp, W. (1995) Chemical Imaging by Scanning Force Microscopy. *Advanced Materials* 7: 549-551.

126. Papastavrou, G., Akari, S., and Mohwald, H. (2000) Interactions between hydrophilic and hydrophobic surfaces on microscopic scale and the influence of air bubbles as observed by scanning force microscopy in aqueous and alcoholic mediums. *Europhysics Letters* 52: 551-556.

127. Friedsam, C. *et al.* (2004) Polymer functionalized AFM tips for long-term measurements in single-molecule force spectroscopy. *Chemphyschem* 5: 388-393.

128. Friedsam, C., Gaub, H.E., and Netz, R.R. (2006) Probing surfaces with single-polymer atomic force microscope experiments. *Biointerphases* 1: Mr1-Mr21.

129. Hugel, T. *et al.* (2002) Single-molecule optomechanical cycle. *Science* 296: 1103-1106.

130. Geisler, M. *et al.* (2008) Hydrophobic and Hofmeister effects on the adhesion of spider silk proteins onto solid substrates: An AFM-based single-molecule study. *Langmuir* 24: 1350-1355.

131. Sonnenberg, L. *et al.* (2007) Quantitative single molecule measurements on the interaction forces of poly(L-glutamic acid) with calcite crystals. *Journal of the American Chemical Society* 129: 15364-15371.

132. Friedsam, C., Gaub, H.E., and Netz, R.R. (2005) Adsorption energies of single charged polymers. *Europhysics Letters* 72: 844-850.

133. Hanke, F., Livadaru, L., and Kreuzer, H.J. (2005) Adsorption forces on a single polymer molecule in contact with a solid surface. *Europhysics Letters* 69: 242-248.

134. Chatellier, X., Senden, T.J., Joanny, J.F., and di Meglio, J.M. (1998) Detachment of a single polyelectrolyte chain adsorbed on a charged surface. *Europhysics Letters* 41: 303-308.

135. Hugel, T. and Seitz, M. (2001) The study of molecular interactions by AFM force spectroscopy. *Macromolecular Rapid Communications* 22: 989-1016.

136. Seitz, M. *et al.* (2003) Probing solid surfaces with single polymers. *Chemphyschem* 4: 986-990.

137. Hugel, T. *et al.* (2001) Elasticity of single polyelectrolyte chains and their desorption from solid supports studied by AFM based single molecule force spectroscopy. *Macromolecules* 34: 1039-1047.

138. Cui, S., Liu, C., Wang, Z., and Zhang, X. (2004) Single molecule force spectroscopy on polyelectrolytes: Effect of spacer on adhesion force and linear charge density on rigidity. *Macromolecules* 37: 946-953.

139. Shi, W.Q. *et al.* (2005) Force spectroscopy on dendronized poly(p-phenylene)s: Revealing the chain elasticity and the interfacial interaction. *Macromolecules* 38: 861-866.

140. Staple, D.B. *et al.* (2009) Polymer adsorption on surfaces I: Thermodynamics and equilibrium theory. *Biophysical Journal* submitted.

141. Serr, A., Horinek, D., and Netz, R.R. (2008) Polypeptide friction and adhesion on hydrophobic and hydrophilic surfaces: A molecular dynamics case study. *Journal of the American Chemical Society* 130: 12408-12413.

142. Serr, A. and Netz, R.R. (2006) Pulling adsorbed polymers from surfaces with the AFM: stick vs. slip, peeling vs. gliding. *Europhys. Lett.* 73: 292-298.

143. Hanke, F. and Kreuzer, H.J. (2006) Breaking bonds in the atomic force microscope: Theory and analysis. *Physical Review E* 74: -.

144. Kreuzer, H.J., Payne, S.H., and Livadaru, L. (2001) Stretching a macromolecule in an atomic force microscope: Statistical mechanical analysis. *Biophysical Journal* 80: 2505-2514.

145. Staple, D.B., Hanke, F., and Kreuzer, H.J. (2008) Dynamics of single-molecule force-ramp experiments: The role of fluctuations. *Physical Review E* 77: -.

146. Staple, D.B. *et al.* (2009) Polymer adsorption on surfaces II: Nonequilibrium theory and experiment. *Biophysical Journal* submitted.

147. Hanke, F. and Kreuzer, H.J. (2005) Nonequilibrium theory of polymer stretching based on the master equation. *Physical Review E* 72: -.

148. Schlierf, M. and Rief, M. (2005) Temperature softening of a protein in single-molecule experiments. *Journal of Molecular Biology* 354: 497-503.

149. Li, H.B. *et al.* (2000) Point mutations alter the mechanical stability of immunoglobulin modules. *Nature Structural Biology* 7: 1117-1120.

150. Nevo, R. *et al.* (2003) A molecular switch between alternative conformational states in the complex of Ran and importin beta 1. *Nature Structural Biology* 10: 553-557.

151. Puchner, E.M., Franzen, G., Gautel, M., and Gaub, H.E. (2008) Comparing proteins by their unfolding pattern. *Biophysical Journal* 95: 426-434.

152. Bustamante, C., Marko, J.F., Siggia, E.D., and Smith, S. (1994) Entropic Elasticity of Lambda-Phage DNA. *Science* 265: 1599-1600.

153. Rief, M., Gautel, M., Schemmel, A., and Gaub, H.E. (1998) The mechanical stability of immunoglobulin and fibronectin III domains in the muscle protein titin measured by atomic force microscopy. *Biophysical Journal* 75: 3008-3014.

154. Hugel, T. *et al.* (2005) Highly stretched single polymers: Atomic-force-microscope experiments versus ab-initio theory. *Physical Review Letters* 94: -.

155. Cao, Y., Kuske, R., and Li, H.B. (2008) Direct observation of Markovian behavior of the mechanical unfolding of individual proteins. *Biophysical Journal* 95: 782-788.

156. Junker, J.P., Ziegler, F., and Rief, M. (2009) Ligand-Dependent Equilibrium Fluctuations of Single Calmodulin Molecules. *Science* 323: 633-637.

157. Schwaiger, I., Schleicher, M., Noegel, A.A., and Rief, M. (2005) The folding pathway of a fast-folding immunoglobulin domain revealed by single-molecule mechanical experiments. *Embo Reports* 6: 46-51.

158. Evans, E. and Ritchie, K. (1999) Strength of a weak bond connecting flexible polymer chains. *Biophysical Journal* 76: 2439-2447.

159. Bell, G.I. (1978) Models for Specific Adhesion of Cells to Cells. *Science* 200: 618-627.

160. Yang, W.Y. and Gruebele, M. (2003) Folding at the speed limit. *Nature* 423: 193-197.

161. Schlierf, M. and Rief, M. (2006) Single-molecule unfolding force distributions reveal a funnel-shaped energy landscape. *Biophysical Journal* 90: L33-L35.

162. Evans, E. (2001) Probing the relation between force - Lifetime - and chemistry in single molecular bonds. *Annual Review of Biophysics and Biomolecular Structure* 30: 105-128.

163. Zhang, H.Y. and Marko, J.F. (2008) Maxwell relations for single-DNA experiments: Monitoring protein binding and double-helix torque with force-extension measurements. *Physical Review E* 77: -.

164. Adamson, A.W. and Gast, A.P., *Physical Chemistry of Surfaces*, sixth ed. (Wiley, New York, 1997).

165. Can, O. and Holland, N.B. (2009) Modified Langmuir isotherm for a two-domain adsorbate: Derivation and application to antifreeze proteins. *Journal of Colloid and Interface Science* 329: 24-30.

166. Thomas, A.S. and Elcock, A.H. (2007) Molecular dynamics simulations of hydrophobic associations in aqueous salt solutions indicate a connection between water hydrogen bonding and the Hofmeister effect. *Journal of the American Chemical Society* 129: 14887-14898.

167. Wennerstrom, H. (2004) Ion binding to interfaces. *Current Opinion in Colloid & Interface Science* 9: 163-164.

168. Pocius, A.V. ed., *Adhesion and Adhesives Technology: An Introduction*, 2nd ed. (Hanser Gardner Publ, 2002).

169. Browning, R.L. *et al.* (2006) Quantitative evaluation of scratch resistance of polymeric coatings based on a standardized progressive load scratch test. *Surface & Coatings Technology* 201: 2970-2976.

170. Chalker, P.R., Bull, S.J., and Rickerby, D.S. (1991) A Review of the Methods for the Evaluation of Coating-Substrate Adhesion. *Materials Science and Engineering a-Structural Materials Properties Microstructure and Processing* 140: 583-592.

171. Meagher, L. and Craig, V.S.J. (1994) Effect of Dissolved-Gas and Salt on the Hydrophobic Force between Polypropylene Surfaces. *Langmuir* 10: 2736-2742.

172. Roberts, M.J., Bentley, M.D., and Harris, J.M. (2002) Chemistry for peptide and protein PEGylation. *Advanced Drug Delivery Reviews* 54: 459-476.

173. Abdella, P.M., Smith, P.K., and Royer, G.P. (1979) New Cleavable Reagent for Cross-Linking and Reversible Immobilization of Proteins. *Biochemical and Biophysical Research Communications* 87: 734-742.

174. Heyes, C.D., Kobitski, A.Y., Amirgoulova, E.V., and Nienhaus, G.U. (2004) Biocompatible surfaces for specific tethering of individual protein molecules. *Journal of Physical Chemistry B* 108: 13387-13394.

175. Oesterhelt, F., Rief, M., and Gaub, H. (1999) Single molecule force spectroscopy by AFM indicates helical structure of poly(ethylene-glycol) in water. *New Journal of Physics* 1: 6.1-6.11.

176. Rammensee, S., Slotta, U., Scheibel, T., and Bausch, A.R. (2008) Assembly mechanism of recombinant spider silk proteins. *Proceedings of the National Academy of Sciences of the United States of America* 105: 6590-6595.

177. Huemmerich, D. *et al.* (2004) Primary structure elements of spider dragline silks and their contribution to protein solubility. *Biochemistry* 43: 13604-13612.

178. Dudko, O.K., Hummer, G., and Szabo, A. (2008) Theory, analysis, and interpretation of single-molecule force spectroscopy experiments. *Proceedings of the National Academy of Sciences of the United States of America* 105: 15755-15760.

179. Châtelier, X. and Joanny, J.F. (1998) pull-off of a polyelectrolyte chain from an oppositely charged surface. *Phys. Rev. E* 57: 6923-6935.

180. Haupt, B.J., Ennis, J., and Sevick, E.M. (1999) The detachment of a polymer chain from a weakly adsorbing surface using an AFM tip. *Langmuir* 15: 3886-3892.

181. Meiners, J.C. and Quake, S.R. (2000) Femtonewton force spectroscopy of single extended DNA molecules. *Physical Review Letters* 84: 5014-5017.

182. Blummel, J. *et al.* (2007) Protein repellent properties of covalently attached PEG coatings on nanostructured SiO2-based interfaces. *Biomaterials* 28: 4739-4747.

183. Efremova, N.V., Sheth, S.R., and Leckband, D.E. (2001) Protein-induced changes in poly(ethylene glycol) brushes: Molecular weight and temperature dependence. *Langmuir* 17: 7628-7636.

184. Yang, Z.H., Galloway, J.A., and Yu, H.U. (1999) Protein interactions with poly(ethylene glycol) self-assembled monolayers on glass substrates: Diffusion and adsorption. *Langmuir* 15: 8405-8411.

185. Sofia, S.J., Premnath, V., and Merrill, E.W. (1998) Poly(ethylene oxide) grafted to silicon surfaces: Grafting density and protein adsorption. *Macromolecules* 31: 5059-5070.

186. Halperin, A. (1999) Polymer brushes that resist adsorption of model proteins: Design parameters. *Langmuir* 15: 2525-2533.

187. Variola, F. *et al.* (2009) Improving Biocompatibitity of Implantable Metals by Nanoscale Modification of Surfaces: An Overview of Strategies, Fabrication Methods, and Challenges. *Small* 5: 996-1006.

188. Lim, J.Y. and Donahue, H.J. (2007) Cell sensing and response to micro- and nanostructured surfaces produced by chemical and topographic patterning. *Tissue Engineering* 13: 1879-1891.

189. Liu, X. *et al.* (2007) Influence of substratum surface chemistry/energy and topography on the human fetal osteoblastic cell line hFOB 1.19: Phenotypic and genotypic responses observed in vitro. *Biomaterials* 28: 4535-4550.

190. Curtis, A. and Wilkinson, C. (1997) Topographical control of cells. *Biomaterials* 18: 1573-1583.

191. Han, M., Sethuraman, A., Kane, R.S., and Belfort, G. (2003) Nanometer-scale roughness effect on adsorbed protein. *Langmuir* 19: 9868-9872.

192. Fukuzaki, S., Urano, H., and Nagata, K. (1995) Adsorption of Protein onto Stainless-Steel Surfaces. *Journal of Fermentation and Bioengineering* 80: 6-11.

193. Singh, N. and Husson, S.M. (2006) Adsorption thermodynamics of short-chain peptides on charged and uncharged nanothin polymer films. *Langmuir* 22: 8443-8451.

194. Buijs, J. and Hlady, V. (1997) Adsorption kinetics, conformation, and mobility of the growth hormone and lysozyme on solid surfaces, studied with TIRF. *Journal of Colloid and Interface Science* 190: 171-181.

195. Uhlmann, P. *et al.* (2007) In-situ investigation of the adsorption of globular model proteins on stimuli-responsive binary polyelectrolyte brushes. *Langmuir* 23: 57-64.

196. Lu, J.R., Zhao, X.B., and Yaseen, M. (2007) Protein adsorption studied by neutron reflection. *Current Opinion in Colloid & Interface Science* 12: 9-16.

197. Michiardi, A. *et al.* (2007) The influence of surface energy on competitive protein adsorption on oxidized NiTi surfaces. *Biomaterials* 28: 586-594.

198. Noh, H., Yohe, S.T., and Vogler, E.A. (2008) Volumetric interpretation of protein adsorption: ion-exchange adsorbent capacity, protein pI, and interaction energetics. *Biomaterials* 29: 2033-2048.

199. Cha, P., Krishnan, A., Fiore, V.F., and Vogler, E.A. (2008) Interfacial energetics of protein adsorption from aqueous buffer to surfaces with varying hydrophobicity. *Langmuir* 24: 2553-2563.

200. Ostuni, E. *et al.* (2001) Survey of structure-property relationships of surfaces that resist the adsorption of protein. *Langmuir* 17: 5605-5620.

201. Hone, D., Ji, H., and Pincus, P.A. (1987) Polymer Adsorption on Rough Surfaces .1. Ideal Long-Chain. *Macromolecules* 20: 2543-2549.

202. Ji, H. and Hone, D. (1988) Polymer Adsorption on Rough Surfaces .2. Good Solvent Conditions. *Macromolecules* 21: 2600-2605.

203. Zimin, D., Craig, V.S.J., and Kunz, W. (2004) Adsorption and desorption of polymer/surfactant mixtures at solid-liquid interfaces: Substitution experiments. *Langmuir* 20: 8114-8123.

204. Sun, W., Long, J., Xu, Z., and Masliyah, J.H. (2008) Study of Al(OH)3-polyacrylamide-induced pelleting flocculation by single molecule force spectroscopy. *Langmuir* 24: 14015-14021.

205. Williams, D.F. (2008) On the mechanisms of biocompatibility. *Biomaterials* 29: 2941-2953.

206. Wessely, R. *et al.* (2005) Inhibition of neointima fomation by a novel drug-eluting stent system that allows for dose-adjustable, multiple, and on-site stent coating. *Arterioscle. Thromb. Vasc. Biol.* 25: 748-753.

207. Cognard, P. ed., *Adhesives and Sealants - General Knowledge, Application Techniques, New Curing Techniques*. (Elsevier, 2006).

208. Ulman, A. (1996) Formation and structure of self-assembled monolayers. *Chemical Reviews* 96: 1533-1554.

209. Atre, S.V., Liedberg, B., and Allara, D.L. (1995) Chain-Length Dependence of the Structure and Wetting Properties in Binary Composition Monolayers of Oh-Terminated and Ch3-Terminated Alkanethiolates on Gold. *Langmuir* 11: 3882-3893.

210. Pavlov, G.M. *et al.* (2006) Molecular Properties and Electrostatic Interactions of Linear Poly(allylamine hydrochloride) Chains. *Progress in Colloid and Polymer Science* 131: 134-140.

211. Arai, T. *et al.* (2002) Preparation of silk fibroin and polyallylamine composites. *Journal of Applied Polymer Science* 84: 1963-1970.

212. Pathak, A., Vyas, S.P., and Gupta, K.C. (2008) Nano-vectors for efficient liver specific gene transfer. *International Journal of Nanomedicine* 3: 31-49.

213. Pathak, A. *et al.* (2007) Engineered polyallylamine nanoparticles for efficient in vitro transfection. *Pharmaceutical Research* 24: 1427-1440.

214. Zelzer, M. *et al.* (2008) Investigation of cell-surface interactions using chemical gradients formed from plasma polymers. *Biomaterials* 29: 172-184.

215. Krekea, M.R. *et al.* (2005) Modulation of protein adsorption and cell adhesion by poly(allylamine hydrochloride) heparin films. *Biomaterials* 26: 2975-2981

216. Nebel, C.E. *et al.* (2007) Diamond and biology. *Journal of the Royal Society Interface* 4: 439-461.

217. Lechleitner, T. *et al.* (2008) The surface properties of nanocrystalline diamond and nanoparticulate diamond powder and their suitability as cell growth support surfaces. *Biomaterials* 29: 4275-4284.

218. Hartl, A. *et al.* (2007) The ion sensitivity of surface conductive single crystalline diamond. *Journal of the American Chemical Society* 129: 1287-1292.

219. Landstrass, M.I. and Ravi, K.V. (1989) Resistivity of Chemical Vapor-Deposited Diamond Films. *Applied Physics Letters* 55: 975-977.

220. Nonnenmacher, M., Oboyle, M.P., and Wickramasinghe, H.K. (1991) Kelvin Probe Force Microscopy. *Applied Physics Letters* 58: 2921-2923.

221. Scherer, A. *et al.* (2005) Intermolecular interactions of polymer molecules determined by single-molecule force spectroscopy. *Macromolecules* 38: 9821-9825.

222. Friedsam, C., Seitz, M., and Gaub, H.E. (2004) Investigation of polyelectrolyte desorption by single molecule force spectroscopy. *Journal of Physics-Condensed Matter* 16: S2369-S2382.

223. Kane, R.S., Deschatelets, P., and Whitesides, G.M. (2003) Kosmotropes form the basis of protein-resistant surfaces. *Langmuir* 19: 2388-2391.

224. Shimizu, S., Kiuchi, T., and Pan, N. (2007) A "Teflon-Footed" resorcinarene: A hexameric capsule in fluorous solvents and fluorophobic effects on molecular encapsulation. *Angewandte Chemie-International Edition* 46: 6442-6445.

225. Carrion-Vazquez, M. *et al.* (1999) Mechanical and chemical unfolding of a single protein: A comparison. *Proceedings of the National Academy of Sciences of the United States of America* 96: 3694-3699.

226. Bornschlogl, T. and Rief, M. (2006) Single molecule unzipping of coiled coils: Sequence resolved stability profiles. *Physical Review Letters* 96: -.

227. Patete, J. *et al.* (2009) Hofmeister Effect on the Interfacial Free Energy of Aliphatic and Aromatic Surfaces Studied by Chemical Force Microscopy. *Journal of Physical Chemistry B* 113: 583-588.

228. Pirzer, T., Geisler, M., Scheibel, T., and Hugel, T. (2009) Single molecule force measurements delineate salt, pH and surface effects on biopolymer adhesion. *Physical Biology* 6: -.

229. Vendrely, C. and Scheibel, T. (2007) Biotechnological production of spider-silk proteins enables new applications. *Macromolecular Bioscience* 7: 401-409.

230. Kyte, J. and Doolittle, R.F. (1982) A Simple Method for Displaying the Hydropathic Character of a Protein. *Journal of Molecular Biology* 157: 105-132.

231. Weisenberger, S. and Schumpe, A. (1996) Estimation of gas solubilities in salt solutions at temperatures from 273 K to 363 K. *Aiche Journal* 42: 298-300.

232. Maibaum, L., Dinner, A.R., and Chandler, D. (2004) Micelle formation and the hydrophobic effect. *Journal of Physical Chemistry B* 108: 6778-6781.

233. Grainger, D.W. and Castner, D.G. (2008) Nanobiomaterials and nanoanalysis: opportunities for improving the science to benefit biomedical technologies. *Advanced Materials* 20: 867-877.

234. Krueger, A. (2008) New carbon materials: Biological applications of functionalized nanodiamond materials. *Chemistry-a European Journal* 14: 1382-1390.

235. Kalbacova, M. *et al.* (2007) The effect of SWCNT and nano-diamond films on human osteoblast cells. *Physica Status Solidi B-Basic Solid State Physics* 244: 4356-4359.

236. Kloss, F.R. *et al.* (2008) Commercial developments of nano-crystalline diamond - two prototypes as case studies. *Diamond & Related Materials* 17: 1089-1099.

237. Tang, Y., Aslam, D.M., Wang, J., and Wise, K.D. (2006) Study of polycrystalline diamond piezoresistive position sensors for application in cochlear implant probe. *Diamond & Related Materials* 15: 199-202.

238. Lud, S.Q. *et al.* (2006) Chemical grafting of biphenyl self-assembled monolayers on ultrananocrystalline diamond. *Journal of the American Chemical Society* 128: 16884-16891.

239. Härtl, A., Baur, B., Stutzmann, M., and Garrido, J.A. (2008) Enzyme modified field effect transistors based on surface conductive single crystalline diamond. *Langmuir* 24: 9898-9906.

240. Troupe, C.E. *et al.* (1998) Diamond based glucose sensors. *Diamond & Related Materials* 7: 575-580.

241. Kanazawa, H. *et al.* (2003) Effect of iodide ions on the hydrogen-terminated and partially oxygen-terminated diamond surface. *Diamond and Related Materials* 12: 618-622.

242. Nebel, C.E., Rezek, B., Shin, D., and Watanabe, H. (2006) Surface electronic properties of H-terminated diamond in contact with adsorbates and electrolytes. *Physica Status Solidi a-Applications and Materials Science* 203: 3273-3298.

243. Rezek, B. and Nebel, C.E. (2005) Kelvin force microscopy on diamond surfaces and devices. *Diamond and Related Materials* 14: 466-469.

244. Girad, P. (2001) Electrostatic force microscopy: principles and some applications to semiconductors. *Nanotechnology* 12: 485-490.

245. Jacobs, H.O., Leuchtmann, P., Homan, O.J., and Stemmer, A. (1998) Resolution and contrast in Kelvin probe force microscopy. *Journal of Applied Physics* 84: 1168-1173.

246. Rezek, B. and Nebel, C.E. (2006) Electronic properties of plasma hydrogenated diamond surfaces: A microscopic study. *Diamond and Related Materials* 15: 1374-1377.

247. Petrini, D. and Larsson, K. (2007) A theoretical study of the energetic stability and geometry of hydrogen- and oxygen-terminated diamond (100) surfaces. *Journal of Physical Chemistry C* 111: 795-801.

248. Petrini, D. and Larsson, K. (2008) Theoretical study of the thermodynamic and kinetic aspects of terminated (111) diamond surfaces. *Journal of Physical Chemistry C* 112: 3018-3026.

249. Athawale, M.V., Sarupria, S., and Garde, S. (2008) Enthalpy-entropy contributions to salt and osmolyte effects on molecular-scale hydrophobic hydration and interactions. *Journal of Physical Chemistry B* 112: 5661-5670.

250. Schellman, J.A. (1997) Temperature, stability, and the hydrophobic interaction. *Biophysical Journal* 73: 2960-2964.

251. Lee, B. (1991) Isoenthalpic and Isoentropic Temperatures and the Thermodynamics of Protein Denaturation. *Proceedings of the National Academy of Sciences of the United States of America* 88: 5154-5158.

252. Garde, S. *et al.* (1996) Origin of entropy convergence in hydrophobic hydration and protein folding. *Physical Review Letters* 77: 4966-4968.

253. Hummer, G. *et al.* (1998) The pressure dependence of hydrophobic interactions is consistent with the observed pressure denaturation of proteins. *Proceedings of the National Academy of Sciences of the United States of America* 95: 1552-1555.

254. Hummer, G., Garde, S., Garcia, A.E., and Pratt, L.R. (2000) New perspectives on hydrophobic effects. *Chemical Physics* 258: 349-370.

255. Robertson, A.D. and Murphy, K.P. (1997) Protein structure and the energetics of protein stability. *Chemical Reviews* 97: 1251-1267.

256. Olofsson, G., Oshodj, A.A., Qvarnstrom, E., and Wadso, I. (1984) Calorimetric Measurements on Slightly Soluble Gases in Water - Enthalpies of Solution of Helium, Neon, Argon, Krypton, Xenon, Methane, Ethane, Propane, Normal-Butane, and Oxygen at 288.15, 298.15, and 308.15 K. *Journal of Chemical Thermodynamics* 16: 1041-1052.

257. Gill, S.J., Nichols, N.F., and Wadso, I. (1976) Calorimetric Determination of Enthalpies of Solution of Slightly Soluble Liquids .2. Enthalpy of Solution of Some Hydrocarbons in Water and Their Use in Establishing Temperature-Dependence of Their Solubilities. *Journal of Chemical Thermodynamics* 8: 445-452.

258. Makhatadze, G.I. and Privalov, P.L. (1989) Heat-Capacity of Alcohols in Aqueous-Solutions in the Temperature-Range from 5-Degrees-C to 125-Degrees-C. *Journal of Solution Chemistry* 18: 927-936.

259. Murphy, K.P. and Gill, S.J. (1989) Thermodynamics of Dissolution of Solid Cyclic Dipeptides Containing Hydrophobic Side Groups. *Journal of Chemical Thermodynamics* 21: 903-913.

260. Privalov, P.L. and Gill, S.J. (1988) Stability of Protein-Structure and Hydrophobic Interaction. *Advances in Protein Chemistry* 39: 191-234.

261. Fu, L. and Freire, E. (1992) On the Origin of the Enthalpy and Entropy Convergence Temperatures in Protein Folding. *Proceedings of the National Academy of Sciences of the United States of America* 89: 9335-9338.

262. Holzmann, J., Ludwig, R., Geiger, A., and Paschek, D. (2008) Temperature and Concentration Effects on the Solvophobic Solvation of Methane in Aqueous Salt Solutions. *Chemphyschem* 9: 2722-2730.

263. Fujita, T., Watanabe, H., and Tanaka, S. (2007) Effects of salt addition on strength and dynamics of hydrophobic interactions. *Chemical Physics Letters* 434: 42-48.

264. Dobson, C.M. (2003) Protein folding and misfolding. *Nature* 426: 884-890.

265. Taylor, J.P., Hardy, J., and Fischbeck, K.H. (2002) Biomedicine - Toxic proteins in neurodegenerative disease. *Science* 296: 1991-1995.

266. Slotta, U. *et al.* (2007) Spider silk and amyloid fibrils: A structural comparison. *Macromolecular Bioscience* 7: 183-188.

267. Kenney, J.M., Knight, D., Wise, M.J., and Vollrath, F. (2002) Amyloidogenic nature of spider silk. *European Journal of Biochemistry* 269: 4159-4163.

268. Knowles, T.P. *et al.* (2007) Role of intermolecular forces in defining material properties of protein nanofibrils. *Science* 318: 1900-1903.

269. Liu, L., Komatsu, H., Murray, I.V.J., and Axelsen, P.H. (2008) Promotion of amyloid beta protein misfolding and fibrillogenesis by a lipid oxidation product. *Journal of Molecular Biology* 377: 1236-1250.

270. Ray, C. and Akhremitchev, B.B. (2005) Conformational heterogeneity of surface-grafted amyloidogenic fragments of alpha-synuclein dimers detected by atomic force microscopy. *Journal of the American Chemical Society* 127: 14739-14744.

271. Domanov, Y.A. and Kinnunen, P.K.J. (2008) Islet amyloid polypeptide forms rigid lipid-protein amyloid fibrils on supported phospholipid bilayers. *Journal of Molecular Biology* 376: 42-54.

272. Lee, J.H., Bhak, G., Lee, S.G., and Paik, S.R. (2008) Instantaneous amyloid fibril formation of alpha-synuclein from the oligomeric granular structures in the presence of hexane. *Biophysical Journal* 95: L16-L18.

273. Sandal, M. *et al.* (2008) Conformational equilibria in monomeric alpha-synuclein at the single-molecule level. *Plos Biology* 6: 99-108.

274. Yu, J.P., Malkova, S., and Lyubchenko, Y.L. (2008) alpha-Synuclein Misfolding: Single Molecule AFM Force Spectroscopy Study. *Journal of Molecular Biology* 384: 992-1001.

275. Karsai, A. *et al.* (2006) Mechanical manipulation of Alzheimer's amyloid beta 1-42 fibrils. *Journal of Structural Biology* 155: 316-326.

276. Becker, N. *et al.* (2003) Molecular nanosprings in spider capture-silk threads. *Nature Materials* 2: 278-283.

277. Sawaya, M.R. *et al.* (2007) Atomic structures of amyloid cross-beta spines reveal varied steric zippers. *Nature* 447: 453-457.

278. Xiao, S.B. *et al.* (2009) Mechanical Response of Silk Crystalline Units from Force-Distribution Analysis. *Biophysical Journal* 96: 3997-4005.

279. Lammel, A. *et al.* (2008) Processing conditions for the formation of spider silk microspheres. *Chemsuschem* 1: 413-416.

280. Gosline, J.M., Guerette, P.A., Ortlepp, C.S., and Savage, K.N. (1999) The mechanical design of spider silks: From fibroin sequence to mechanical function. *Journal of Experimental Biology* 202: 3295-3303.

281. Friedsam, C., Wehle, A.K., Kuhner, F., and Gaub, H.E. (2003) Dynamic single-molecule force spectroscopy: bond rupture analysis with variable spacer length. *Journal of Physics-Condensed Matter* 15: S1709-S1723.

282. Evans, E. and Ritchie, K. (1997) Dynamic strength of molecular adhesion bonds. *Biophysical Journal* 72: 1541-1555.

283. Carrion-Vazquez, M., Marszalek, P.E., Oberhauser, A.F., and Fernandez, J.M. (1999) Atomic force microscopy captures length phenotypes in single proteins. *Proceedings of the National Academy of Sciences of the United States of America* 96: 11288-11292.

284. Makin, O.S. and Serpell, L.C. (2005) Structures for amyloid fibrils. *Febs Journal* 272: 5950-5961.

285. Slotta, U.K., Rammensee, S., Gorb, S., and Scheibel, T. (2008) An engineered spider silk protein forms microspheres. *Angewandte Chemie-International Edition* 47: 4592-4594.

286. Metwalli, E. *et al.* (2007) Structural changes of thin films from recombinant spider silk proteins upon post-treatment. *Applied Physics a-Materials Science & Processing* 89: 655-661.

287. Asakura, T., Okonogi, M., Nakazawa, Y., and Yamauchi, K. (2006) Structural analysis of alanine tripeptide with antiparallel and parallel beta-sheet structures in relation to the analysis of mixed beta-sheet structures in Samia cynthia ricini silk protein fiber using solid-state NMR spectroscopy. *Journal of the American Chemical Society* 128: 6231-6238.

288. Carrion-Vazquez, M. *et al.* (2003) The mechanical stability of ubiquitin is linkage dependent. *Nature Structural Biology* 10: 738-743.

289. Oberhauser, A.F., Marszalek, P.E., Erickson, H.P., and Fernandez, J.M. (1998) The molecular elasticity of the extracellular matrix protein tenascin. *Nature* 393: 181-185.

290. Smith, B.L. *et al.* (1999) Molecular mechanistic origin of the toughness of natural adhesives, fibres and composites. *Nature* 399: 761-763.

291. Keten, S. and Buehler, M.J. (2008) Geometric confinement governs the rupture strength of H-bond assemblies at a critical length scale. *Nano Letters* 8: 743-748.

292. Termonia, Y. (1994) Molecular Modeling of Spider Silk Elasticity. *Macromolecules* 27: 7378-7381.

293. Schellman, J.A. (2005) Destabilization and stabilization of proteins. *Quarterly Reviews of Biophysics* 38: 351-361.

294. Cunningham, P., Afzal-Ahmed, I., and Naftalin, R.J. (2006) Docking studies show that D-glucose and quercetin slide through the transporter GLUT1. *Journal of Biological Chemistry* 281: 5797-5803.

295. Mueckler, M. *et al.* (1985) Sequence and Structure of a Human Glucose Transporter. *Science* 229: 941-945.

296. Alberts, B., Bray, D., and Lewis, J., *Molecular Biology of the Cell*, fourth ed. (Taylor & Francis, 2002).

297. Gavutis, M., Lata, S., and Piehler, J. (2006) Probing 2-dimensional protein-protein interactions on model membranes. *Nature Protocols* 1: 2091-2103.

298. D'Auria, S. *et al.* (2006) Binding of glucose to the D-galactose/D-glucose-binding protein from Escherichia coli restores the native protein secondary structure and thermostability that are lost upon calcium depletion. *Journal of Biochemistry* 139: 213-221.

299. Yang, M.S., Yau, H.C.M., and Chan, H.L. (1998) Adsorption kinetics and ligand-binding properties of thiol-modified double-stranded DNA on a gold surface. *Langmuir* 14: 6121-6129.

300. Velazquez-Campoy, A. and Freire, E. (2006) Isothermal titration calorimetry to determine association constants for high-affinity ligands. *Nature Protocols* 1: 186-191.

301. Timasheff, S.N. (2002) Protein-solvent preferential interactions, protein hydration, and the modulation of biochemical reactions by solvent components. *Proceedings of the National Academy of Sciences of the United States of America* 99: 9721-9726.

302. Ebel, C., Eisenberg, H., and Ghirlando, R. (2000) Probing protein-sugar interactions. *Biophysical Journal* 78: 385-393.

303. Mobley, D.L. and Dill, K.A. (2009) Binding of Small-Molecule Ligands to Proteins: "What You See" Is Not Always "What You Get". *Structure* 17: 489-498.

304. Harries, D. and Parsegian, V.A. (2004) Gibbs adsorption isotherm combined with Monte Carlo sampling to see action of cosolutes on protein folding. *Proteins-Structure Function and Bioinformatics* 57: 311-321.

305. Greenleaf, W.J., Woodside, M.T., and Block, S.M. (2007) High-resolution, single-molecule measurements of biomolecular motion. *Annual Review of Biophysics and Biomolecular Structure* 36: 171-190.

306. Ali, B.M.J. *et al.* (2001) Compaction of single DNA molecules induced by binding of integration host factor (IHF). *Proceedings of the National Academy of Sciences of the United States of America* 98: 10658-10663.

307. Skoko, D. *et al.* (2006) Mechanism of chromosome compaction and looping by the Escherichia coli nucleoid protein Fis. *Journal of Molecular Biology* 364: 777-798.

308. Krautbauer, R. *et al.* (2002) Discriminating small molecule DNA binding modes by single molecule force spectroscopy. *Febs Letters* 510: 154-158.

309. Strey, R. *et al.* (1999) On the necessity of using activities in the Gibbs equation. *Journal of Physical Chemistry B* 103: 9112-9116.

310. Hu, Y.F. and Wang, Z.C. (1997) Isopiestic studies on (mannitol plus sorbitol plus D-glucose)(aq) and two of the subsystems at the temperature 298.15 K. *Journal of Chemical Thermodynamics* 29: 879-884.

311. Miyajima, K., Sawada, M., and Nakagaki, M. (1983) Studies on Aqueous-Solutions of Saccharides .1. Activity-Coefficients of Monosaccharides in Aqueous-Solutions at 25-Degrees-C. *Bulletin of the Chemical Society of Japan* 56: 1620-1623.

312. Fazal, F.M. and Hansen, D.E. (2007) Glucose-specific poly(allylamine) hydrogels- A reassessment. *Bioorganic & Medicinal Chemistry Letters* 17: 235-238.

313. Wizeman, W.J. and Kofinas, P. (2001) Molecularly imprinted polymer hydrogels displaying isomerically resolved glucose binding. *Biomaterials* 22: 1485-1491.

314. Parmpi, P. and Kofinas, P. (2004) Biomimetic glucose recognition using molecularly imprinted polymer hydrogels. *Biomaterials* 25: 1969-1973.

315. Hong, L., Bush, W.D., Hatcher, L.Q., and Simon, J. (2008) Determining thermodynamic parameters from isothermal calorimetric isotherms of the binding of macromolecules to metal cations originally chelated by a weak ligand. *Journal of Physical Chemistry B* 112: 604-611.

316. Tellinghuisen, J. (2007) Optimizing experimental parameters in isothermal titration calorimetry: Variable volume procedures. *Journal of Physical Chemistry B* 111: 11531-11537.

317. Kim, W., Yamasaki, Y., and Kataoka, K. (2006) Development of a fitting model suitable for the isothermal titration calorimetric curve of DNA with cationic ligands. *Journal of Physical Chemistry B* 110: 10919-10925.

318. Hedgeland, H. *et al.* (2009) Measurement of single-molecule frictional dissipation in a prototypical nanoscale system. *Nature Physics* 5: 561-564.

319. Cannara, R.J. *et al.* (2007) Nanoscale friction varied by isotopic shifting of surface vibrational frequencies. *Science* 318: 780-783.

320. Serr, A. and Netz, R. (2007) Enhancing polymer adsorption by lateral pulling. *Europhys. Lett.* 78: 1-5.

321. Butt, H.J. and Jaschke, M. (1995) Calculation of Thermal Noise in Atomic-Force Microscopy. *Nanotechnology* 6: 1-7.

322. Stark, R.W., Drobek, T., and Heckl, W.M. (2001) Thermomechanical noise of a free v-shaped cantilever for atomic-force microscopy. *Ultramicroscopy* 86: 207-215.

323. Proksch, R. *et al.* (2004) Finite optical spot size and position corrections in thermal spring constant calibration. *Nanotechnology* 15: 1344-1350.

324. Schaffer, T.E. (2005) Calculation of thermal noise in an atomic force microscope with a finite optical spot size. *Nanotechnology* 16: 664-670.

325. Viani, M.B. *et al.* (1999) Small cantilevers for force spectroscopy of single molecules. *Journal of Applied Physics* 86: 2258-2262.

326. Kuhner, F. and Gaub, H.E. (2006) Modelling cantilever-based force spectroscopy with polymers. *Polymer* 47: 2555-2563.

327. Sonnenberg, L. *et al.* (2006) AFM-based single molecule force spectroscopy of end-grafted poly(acrylic acid) monolayers. *Macromolecules* 39: 281-288.

328. Schmidt, M., Romer, L., Strehle, M., and Scheibel, T. (2007) Conquering isoleucine auxotrophy of Escherichia coli BLR(DE3) to recombinantly produce spider silk proteins in minimal media. *Biotechnology Letters* 29: 1741-1744.

329. Gronwald, W. *et al.* (1996) NMR characterization of side chain flexibility and backbone structure in the type I antifreeze protein at near freezing temperatures. *Biochemistry* 35: 16698-16704.

330. Hermanson, G.T. ed., *Bioconjugate Techniques*, 2nd ed. (Academic Press, 2008).

331. Stalder, A.F. *et al.* (2006) A snake-based approach to accurate determination of both contact points and contact angles. *Colloids and Surfaces a-Physicochemical and Engineering Aspects* 286: 92-103.

332. Jacobs, H.O., Knapp, H.F., and Stemmer, A. (1999) Practical aspects of Kelvin probe force microscopy. *Review of Scientific Instruments* 70: 1756-1760.

333. Leendertz, C., Streicher, F., Lux-Steiner, M.C., and Sadewasser, S. (2006) Evaluation of Kelvin probe force microscopy for imaging grain boundaries in chalcopyrite thin films. *Applied Physics Letters* 89: -.

334. Liscio, A., Palermo, V., and Samori, P. (2008) Probing local surface potential of quasi-one-dimensional systems: A KPFM study of P3HT nanofibers. *Advanced Functional Materials* 18: 907-914.

335. Krok, F. *et al.* (2008) Lateral resolution and potential sensitivity in Kelvin probe force microscopy: Towards understanding of the sub-nanometer resolution. *Physical Review B* 77: -.

List of Publications

Parts of this thesis have been published in or submitted to peer-reviewed journals, further manuscripts are in preparation for submission. These contributions include:

M1. Geisler, M. and Hugel, T. (**2007**) Device and method for the acquisition of forces in the sub-Micro Newton regime. *European Patent Office* PCT/EP2008/050075.

M2. Geisler, M., Pirzer, T., Ackerschott, C. *et al.* (**2008**) Hydrophobic and Hofmeister effects on the adhesion of spider silk proteins onto solid substrates: An AFM-based single-molecule study. *Langmuir* 24: 1350-1355.

M3. Horinek, D., Serr, A., Geisler, M. *et al.* (**2008**) Peptide adsorption on a hydrophobic surface results from an interplay of solvation, surface, and intrapeptide forces. *Proceedings of the National Academy of Sciences of the United States of America* 105: 2842-2847.

M4. Pirzer, T., Geisler, M., Scheibel, T., and Hugel, T. (**2009**) Single molecule force measurements delineate salt, pH and surface effects on biopolymer adhesion. *Physical Biology* 6: -.

M5. Geisler, M., Balzer, N.B., and Hugel, T. (**2009**) Polymer adhesion at the solid-liquid interface probed by a single molecule force sensor. *Small* DOI: 10.1002/smll.200901237.

M6. Geisler, M. and Hugel, T. (**2009**) Aging of hydrogenated and oxidized diamond. *Advanced Materials* DOI: 10.1002/adma.200902198 .

M7. Geisler, M., Horinek, D., and Hugel, T. (**2009**) Single molecule adhesion mechanics on rough surfaces. *Macromolecules* DOI: 10.1021/ma9017372.

M8. Staple, D.B., Geisler, M., Kreplak, L. *et al.* (**2009**) Polymer adsorption on interfaces I: What can be learned from plateau forces? Submitted.

M9. Staple, D.B., Geisler, M., Kreplak, L. *et al.* (**2009**) Polymer adsorption on interfaces II: Non-equilibrium plateau forces. Submitted.

M10. Geisler, M., Netz, R.R., and Hugel, T. (**2009**) Pulling a single polymer off a substrate reveals binding thermodynamics of cosolutes. Submitted.

M11. Geisler, M., Xiao, S.B., Puchner, E.M. *et al.* (**2009**) Surface induced folding of a single spider silk protein into an amyloid-like secondary structure. Submitted.

M12. Geisler, M., Sedlmeier, F., Netz, R.R., and Hugel, T. (**2009**) Ion specific shift of convergence temperatures in polymer hydration. In preparation.

Acknowledgements

There are two types of honest people, those who confess and those who criticize. I am very glad that many people who contributed to this work are representatives of the latter. In the following, sincere thanks shall be given to all of them (including those I may have forgotten to mention here).

Foremost, I want to express my special gratitude to Dr. Thorsten Hugel. This dissertation would not have been possible without his expert guidance and his encouragement. Not only was he readily available for me, as he so generously is for all of his students, but he always read and responded to the drafts of each publication and chapter of this thesis more quickly than I could have hoped. I am deeply grateful to him for the long discussions that helped me sort out the technical details of my work and his substantive contributions to help me clarify my arguments.

I am equally thankful for having received much assistance from Dr. Roland R. Netz. His insightful comments and constructive criticisms at different stages of my research added significantly to my research progress and helped me focus my ideas, which I cannot value highly enough.

I was also greatly inspired by Dr. Mathias Rief and Dr. Andreas Bausch who were always willing to discuss current issues related to my work, commenting on my views and tactfully pointed out my misconceptions.

My sincere gratitude goes to Dr. Domink Horinek, Nadine Schwierz and Felix Sedlmeier for the fruitful collaboration, revelatory MD-simulations and many valuable discussions that helped me to understand what happens on the molecular scale.

I gladly express my gratitude to Dr. Frauke Gräter and Senbo Xiao from the University of Heidelberg and the Shanghai Institutes for Biological Sciences for their excellent teamwork regarding force-probe MD simulation on silk proteins. Intense discussion with them let me reconsider some of my views.

Many thanks go to Dr. Hans Jürgen Kreuzer and Douglas Staple from Dalhousie University, Canada, for their close collaboration and their profound work on the equilibrium theory and non-equilibrium effects.

I would like to gratefully acknowledge Dr. Thomas Scheibel, Ute Slotta and Dr. Christian Ackerschott from the University of Bayreuth for the kind donation of spider silk proteins. I am particularly thankful to Dr. Martin Stutzmann, Dr. José Antonio Garrido, Moritz Hauf and Simon Q. Lud from the Walter Schottky Institute for providing modified diamond surfaces.

I am deeply indebted to Dr. Michael Schlierf, Dr. Elias Puchner and Tobias Pirzer for their help with IGOR programming and for providing necessary software tools.

Many people on the faculty and in particular the IMETUM staff assisted and encouraged me in various ways during my course of studies. I am especially grateful to Susanne Schnell-

Witteczek and Josef Hintermair for their help and practical implementation of a number of experiments.

Moreover, I owe my gratitude to all those people who provided an inspiring and motivating working atmosphere, including Bizan N. Balzer, Fank Stetter, Christina Lumme, Christoph Ratzke and Dr. Moritz Mickler.

I appreciate the support of the Elitenetzwerk Bayern and the doctorate program Materials Science of Complex Interfaces.

Last but not least I want to give my thanks to the Stiftung Industrieforschung, namely Dr. Wolfgang Lerch and Dr. Peter Weirich for their support. Their obliging and open-minded cooperation which defied any bureaucracy has been invaluable.